NTNU

Norwegian University of
Science and Technology

Investigating Mixed Mode Loading of Materials Used in Fuel Cells

Stian Waagner Birkeland

Master of Science in Mechanical Engineering
Submission date: June 2018
Supervisor: Filippo Berto, MTP

Norwegian University of Science and Technology
Department of Mechanical and Industrial Engineering

Abstract

Fuel cell technology have the potential of being a crucial element of reducing greenhouse gas emission from transport, mainly road traffic. The technology is still facing challenges that hinders it commercialization, mainly durability and cost. Yttria stabilized zirconia is one of the more studied electrolytes for use in solid-oxide fuel cells, because of its beneficial thermal and electrical properties.

In this thesis, mixed mode fracture behaviour of yttria stabilized zirconia in asymmetric four point bending is studied. Finite element analysis of the test specimen is performed to obtain geometric factors of fracture and prepare the experiment. Fracture load predictions are performed by average strain energy density criterion.

Earlier experimental results of asymmetric four point bending are re-analysed by use of finite element method and the results are compared by use of average strain energy density criterion, maximum tangential stress criterion and generalized maximum tangential stress criterion.

Fracture load curves for the testing configuration is produced and the results show little influence by T-stress. The results show that the three fracture criterion predict similar behavior for mode I dominated loading and show more variation for mode II dominated loading, but neither of the criterion fit the analysed data better than the other for this limited study.

Sammendrag

Brenselcelle-teknologi har potensiale til å være en av de viktigste bidragsyterne til å redusere CO_2-utslipp fra transport, spesielt vegtrafikk. Teknologien har utfordringer som må løses før den er klar for kommersiell bruk, hovedsaklig kostnad og levetid. Yttria stabilisert zirconia er et av de mest prøvde elektrolyttene til bruk i faststoff brenselcelle på grunn av gode termiske og elektriske egenskaper.

Bruddmekanisk oppførsel for yttria stabilisert zirconia er utsatt for asymmetrisk firepunkts bøyetest ved hjelp av numerisk analyse for forberedelse av eksperiment. Geometriske faktorer knyttet til teststykket og testoppsett er presentert. Bruddlastestimering er utført ved bruk av kriteriet for gjennomsnittlig tøyningsenergitetthet.

Tidligere eksperimenter for asymmetrisk firepunkts bøyetest blir analysert ved hjelp av numerisk analyse for å sammenligne resultatene ved hjelp av kriteriene for gjennomsnittlig tøyningsenergitetthet, størst tangentiell spenning og generalisert størst tangentiell spenning.

Bruddlaster for yttria stabilisert zirconia viser seg lite påvirket av T-spenning. Resultatene viser at alle kriteriene gir samme mekaniske oppførsel når mode I bruddlasttilfelle dominerer, mens resultatene varier mer ved mode II bruddlasttilfelle dominans. Ingen av kriteriene skiller seg ut som mer egnet enn de andre for denne begrensede studien.
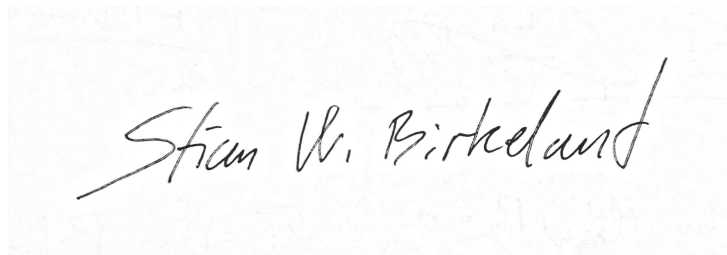
Preface

This master thesis is the final dissertation for the M.Sc. degree at the Department of Design and Materials at Norwegian University of Science and Technology. It concludes my five years at the university and my five years living in Trondheim. I'm grateful to all my friends that have made my life better and the memories will be cherished when I'm dead in 100 years.

I would like to thank my supervisor Professor Filippo Berto for guidance and coffee and co-supervisor PhD student Seyed Mohammad Javad Razavi for helpful discussions whenever I needed.

Thanks to my family for support throughout my whole life no matter what I do.

Thanks to Tora for being a lovely person.

Stian Waagner Birkeland

Contents

List of Figures

x

List of Tables

Chapter 1

Introduction

1.1 Motivation for research

Norway has the second highest per capita energy consumption in the world primarily because of a energy-intensive industry such as oil and gas, light metal and electrochemical production. Oil and gas specifically is a energy intensive industry which also contributes 25% of Norway's domestic green house gas emissions. Transportation by road traffic, aviation and shipping is larger again with is responsible for 33% of the emissions [1]. Norway pledged in 2009 to reduce greenhouse gas emissions by 30% of its 1990 domestic emissions by 2020, but by 2016 the emissions were 3% higher than compared to emissions from year 1990 [2]. Norway is in a beneficial position of energy production in which 49% of the consumed energy is by electricity. Most of that consumption is met by hydropower, but the road to achieving the goal of reduced greenhouse gas emissions is far away. Together with bio fuel and electricity, fuel cells are one of future solutions to cutting the emissions caused by transportation, primarily road traffic. Fuel cells are chemical factories able to produce electricity with hydrogen as fuel; it is a possible clean and efficient mechanism for energy conversion for the hydropower capacity. However, fuel cells are a complicated science with many challenges as an interdisciplinary science. Its construction requires the fields electrochemistry, material science, thermodynamics and engineering economics all come together to solve the challenges of fuel cells.

Fuel cells are typically divided into five different types of fuel cells where each one of them has their advantages, disadvantages and challenges. This thesis focus on the solid-oxide fuel cells (SOFC), more specifically on the structural integrity of yttria stabilized zirconia which is a common electrolyte for a SOFC. Because of high thermal cyclic stresses, sealing issues and high temperatures the durability and lifetime of a SOFC is relatively low. Understanding how electrolytes in the fuel cells behave when subjected to the different factors contributing to failure will allow us to understand how to improve the technology.

1.2 Objectives

The objective of the thesis is to prepare the experimental testing of an asymmetric four point bending (ASFPB) test by use of finite element analysis and perform testing of 30 yttria stabilized zirconia (YSZ) specimen. Because of a delay in the delivery of the ordered specimen announced mid May, the new objective is to analyse as many earlier experimental results as time permits in addition to the preparation of the experimental testing. All results are analyzed by average strain energy density (ASED) criterion,

maximum tangential stress (MTS) criterion and generalized maximum tangential stress (GMTS) criterion.

Points of interest are:

1. Testing configuration of 3x4x45 mm specimen using the equipment at Norwegian Universtiy of Science and Technology.

2. Fracture load curves by method of ASED.

3. Discussion of parameters that influence mixed mode loading behaviour.

4. Compare the ASED, MTS and GMTS criterion in light of earlier experimental results.

1.3   Structure of the thesis

The rest of the thesis is structured as follows: Chapter 2 is written to give an insight to the basic operation and construction of fuel cells and a review of the types of ceramic electrolytes that are studied for use in SOFCs. The electrolyte focus is on fracture behaviour, methods of testing and properties related to fuel cells in general. It is mainly limited in the range of year 2010 to 2018.

Chapter 3 explains linear elastic fracture mechanics, including basic fracture mechanics concepts, explanation of the singularity at the crack tip, mixed mode loading and the three fracture criterion used in this thesis.

Chapter 4 describes how the configuration of the experimental set up would have been performed and explains the finite element method used to do the analysis.

Chapter 5 present and discuss the obtained results.

The appendix contains the script used for simulation in Abaqus, supplementary results as plots and technical drawings used to order the specimen.

1.4   Approach

Much of the theory of this thesis is based on the book *Fracture Mechanics* by Ted L. Anderson [3], and the paper *Recent developments in brittle and quasi-brittle failure assessment of engineering materials by means of local approaches* by Berto and Lazzarin [4] have helped me use and explain the ASED criterion. Additionally, the paper published by Razavi et al. on application of the ASED criterion for ASFPB testing for granite [5] has been a good roadmap for the experimental approach for this thesis.

The two paper that are studied for analysis is *Mixed-Mode Fracture of Ceramics in Asymmetric Four-Point Bending: Effect of Crack-Face Grain Interlocking/Bridging* by Li et al. [6] and *Mixed-Mode Fracture Toughness of Ceramic Materials* by Suresh et al. [7].

Chapter 2

Fuel cells and ceramic electrolytes

2.1   Basic fuel cell operation

The fuel cell is analogous to a combustion engine as it generates power from a fuel source. It also has similarities to a battery as the process that generate power is primarily electrochemical. The simplest example is the combustion of hydrogen as it reacts with oxygen as shown in reaction R1.

$$H_2 + \frac{1}{2}O_2 \rightarrow CO + 2H_2O \tag{R1}$$

Hydrogen molecules are oxidised, resulting in water and releasing heat. The heat is created when hydrogen and oxygen molecules break their bonds to form H_2O-bonds, made up by the valens electrons of the hydrogen and oxygen atoms. The bonds of water molecules have lower energy configuration compared to the energy configuration of hydrogen molecule-bonds and oxygen molecule-bonds, and it is this difference that gives the heat (energy) release.

For fuel cells, the transfer of electrons from hydrogen to oxide-elements are forced through a longer distance. They are spatially removed from each other and by forcing the electrons to go a certain way the electrons can be harnessed as electrical current. The spatial separation is achieved with an electrolyte. The electrolyte is a material that allows ions to travel, but not electrons. The electrons are instead forced trough a circuit and can be forced to power a load. The basic most basic concept of a fuel cell is shown in figure 2.1.
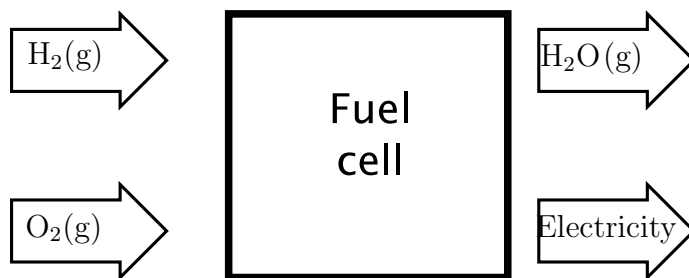
Figure 2.1: The basic concept of a fuel cell. Hydrogen gas acts as the fuel necessary for the process. Generally, electricity and water is the result of the process.
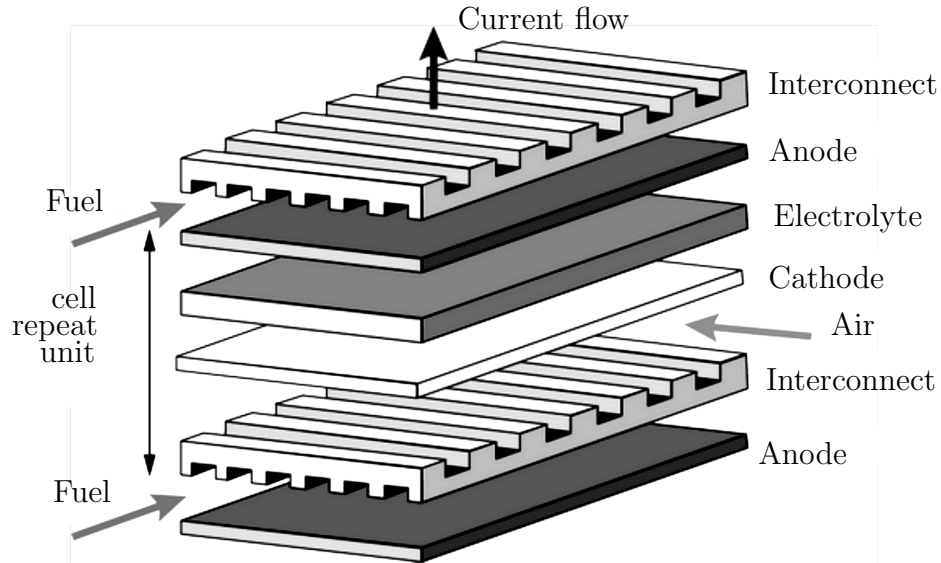
Figure 2.2: An exploded view of a stacked solid-oxide fuel cell. Retrieved from Universtiy of Cambridge [9].

The typical advantages that are associated with fuel cells are: less or no pollution, high thermodynamic efficiency, modularity and scalable, quiet and static, fuel flexibility and more. By scalable, its typically meant that they can be made larger or stacked. A staced cell is seen in figure 2.2. Typical disadvantages are immature technology infrastructure for use of hydrogen, sensitivity to contaminations, durability and stability in long term scope and high cost. High cost is especially important for the implentation of a technology [8].

A typical fuel cell consists of an anode, a cathode and the electrolyte that spatially separates the two. A fuel cell can be classified into five major types, which are differentiated by the different types of electrolyte.

1. Solid-oxide fuel cell (SOFC)

2. Polymer electrolyte membrane fuel cell (PEMFC)

3. Phosphoric acid fuel cell (PAFC)

4. Alkaline fuel cell (AFC)

5. Molten carbonate fuel cell (MCFC)

The five major fuel cells have operating temperature depending on the type of fuel applicable, but it is also dependant on the electrolyte. Yttria stabilized zirconia, one of the most studied electrolyte materials for SOFCs, require a certain temperature to obtain the crystal structure that ensure a sufficient conductivity, see section 2.2.5. High operating temperatures (range of 600-800 °C) lead to accelerated degradation because of thermal expansion mismatch between materials that make up the construction of the fuel cell. Temperatures is one of many ways stress can be induced. Stress can be induced on the electrolyte ceramic from residual stresses from manufacturing, temperature gradients, oxygen activity gradients and external mechanical loading. Complex simulations stacked cells stresses can be performed [10] [11] to simulate the stress induced by thermal

expansion, buckling-drive delamination because of compressive stress or delamination or cracking because of tensile stresses. Additionally, coarsening of grains, localized change of composition of the materials or phase transformations are other reasons the cell degrade, as well as the material property change can make the cell less resistive against the applied stresses. The construction is complicated and there are many ways to fail.

For this thesis, solid electrolytes, specifically yttria stabilized zirconia used for SOFC are studied. The general benefits of SOFC are:

- Fuel flexibility as SOFCs can use H_2, CH_4 and CO as fuel.

- Nonprecious metal as catalyst. Nickel is relatively inexpensive and can be used in planar SOFC.

- Cogeneration applications. Waste heat can be used to further raise effect of the system.

- Solid electrolyte is easier to manage than liquid electrolyte.

- Relatively high power density.

while the general disadvantages are:

- High temperature material issues, such as delamination, reduction of materials and different thermal expansion coefficient.

- Sealing issues. Hindering the degradation of sealants is difficult for both stacked and planar cells. Recent glass-based self healing sealants show promise [12].

- Relatively expensive components. The most studied electrolyte (YSZ) uses yttria which is a rare-earth mineral.

Note that these explanations use oversimplication and generalisation to introduce the reader to fuel cells and the electrolyte material that is studied further.

2.2 Ceramics used in solid-oxide fuel cells

2.2.1 Crystal structure and the general ceramic electrolytes

Ceramics are composed of at least two elements and often more. Ceramic materials may have ionic or covalent bonding, or a combination of both. A ceramics crystal structure is determined by the size of the cation and anion and the magnitude of the electrical charge on each of the component ions.

The electrochemical reactions at the anode and cathode for a fuel cell either consume or produce ions and electrons. The ions are transported through the electrolyte by diffusion while the electrons go through electrically conductive paths. The effectiveness of an fuel cell is hugely dependant on the ionic conductivity and electric conductivity of an electrolyte. The electrolyte should have relatively high ionic conductivity and relatively low electric conductivity for the best performance. The conductivity is highly dependant on the material structure and is an important area of study [13]. The ionic conductivity is depends on the relative size on the dopant ions compared to the original structure ions. Aliovalent, or substitional impurity ions, create oxygen-ion conductivity since the dopant
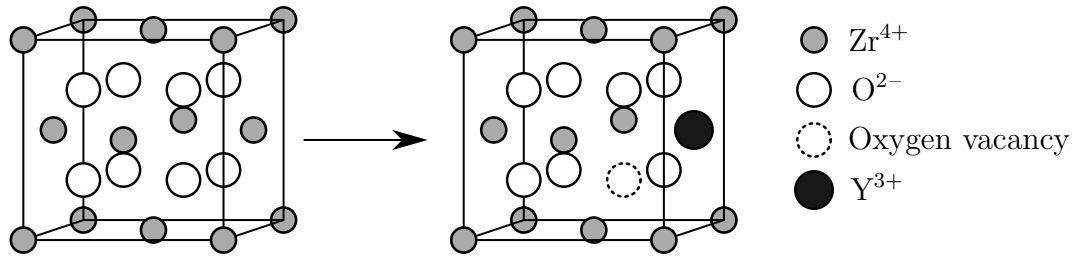
Figure 2.3: Yttria stabilized zirconia cubic fluroite crystal structure.

creates a oxygen vacancies to maintain electroneutrality. The point defects (substition ion) and vacancy interact through elastic strain introduced to the crystal lattice. A mismatch in size between the original crystal ion and dopant ion give rise to relatively higher stress in the lattice. Results show the best ion conductors are the ones where dopant ions are relatively similar to the original ions. The doping will increase ionic conductivity up to a certain point, where the increased interaction between dopant ions and the vacancies causes the conductivity to drop [14].

2.2.2 Doped Ceria

Ceria (CeO_4) can be doped with a aliovalent lanthanide metal, meaning a metal with atom number 57 to 71 that can substitute the original ion. The general form is $Ce_{1-\delta}(Ln)_\delta O_{2-1/2\delta}$. The general advantage with doped ceria over yttria stabilized zirconia, is that usually shows higher ionic conductivity of oxygen at lower temperatures. Disadvantages of doped ceria is that Ce^{4+} partially reduce to Ce^{3+} which induce n-type electronic conductivity. This can lead to internal shortage in the electrolyte. This reduction of Ce increases with increasing temperature. Ceria also expands under reducing conditions because of nonstochiometry and induce stresses in the structure.

Ceria can be doped with gadolinium, making a fluorite crystal structure. The doping range of 10-20 mol% usually gives suitable properties for SOFC. 10% mol gadolinium doped ceria, $Ce_0 \cdot 9\,Gd_0 \cdot 1\,O_1 \cdot 95$, (GDC10) has ionic conductivity of 0.01 Scm^{-1} at 500 °C. ([14] source [104]), but GDC is generally considered an option for operating temperatures from 500 to 700 °C. Morales et al. [15] studies GDC elastic modulus E, hardness H and fracture toughness K_{IC} by method of nanoindentation, assumed at RT. For 10GDC they report a Young's modulus of 202 GPa, which decreases with increasing percentage of gadolinium doping. For 20GDC the Young's modulus is 186 GPa. Gao et al. [16] studies the Young's modulus by high-temperature resonant ultrasound technique, which for 10GDC corresponds well with the values reported by Morales, though the difference between 10GDC and 20GDC is less prominent. Gao shows that GDC has only small deviation from linear behaviour between Young's Modulus and temperature, compared to SCSZ and YSZ. The coefficient of thermal expansion for GDC is higher than YSZ and SCSZ with about 20%.

Cao et al. [17] studied the effect of CuO doping of GDC, reporting a lower required temperature when sintering for a full densification requirement. Additionally, when sintering CuO-doped GDC at 1100 °C, it showed higher relative density and increased flexural strength.

Samaria doped ceria is a less studied ceria compared to GDC. SDC typically has the same benefits as GDC and the doping range of samaria is also typically 10-20 mol%. The combination of both samaria and gadolinium doping has been studied by Daza et al. [18]

and the codoping gives increased ionic conductivity at 700 °C because of better structural homogeneity.

2.2.3   Scandia stabilized zirconia

Ramesh et al. [19] and Ng et al. [20] studied the mechanical properties of 10 mol% scandia stabilized zirconia doped with 1 mol% ceria (10Sc1CeSZ). The studies compares conventional box sintering at varying temperature and microwaved-sintering at two different temperatures. The ceramic pellets are — **size**. The Vicker's Hardness (HV) for scandia-stabilized zirconia (SDZ) ranging from 14.6 GPa to 13.1 GPa and trends with increasing sintering temperature from 1300 to 1550 °C. Using microwave-sintered SSZ at 1300 and 1350 °C, the harndess is 13.6 and 14.2 GPa respectively.

How the fracture toughness is measured is not mentioned, but it is assumed by hardness measurement/indentation. The fracture toughness is relatively stable around 3.5 MPam$^{0.5}$ and with highest value being 3.7 MPam$^{1/2}$ at 1450 °C. By microwave-sintering, the values are 3.4 and 3.3 MPam$^{1/2}$ for 1300 and 1350 °C respectively. The elastic modulus is also varies between 180-215 GPa, with highest values for 1300 and 1350 °C.

2.2.4   Doped Lanthanum Gallate (LSGM)

Morales et al. [21] [22] study the mechanical properties and ionic conductivity of $LaGaO_3$ (Lanthanum Gallate) perovskite doped with Sr and Mg. They compare two composites where both compositions where sintered at 1300, 1350, 1400 and 1450 °C. LSGM materials are possible candidates for electrolytes in SOFC because of relatively high ionic conduction at 800 °C. The indentation testing was performed with pyramic 3-sided Berkovich diamond indenter. The hardness varied between 9.17 and 11.25 GPa and the authors note that it is higher than previously reported results because the indentation technique doesn't take grain size and manufacturing defects in consideration. They conclude that the hardness reduces when secondary phases such as $LaSrGaO_4$ and $LaSrGa_3O_7$ are present. The secondary phases migrate to the grain boundaries of the primary phase of LSGM perovskite.

2.2.5   Yttria stabilized zirconia

Yttria stabilized zirconia (YSZ) is one of the most studied electrolyte materials. YSZ is created by doping zirconia (ZrO_2) with a percentage of yttria (Y_2O_3), usually 3, 5, 8 or 10 mol%. 3YSZ is usually used for the anode, 5YSZ can be used as substrate in automobile oxygen sensors, while 8YSZ has high ionic conductivity and is suitable as a ceramic electrolyte. The thermal and mechanical propterties of YSZ depends on the amount of doping as well as temperature. 3YSZ exhibits both monoclinic and tetragonal crystal structure troughout, but tetragonal is the stable one for higher temperatures, see fig 2.4. 5YSZ shows stable tetragonal structure for sintering temperatures from 1300 to 1450 [23]. For concentrations of 8YSZ, the cubic structure is stable from 0 °C to operating temperatures of 800 °C. The phase diagram for $ZrO_2 - YO_{1.5}$ is shown in figure 2.4. The higher temperature phase transformations have recently been studied by Asadikiya et al. [24] where the ZrO_2-rich side has been thoroughly evaluated. The phase diagram shows that operating temperatures in the range of 600-800 °C will change the crystal structure of the material. The cubic crystal structure can be seen in fig 2.3. For fuel
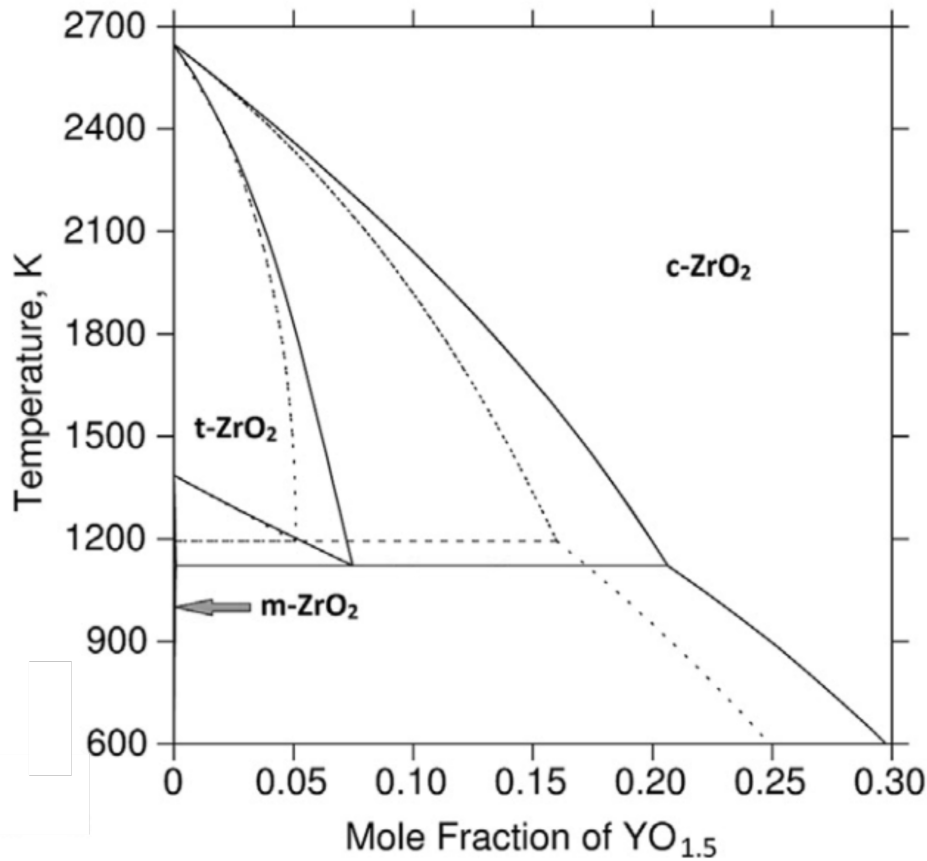
Figure 2.4: ZrO_2-rich side of the phase diagram for the $ZrO_2-YO_{1.5}$-system. Retrieved from Asadikiya et al. [24].

cell stacks, the ceramic is usually sintered after a tape casting process. Increasing the sintering temperature leads to larger grain size. The grain resistance and grain boundary resistance for 5YSZ increases with larger grain size, as shown by Xia et al [23]. It is important to note that even though 8YSZ has an higher average grain size than 8YSZ [25], 8YSZ still has better conductivity than 5YSZ [14].

The relative density is also affected by the sintering temperature and affect mechanical properties such as elastic modulus or fracture toughness. For certain electrolytes used in SOFCs, a high density is wanted as some have the highest amount of conductivty at high density [22]. Additionally, since the sintering process for SOFCs by tape-casting often yield 99% relative density [26], a relative density above 95% or higher should be targeted when tested. If not achievable, it should be thoroughly documented. For an increased sintering temperature the relative density dropped from 98% to 96%, the flexural strength of a 5YSZ ceramic dropped 10.5% in addition to an increased grain size [23].

The mechanical properties of YSZ change with concentration of yttria. Nakajo et al. [27] compiled the mechanical properties of YSZ since the mechanical failure of one cell in a fuel cell stack can end its service life. The Young's Modulus can be obtained by various methods traditional means, but an interesting non-destructive method is the impulse excitation technique which is great when dealing with expensive rare-earth ceramics. The values varies between 219.5 and 223.9 GPa at RT for 8YSZ and between 213.2 and 218.9 for 3YSZ. For 8YSZ the values corresponds well with values acquired later years from Gao et al. [16] including the temperature dependant Young's modulus. Morales et al.
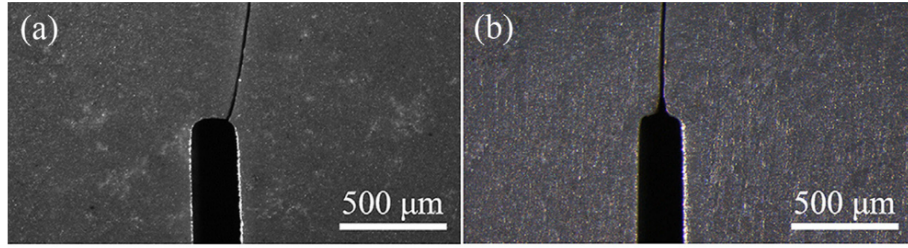
Figure 2.5: Optical microscope images of a a) precracked specimen and b) V-notch machined by laser [29].

test by using indentation method and shows that at displacement should least be 500 nm to get valid results, which show similar values [15]. Masini et al. [28] also tests one cell of a stacked electrolyte supported fuel cell to better understand the effect of co-sintering and the interaction between layers. Different techniques of obtaining elastic modulus gave different results, which shows the complexity of the problem with layered structures. As the authors themselves mention, one should be careful to interpret the results.

Mode I fracture toughness, K_{Ic}, has been studied on YSZ by indentation hardness, bending tests and ball-on-3-ball tests. Morales et al. [15] found K_{Ic} of 8YSZ by indentation and Palmqvist cracks to be 1.79 MPam$^{1/2}$. A indentation of 500 nm was required to counteract indentation size effects, meaning surface defects such as submicrometer cracks, dislocations roughness and porosity. The fracture to Heiroth et al. [30] studied the toughness of 700 nm thin films of ceramics and qualitatively determined 3YSZ to have higher fracture toughness than 8YSZ as a result of toughness induced by the tetragonal to monoclinic phase transformation. It was also concluded that the general 3YSZ-ceramic had higher hardness and elastic modulus if the crystal structure was crystalline rather than amorphous. For 5YSZ with stable tetragonal crystal structure, increased density at sintering temperature 1350°C compared to 1300, 1400 and 1450 also showed incrased mode I fracture toughness, flexural strength and Vicker's Hardness [23]. Quinn et al. [31] concludes in 2007 that Vickers indentation fracture toughness tests does not correctly measure any crack propagation parameter. It does measure a complex crack arresting phenomenom. However, it seems it is still a much used method of approximation of the values since it is a non-destructive method. The values and papers discussed give good indication of the mechanical properties and the relationship between amount of doped yttria. It also shows the importance of crystal structure, especially relevant for 3YSZ.

Three or four point bending tests measuring K_{Ic} for brittle materials can be time consuming. Instead of using a razor and diamond paste to obtain a crack with micrometer notch radius, Zhao, Rao and Ling [29] presents the use of a femtosecond laser to micromachine a sharp notch with radius $\rho<0.5$ µm in a U-groove. The use of SEVNB as a superior method to SEPB is also shown, as precracking is hard to control for brittle materials, see figure 2.5. The study also show that width of U-groove does not effect the value of K_{Ic} when the radius is less than 0.5 µm. Wang et al. [32] test multiple ceramic materials where the crack for SEVNB testing is prepared by diamond wire or diamond wheel cutting, razor and diamond paste with grain size varying from 1-20 µm, laser and bridge indentation, results shown in figure 2.6. The results clearly show laser machining of the notch giving intrinsic values similar to the ones from bridge intendation. Using laser machining by a femtosecond laser, Liu et al. [25] measures K_{Ic} of 3YSZ, 5YSZ and 8YSZ. It is reasonable to believe the results are accurate measurements when notch radius
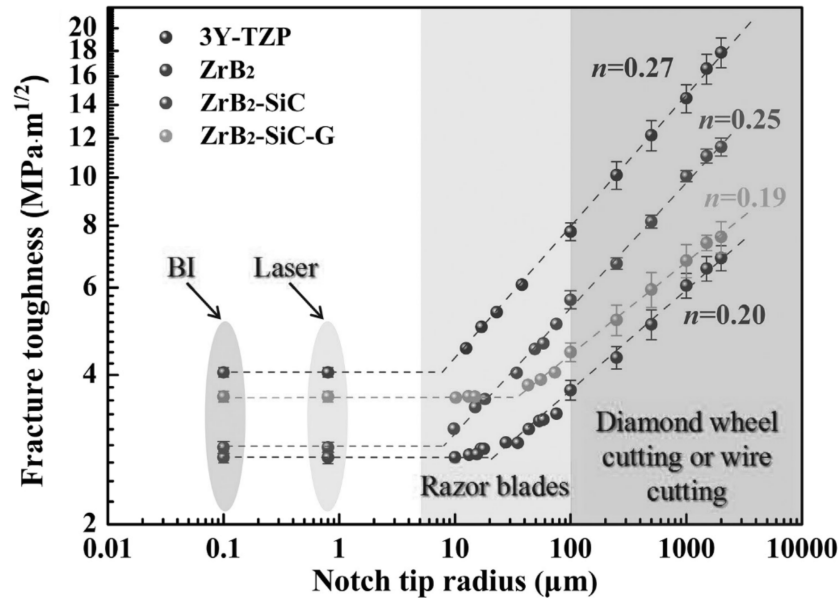
Figure 2.6: Variation of $K_{\mathrm{I,c}}$ with notch tip radius. BI stands for bridge indentation. Retrieved from Wang et al. [32].

is about 0.25 μm, lower than the grain size of the tested samples of 3YSZ and thus lower than the major microstructural feature size.

Subcritical crack growth (SCCG) is relevant for the ceramics used in SOFCs because of the environment that the electrolytes are in. SCCG have been observed for YSZ composites by Kumar and Sorensen [26] and Chevalier et al. [33]. Boccacini et al. found that increased porosity increased the rate of SCCG, but still retained mechanical properties which could be tolerable for use in SOFC.

In summary, the choice of electrolyte is difficult. Some are advantageous for high temperatures while other have better conductivity, better stability, fracture properties or are easily manufactured. The ideal trade off is not easy to find, However, the more that is known for the electrolytes, the further we are to find the best combination of material properties, structure and construction of the fuel cells. The ceramics for SOFCs needs to be meticulously tested so they can be tailored for its use.

Chapter 3

Theory

3.1 Fundamentals of material science

3.1.1 Deformation and strain

Under the action of forces, a body may *deform* to occupy a new region. The *displacement* of a point from the original body becuase of deformation can be expressed as $u_i = (u_1, u_2, u_3)$ for a rectangular Cartesian coordinate system. Displacement is considered a vector or first-order tensor quantity. *Strain* is defined as deformation from a reference configuration to the current configuration. It is useful to define strain for different directions, such as

$$\varepsilon_{rr} = \frac{\partial u_r}{\partial r} \tag{3.1a}$$

$$\varepsilon_{\theta\theta} = \frac{u_r}{r} + \frac{1}{r}\frac{\partial u_\theta}{\partial \theta} \tag{3.1b}$$

$$\varepsilon_{r\theta} = \frac{1}{2}\left(\frac{1}{r}\frac{\partial u_r}{\partial \theta} + \frac{\partial u_\theta}{\partial r} - \frac{u_\theta}{r}\right) \tag{3.1c}$$

for polar coordinates.

3.1.2 Stress

A *stress* component at a point in a material is the forces per unit area (in the limit) acting on the the planes passing trough the point [34]. The stresses on any plane can be computed from stresses on three orthogonal planes passing through the point and such a tensor is called a stress tensor. For a finite area and specifically axial testing, *engineering stress* $\sigma = F/A_i$ is often used, where A_i is the inital cross section area.

3.1.3 Elasticity

Elasticity as a material property describes the ability to deform under load without the deformation beeing permanent, usually referred to as *elastic deformation*. Modulus of elasticity E, or Youngs' modulus, is a material parameter describing the materials elastic property to deform when subjected to loading. The well known equation $\sigma = E\varepsilon$ is a specific case of Hooke's law of elasticity. The generalized Hooke's law states that the most

linear relationship between stresses and strains such that the stresses vanish when the strains are zero is $\sigma_{ij} = C_{ijkl}\varepsilon_{kl}$ where C_{ijkl} is a fourth-order tensor with elastic constants describing the relationship between the stress components and strain components [34]. A *tensor* is a mathematical representation of physical quantities. Typically, brittle materials have relatively high modulus of elasticity compared to ductile materials.

The modulus of elasticity for a material can be found by standardized testing methods. Tensile testing of a dogbone specimen is one of those standardized tests. Figure 3.1 shows a typical relationship between stress and strain. The modulus of elasticity, E, is the slope that describes the relationship between stress σ and ε.
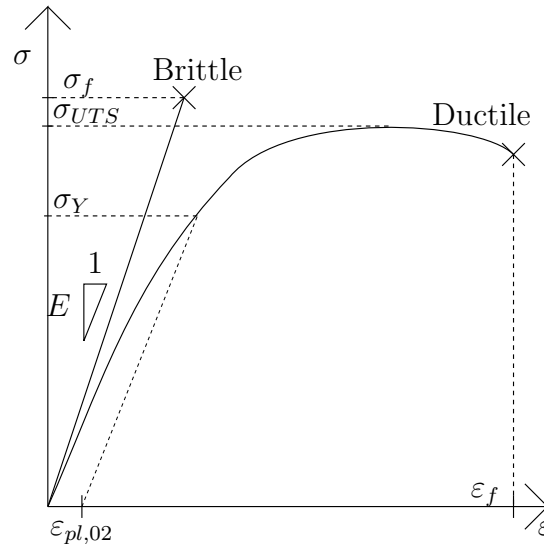
Figure 3.1: Stress-strain relationship curves both brittle and ductile.

A linear elastic

3.1.4   Poissons' ratio

Possions' ratio is the relationship between transverse strain and longitudinal strain. For a tensile test, when longitudinal load is applied, strain in the direction of loading is

$$\varepsilon_x = \frac{\Delta L}{L_i} \tag{3.2}$$

where ΔL is the change of length and L_i is initial length of the specimen. Similarily, because of the elongation the specimen becomes thinner and strain in the transverse direction is

$$\varepsilon_y = \varepsilon_z = \frac{\Delta d}{d_i} \tag{3.3}$$

where Δd is the change in width and d_i is the initial width. Usually, *strain gauges* are used to accurately measure these strains. Strain gauges are electrical sensors that use change in resistance to determine strain.

If a material has is linear elastic, two *elastic constants* can characaterize the linear properties of a material, namely the Poisson's ratio ν and the elastic modulus E.

$$\nu = -\frac{\text{transverse strain}}{\text{longitudinal strain}} = -\frac{\varepsilon_y}{\varepsilon_x} \tag{3.4}$$

3.1.5 Yield stress

Yield stress σ_Y is the point where the deformation of material no longer is elastic, or non-permanent, meaning the deformation is *plastic*. This usually means a small increase in stress gives relatively large additional deformation. Since the onset of plastic deformation is a question of scale, it is convention to use an offset point to define yield stress. The stress level which gives a plastic deformation of 0.2% is the yield stress, see figure 3.1.

3.1.6 Ultimate tensile strength

The ultimate tensile strength (UTS), σ_U, of a material is the highest level of stress reached before fracture. For brittle materials, it is the stress level at which fracture occurs, at $\varepsilon = \varepsilon_f$. In other words, $\sigma_{UTS} = \sigma_f$ where σ_f is the *engineering fracture strength*. For more ductile materials, UTS and engineering fracture strength occurs at different stress levels, see figure 3.1.

3.1.7 Flexural testing of ceramics

Ceramics is a difficult material to test because it often requires special tools to manufacture test specimens since regular machining tools are inadequate. Pre-cracking specimens for fatigue or fracture testing can be relatively time consuming compared to traditional metals. Additionally, because of ceramics' relatively brittle nature, tensile testing usually yield bad results. The same is said for fracture and fatigue testing, it is harder to achieve stable crack growth for most testing machines and specimen preparation. Testing methods have therefore been developed to specifically overcome the difficulties of testing ceramics.

For ceramics, elasticity is tested differently compared to traditional metals. It is difficult to prepare specimen with required geometry, gripping the specimen often results in cracking and most ceramics fail after 0.1% strain which requires the tensile specimen to be accurately aligned to avoid bending [35]. The measured fracture strength of ceramic materials are significantly lower than theoretical strength from ineratomic bonding forces [3], and can be explained by microscopic flaws in the material that acts as stress raisers, see section 3.2. These factors lead to poor results for tensile testing of ceramic material. The measured fracture strength of ceramic materials

Three- or four-point bending tests can be used to test strength and elastic modulus of ceramics. The test specimen is rectangular or a rod. One side of the specimen is subjugated to tensile stress and the other compressive stress, and maximum stresses are computed by geometry, bending moment and moment of inertia of the cross section. Flectural strength σ_{fs} is the stress at fracture and eq. 3.5a shows the equation for a rectangular cross section and eq. 3.5b is the equation for circular cross section.

$$\sigma_{fs} = \frac{3F_f L}{2bd^2} \tag{3.5a}$$

$$\sigma_{fs} = \frac{F_f L}{\pi R^3} \tag{3.5b}$$

The fracture load is F_f, L is the distance of support points in bending tests, b, d, R is cross section dimensions.

The bending tests also reveal linear elastic behaviour between stress and strain, making

it possible to obtain the elastic modulus. The elastic modulus from bending test E_b is

$$E_b = \frac{L^3}{32td^2} \left(\frac{dP}{dv} \right) \tag{3.6}$$

where v is the maximum deflection point of the specimen in bending, other words measured at the point of loading, $L/2$.

Both elastic modulus and fracture strength should be denoted to clarify that values are obtained by bending testing.

3.2   Basic concepts of fracture mechanics

3.2.1   Types of crack growth

Crack growth is mechanically different for brittle and ductile materials. *Ductile crack growth* usually consists of a void nucleation around an inclusion particle or second-phase particle. Because of hydro-static stress and plastic strain, the voids grow larger and larger until the strains around the voids cause necking towards other voids. The voids then joins and fracture occurs.

Cleavage fracture can be defined as rapid propagation of crack growth that consists of the crack growing along the crystollagraphic planes that have the smallest packing density. The crack grows in the directions that requires the least energy since fewer atomic bonds is broken. Cleavage is transgranular for polycrystalline materials, meaning that it grows through the grains of a material. At each grain boundary, the cleavage plane re-orients since the slip systems are not compatible between grains. This re-orientation creates *river patterns* that can be seen in SEM fractographs.

Cleavage is a mechanism that is most likely when plastic flow is restricted. Face centered cubic crystals usually have void nucleation fracture since there are ample slip systems for ductile crack growth. Body centered crystals tend to have cleavage fracture at low temperatures since slip systems are limited at lower temperatures. For cleavage to initiate, microscopic flaws must be present ahead of the macroscopic crack front. The microscopic flaw acts as a stress raiser that induce sufficient stress to exceed the bond strength of atoms. The microscopic flaws can be microcracks on the surface or on the interior, pores or grain corners or inclusion atoms.

Intergranular fracture is cracks forming and propegating along grain boundaries. There is no single mechanism that cause intergranular fracture as it can be cause by enviromental assisted cracking, intergranular corrosion and grain boundary cavitation and cracking at high temperatures for example. Intergranular fracture is easily identified as the crack surface typically consists of grains.

3.2.2   Crack propegation in ceramic materials

Both crystalline and non-crystalline ceramics have mostly brittle fracture before any plastic deformation can occur in tensile testing. In crystalline ceramics, the crack growth is either transgranular or intergranular.

The measured fracture strengths are typically substantially lower than predicted strength from theory of interatomic bonding forces. It can be explained by the ever present flaws previously mentioned. The flaws are a product of production and can not be eliminated.
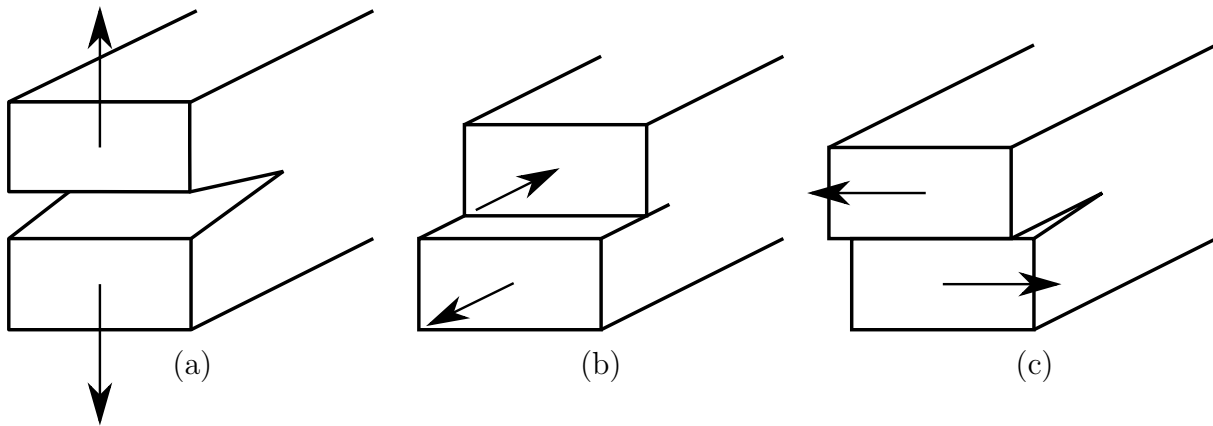
Figure 3.2: The three modes of loading that can be applied to a crack is (a) Mode I, (b) Mode II, and (c) Mode III.

In addition to the rapid crack growth that is observed from cleavage and intergranular fracture, *delayed fracture* describes subcritical crack growth occuring when loaded to less than critical load and static loading. Subcritical crack growth is specifically sensitive to the environmental conditions present and would typically be intergranular crack propegation. When the crack is in a state of loading, environmentally assisted crack growth occurs sharpening and lengthening the crack which eventually raises the stress around the crack tip to critical levels. Additionally, increased stress reduce the time at which SCCG induce failure, so loading should be specified when delayed fracture strength is determined.

3.2.3 Linear-elastic and elastic-plastic fracture mechanics

In this thesis, linear elastic fracture mechanics is mainly described by the singularity $1/\sqrt{r}$ which cause an asymptote at $r = 0$ and infitely large stress at the crack tip. This description is only valid when the non-linear deformation zone around the crack tip is relatively small compared to the relevant dimensions. In other words, the singularity is only correctly describing the stress around the crack tip when the material behaves like a linear elastic material, see section 3.1.3.

For many materials LEFM is not accurately describing the behaviour of fracture since the material exhibit time-independent, nonlinear behaviour, or plastic deformation. One of the most used ways to describe the plastic behaviour is using J contour integral which can give size independent measures of fracture toughness even when deformation zones around the crack tip are relatively large. J contour integrals of course also has its limits, but can within its limits describe the crack tip conditions.

When discussing fracture mechanics, it is useful to talk about what type of loading the crack withstands. Figure 3.2 illustrates how mode I is crack opening, mode II is in-plane shear forces acting on the crack and mode III is out-of plane shear forces acting on the crack.

3.2.4 Plastic zone

Since crack tip must have a finite radius, the stress state at the crack tip can not be infinitely large as by the $1/\sqrt{r}$ singularity. Nonlinear material deformation such as plasticity in a metal leads to relaxation of the stress at the crack tip within a certain area. This

relaxation area is called the *plastic zone.* It can be convenient to divide the area in front of the crack tip in different zones. Small-scale yielding can be described by using both stress intensity factor K and J contour integral, though they describe the conditions at different size of scale. The parameter K is only valid outside the plastic zone, it still accurately describes the crack conditions because the plastic zone is small. In the plastic zone, J contour integral describes the crack conditions and the stress vary with $r^{-1/(n+1)}$. If the plastic zone increase, K is not suited for describing the crack tip conditions while J contour integral still is approximately valid. When there is excessive plasticity or significant crack growth, J contour integral also becomes non-valid crack fracture criterion.

When the crack tip stress conditions are described by the parameter stress intensity factor K, it is known as *K-controlled fracture.* When described by the J contour integral, it is knows as *J-controlled fracture.*

3.3   Plane continuum mechanics

The problem of this thesis is plane in nature, so it is useful to define the terms that is the foundation of linear elastic fracture mechanics. It is assumed that the material and method is within the restrictions of two-dimensional stress state, isotropic material and isothermal deformation. A polar coordinate system is used for easier representation of stress states when using MTS, GMTS and ASED as fracture criterions.

Continuum mechanics is the modelling of materials as a continuous matter instead of discrete particles. The particles are on a size of scale much smaller than what engineering design usually encompass. The modelling of material as continuous is highly accurate when discussing size much larger than inter-atomic distance.

Strain (repeated in this section for clarity, see section 3.1) is defined as deformation from a reference configuration to the current configuration. It is useful to define strain for different directions as

$$\varepsilon_{rr} = \frac{\partial u_r}{\partial r} \tag{3.7a}$$

$$\varepsilon_{\theta\theta} = \frac{u_r}{r} + \frac{1}{r}\frac{\partial u_\theta}{\partial \theta} \tag{3.7b}$$

$$\varepsilon_{r\theta} = \frac{1}{2}\left(\frac{1}{r}\frac{\partial u_r}{\partial \theta} + \frac{\partial u_\theta}{\partial r} - \frac{u_\theta}{r}\right) \tag{3.7c}$$

where ε_{ij} is the strain component in the given direction, and u_r and u_θ are respectively the radial and tangential displacement components.

Stress is the physical quantity describing the internal forces that neighbouring particles of a continuous material exert on each other, see further clarification in section 3.1. A definition is a physical description of stress is the internal resistance to deformation. For

plane strain, the relationship between strain and stress is

$$\sigma_{rr} = \frac{E}{(1+\nu)(1-2\nu)}[(1-v)\varepsilon_{rr} + \nu\varepsilon_{\theta\theta}] \tag{3.8a}$$

$$\sigma_{\theta\theta} = \frac{E}{(1+\nu)(1-2\nu)}[(1-v)\varepsilon_{\theta\theta} + \nu\varepsilon_{rr}] \tag{3.8b}$$

$$\tau_{r\theta} = \frac{E}{1+\nu}\varepsilon_{r\theta} \tag{3.8c}$$

$$\sigma_{zz} = \nu(\sigma_{rr} + \sigma_{\theta\theta}) \tag{3.8d}$$

$$\varepsilon_{zz} = \varepsilon_{rz} = \varepsilon_{\theta z} = \tau_{rz} = \tau_{\theta z} = 0 \tag{3.8e}$$

By enforcing equilibrium of forces acting on an infinitesimal sized material element one obtains the *equilibrium equations*.

$$\frac{\partial\sigma_{rr}}{\partial r} + \frac{1}{r}\frac{\partial\tau_{r\theta}}{\partial\theta} + \frac{\sigma_{rr} - \sigma_{\theta\theta}}{r} = 0 \tag{3.9a}$$

$$\frac{1}{r}\frac{\partial\sigma_{\theta\theta}}{\partial\theta} + \frac{\partial\tau_{r\theta}}{\partial r} + \frac{2\tau_{r\theta}}{r} = 0 \tag{3.9b}$$

Note that eqs. 3.9 is with the absence of *body forces*, for example the absence of gravitational force. To guarantee a tensor field that is continuous and single-valued, a *compatibility equation* is needed. That is,

$$\nabla^2(\sigma_{rr} + \sigma_{\theta\theta}) = 0 \tag{3.10}$$

The Airy stress function is a *scalar* function Φ which should be chosen so that it always has the following property

$$\nabla^4\Phi = 0 \tag{3.11}$$

since this satisfies the equilibrium and compatibility equations. The operator ∇ is defined as

$$\nabla = \frac{\partial}{\partial r}\hat{\boldsymbol{r}} + \frac{1}{r}\frac{\partial}{\partial\theta}\hat{\boldsymbol{\theta}} \tag{3.12a}$$

$$\nabla^2 = \frac{\partial^2}{\partial r^2} + \frac{1}{r}\frac{\partial}{\partial r} + \frac{1}{r^2}\frac{\partial^2}{\partial\theta^2} \tag{3.12b}$$

Equations 3.9-3.11 allow us to write the stress components as functions of the stress function Φ.

$$\sigma_{rr} = \frac{1}{r^2}\frac{\partial^2\Phi}{\partial\theta^2} + \frac{1}{r}\frac{\partial\Phi}{\partial r} \tag{3.13a}$$

$$\sigma_{\theta\theta} = \frac{\partial^2\Phi}{\partial r^2} \tag{3.13b}$$

$$\tau_{r\theta} = \frac{1}{r}\frac{\partial^2\Phi}{\partial r\partial\theta} + \frac{1}{r^2}\frac{\partial\Phi}{\partial\theta} \tag{3.13c}$$

3.4   Linear Elastic Fracture Mechanics

3.4.1   Stress concentrations at the crack tip

Closed-form expressions for stresses in a cracked body can be derived, assuming isotropic linear elastic material behaviour. The reason cracks are critical to engineering design is that there exists a $1/\sqrt{r}$ singlularity for elastic crack problems. This is a universal behaviour and independent of crack configuration. The stress field in any linear elastic cracked body can be written as

$$\sigma_{ij} = \left(\frac{k}{\sqrt{r}} \right) f_{ij}(\theta) + \sum_{m=0}^{\infty} A_m r^{m/2} g_{ij}^{(m)}(\theta) \tag{3.14}$$

where σ_{ij} is the stress tensor, r and θ is defined as seen in figure 3.4, k is a constant usually replaced by a definition containing the stress intensity factor and f_{ij} a dimensionless function. The higher order terms tend to zero or remain finite, while the first term approaches infinity.

By convention, k is usually defined as

$$k = \frac{K_{(\text{I,II,III})}}{\sqrt{2\pi}} \tag{3.15}$$

even though π is superfluous. The parameter K is defined by the mode of loading and geometry of the crack (i.e. through crack, penny crack and edge crack). Figure 3.2 shows the different types of mode of loading.

Williams' approach [36] [37] is one of the easiest to understand mathematically and is shown in this section. Williams was among the first to show the universal relationship of $1/\sqrt{r}$ singularity. Consider a crack defined by ψ as seen in fig. 3.3 with $\psi = 2\pi$ and traction free surfaces.

The stress functions for such a crack was shown to be

$$\begin{aligned}\Phi &= r^{\lambda+1} \left[c_1 \sin{(\lambda+1)\theta^*} + c_2 \cos{(\lambda+1)\theta^*} + c_3 \sin{(\lambda-1)\theta^*} + c_4 \cos{(\lambda-1)\theta^*} \right] \\ \Phi &= r^{\lambda+1} F(\theta^*, \lambda)\end{aligned} \tag{3.16}$$

where $c_i(i = 1, 2, 3, 4)$ are constants, θ^* is the angle shown in fig. 3.3 and λ is a constant determined by the crack configuration and boundary conditions. Using equations 3.13 for σ_{rr}, $\sigma_{\theta\theta}$ $\tau_{r\theta}$ presented in section 3.2 gives expressions for the stresses:

$$\sigma_{rr} = r^{\lambda-1}[F''(\theta^*) + (\lambda+1)F'(\theta^*)] \tag{3.17a}$$

$$\sigma_{\theta\theta} = r^{\lambda-1}[\lambda(\lambda+1)F(\theta^*)] \tag{3.17b}$$

$$\tau_{r\theta} = r^{\lambda-1}[-\lambda F'(\theta^*)] \tag{3.17c}$$

where the primes of F denote derivation with respect to θ^*. Williams also included expressions for displacements. The continuity of displacements require that $\lambda > 0$, meaning that displacements are finite. For free-free edges of the problem, or in other words traction free surfaces,

$$\sigma_{\theta\theta}(0) = \sigma_{\theta\theta}(2\pi) = \tau_{r\theta}(0) = \tau_{r\theta}(2\pi) = 0 \tag{3.18}$$

or

$$F(0) = F(2\pi) = F'(0) = F'(2\pi) = 0 \tag{3.19}$$
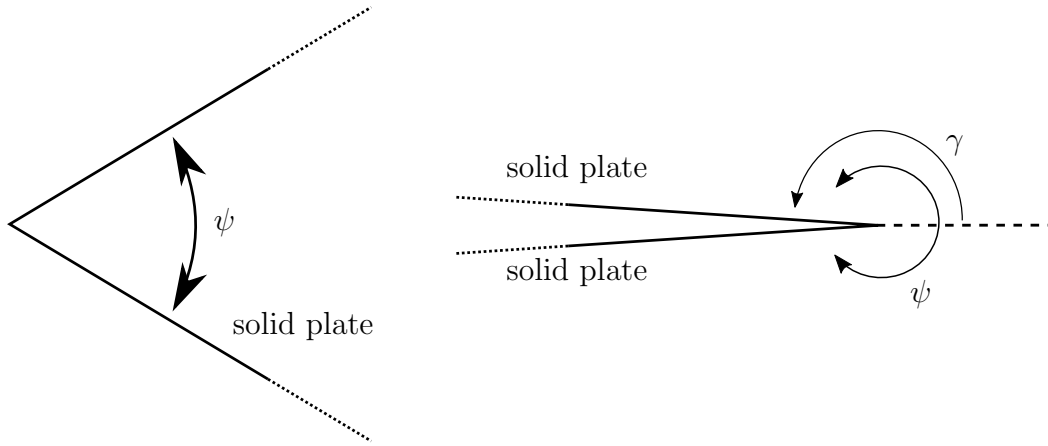
Figure 3.3: The parameters describing the Williams crack plate. Note that the parameter γ is later used for ASED.

which makes the four equations homogeneous. If the constants c_i are non-zero for the general case, the boundary conditions are satisfied when $\sin(2\pi\lambda) = 0$, giving

$$\lambda = \frac{n}{2}, \qquad\qquad \text{where } n = 1, 2, 3...$$

When $\psi = 2\pi$ all four boundary conditions can be met and there are infinite values of λ that satisfy the boundary conditions. Constants c_1 and c_2 can be eliminated, resulting in

$$\Phi = r^{n/2+1}\left\{ c_3\left[\sin\left(\frac{n}{2}-1\right)\theta^* - \frac{n-2}{n+2}\sin\left(\frac{n}{2}+1\right)\theta^*\right]\right.$$
$$\left. + c_4\left[\cos\left(\frac{n}{2}-1\right)\theta^* - \frac{n-2}{n+2}\cos\left(\frac{n}{2}-1\right)\theta^*\right]\right\} \quad (3.20)$$

It is more suitable to express the stress function in terms of bisector angle, $\theta = \theta^* - \pi$. Simultaniously writing out the first few values of n yields:

$$\Phi = r^{3/2}\left[s_1\left(-\cos\frac{\theta}{2} - \frac{1}{3}\cos\frac{3\theta}{2}\right) + t_1\left(-\sin\frac{\theta}{2} - \sin\frac{3\theta}{2}\right)\right]$$
$$+ s_2 r^2[1 - \cos 2\theta] + O(r^{5/2}) + ... \quad (3.21)$$

where s_1 and t_1 are constants to be defined. The associated stresses is found from equations 3.13 as

$$\sigma_{rr} = \frac{1}{4\sqrt{r}}\left\{s_1\left[-5\cos\frac{\theta}{2}+\cos\frac{3\theta}{2}\right) \right] + t_1\left[-5\sin\frac{\theta}{2}+3\sin\frac{3\theta}{2}\right)\right]\right\} + 4s_2\cos\theta^2 + O(r^{1/2}) + \cdots$$

$$(3.22a)$$

$$\sigma_{\theta\theta} = \frac{1}{4\sqrt{r}}\left\{s_1\left[-3\cos\frac{\theta}{2}-\cos\frac{3\theta}{2}\right] + t_1\left[-3\sin\frac{\theta}{2}-3\sin\frac{3\theta}{2}\right)\right]\right\} + 4s_2\sin\theta^2 + O(r^{1/2}) + \cdots$$

$$(3.22b)$$

$$\tau_{r\theta} = \frac{1}{4\sqrt{r}}\left\{s_1\left[-\sin\frac{\theta}{2}-\sin\frac{3\theta}{2}\right] + t_1\left[\cos\frac{\theta}{2}+3\cos\frac{3\theta}{2}\right]\right\} - 2s_2\sin 2\theta + O(r^{1/2}) + \cdots$$

$$(3.22c)$$
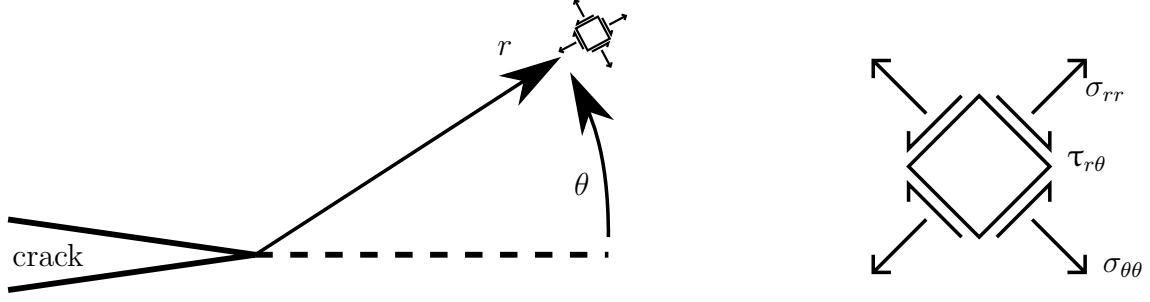
Figure 3.4: Unit element in front of a crack tip. The stress state of the unit element is described by equations 3.23 and 3.24.

Constants s_i are multiplied by cosine terms and t_i are multiplied by sine terms. The stress function has symmetric and anti-symmetric terms with regard to $\theta = 0$. Pure bending or pure tension with principal stress normal to the crack plane are examples of a load case symmetric about $\theta = 0$. For these cases, the terms of t_i are zero. For pure anti-symmetric loading with respect to $\theta = 0$, in-plane shear stress is applied on the crack faces and $s_i = 0$. Pure symmetric corresponds to Mode I loading, while pure anti-symmetric is Mode II loading. Assuming the higher order terms are negligible and using $s_1 = -k = K_I/\sqrt{2\pi}$ and $t_1 = k = K_{II}/\sqrt{2\pi}$ in equations 3.22, the crack tip stresses for Mode I can be written

$$\sigma_{rr} = \frac{K_I}{4\sqrt{2\pi r}} \left[5\cos\frac{\theta}{2} - \cos\frac{3\theta}{2} \right] \tag{3.23a}$$

$$\sigma_{\theta\theta} = \frac{K_I}{4\sqrt{2\pi r}} \left[3\cos\frac{\theta}{2} + \cos\frac{3\theta}{2} \right] \tag{3.23b}$$

$$\tau_{r\theta} = \frac{K_I}{4\sqrt{2\pi r}} \left[\sin\frac{\theta}{2} + \sin\frac{3\theta}{2} \right] \tag{3.23c}$$

while the crack tip stresses for Mode II is written

$$\sigma_{rr} = \frac{K_{II}}{4\sqrt{2\pi r}} \left[-5\sin\frac{\theta}{2} + 3\sin\frac{3\theta}{2} \right] \tag{3.24a}$$

$$\sigma_{\theta\theta} = \frac{K_{II}}{4\sqrt{2\pi r}} \left[-3\sin\frac{\theta}{2} - 3\sin\frac{3\theta}{2} \right] \tag{3.24b}$$

$$\tau_{r\theta} = \frac{K_{II}}{4\sqrt{2\pi r}} \left[\cos\frac{\theta}{2} + 3\cos\frac{3\theta}{2} \right] \tag{3.24c}$$

It is important to note that equations 3.23 and 3.24 is only valid for stresses near the crack tip where the first term, and thus the $1/\sqrt{r}$ singularity dominates. For stress fields further from the crack tip, the higher order terms needs to be taken into consideration.

The individual contributions to a stress state is additive, in so that

$$\sigma_{ij}^{total} = \sigma_{ij}^{I} + \sigma_{ij}^{II} + \sigma_{ij}^{III} \tag{3.25}$$

where σ_{ij} are the same stresses components from different modes of load. The tangential stress can be written

$$\sigma_{\theta\theta} = \frac{K_I}{4\sqrt{2\pi r}} \left[3\cos\frac{\theta}{2} + \cos\frac{3\theta}{2} \right] + \frac{K_{II}}{4\sqrt{2\pi r}} \left[-3\sin\frac{\theta}{2} - 3\sin\frac{3\theta}{2} \right] \tag{3.26}$$
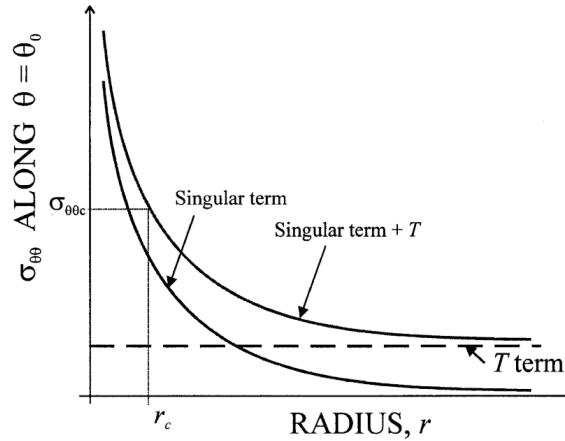
Figure 3.5: Elastic tangential stress along the crack - figure taken from Smith et al. [38]

and similarly for σ_{rr} and $\tau_{r\theta}$. The stress components are defined on the unit element in front of crack tip in figure 3.4.

3.4.2 Higher order terms of stress fields: T-stress

For equations 3.23 and 3.24 the higher order of stress field equations are neglected and the stress fields are dependant on the singularity $1/\sqrt{r}$. The higher order terms can be included and necessary as some crack propegation mechanisms are dependant on the stress level a critical distance R_c from the crack tip. The third and higher terms of Williams' solution vanish at the crack tip, but the second order is finite. Finite meaning that the stress is independent on distance from the crack tip and thus the second order term can affect the plastic zone shape and the stresses in the plastic zone.

The higher order terms (3rd and higher) can also affect the stress-controlled brittle fracture, as shown by Chao and Zhang [39]. Berto and Lazzarin have derived up to the seventh order for mode I and II loading [40]. The inclusion terms higher than second can be needed under certain conditions (e.g. low sheet thickness in lap joints) for valid results.

For a crack in a body of isotropic elastic material for plane strain Mode I loading, the first two terms can be written

$$\sigma_{ij} = \frac{K_{\mathrm{I}}}{\sqrt{2\pi r}} f_{ij}(\theta) + \begin{bmatrix} T & 0 & 0 \\ 0 & 0 & 0 \\ 0 & 0 & \nu T \end{bmatrix} \tag{3.27}$$

where T is a stress along the crack plane $\theta = 0$ which induce a stress in the direction of the thickness for plane strain.

As seen from equation 3.27, T-stress can increase or decrease the stress levels near the crack tip. For a through-thickness crack in an infinite plate, a remote normal stress induce a negative T-stress along the direction of the crack plane. For high levels of T-stress, using stress intensity factor for characterising crack-tip behaviour can be inaccurate [3].

The topic of T-stress is further discussed in relation with the GMTS criterion in section 3.6.

3.4.3 Triaxility, thickness and shear lips

Triaxility plays an important role for fracture mechanics, as it is a factor that decides whether or not it is plane strain or plane stress state near the crack tip. Considering a plate without a crack loaded in one direction, the whole plate is in the state of plane stress, meaning there is no stress component σ_{zz} in the direction of the thickness B.

For a plate with a crack, regions sufficiently far away from the crack tip is also in plane stress. However, close to the crack tip stress concentrations occur, meaning the stress normal to the crack plane are relatively high compared to far away from the crack. The material near the crack tip want to contract because of these heightened stress state, but is hindered because of surrounding material. This constraint causes a *triaxial state* of stress near the crack-tip [3], and is considered plane strain.

The surfaces of such a plate mentioned here are free, meaning $\sigma_{zz} = 0$. The closer to the surface, $\sigma_{zz} \rightarrow 0$, meaning that in the middle of the plate, there will be a state of high triaxility.

The material parameter of $K_{\text{I,c}}$ is somewhat arbitrary. When measuring K_{crit}, the stress intensity factor at failure, the value decrease with a specimen thickness until a plateu is reached. After this point, increasing the thickness of test specimen does not alter the measured value. It is the value of this asymptote that is $K_{I,c}$. The value is referred to as plane strain fracture toughness. It is not only dependent on the change from plane stress to plane strain conditions, but also on *microvoid coalescence* (section 3.2. There will always be a zone of high triaxility even in a thin fractured specimen with pure shear lips.

The shear lips that are typically seen in fracture test specimens after fracture does not occur if the a side-grooved specimen is used.

3.4.4 Dimensionless geometric constant Y

There are closed stress intensity factor solutions for simple cracks such as rectangle or ellipse in infinite size plates, meaning that the cracks are in very small size compared to the size of the specimen. When physically testing material, it is cost beneficial to have small specimen and thus crack geometry are not small compared to size anymore. Results from finite element analysis can be fitted to a polynomial to get accurate solutions of many different crack geometry and loading conditions.

In general, the stress intensity factor can be related to a through crack with a correction factor:

$$K_{\text{I,II,III}} = Y\sigma\sqrt{\pi a} \qquad (3.28)$$

where Y is a dimensionless constant that depend on geometry and loading condition.

3.4.5 Mixed mode fracture

The stress intensity factors for linear elastic materials are additive as long as the mode of loading is the same, meaning

$$K_{\text{I}}^{total} = K_{\text{I}}^{A} + K_{\text{I}}^{B} + K_{\text{I}}^{C} \qquad (3.29)$$

Stress intensity factors for mode I and II are not simply additive. For this thesis only Mode I and II is considered, meaning that it is a plane mixed mode fracture problem,

see section 3.2. As seen from equations 3.23 and 3.24, the stress field at the crack tip is determined by the stress intensity factors K_I and K_II. The crack growth can generally be stable or unstable depending on the loading pattern. For this thesis and the experiments performed, unstable crack growth is expected since the material is brittle.

The *Crack propegation direction* is not as straightforward for mixed mode loading as it is for pure mode I, see figure 3.6. MTS and GMTS both predict this direction and the accuracy is increased when also including higher order terms of the stress function.

Damage zone for ceramics is often considered a zone containing a large number of microcracks. For brittle and quasi-brittle ceramics, crack propagation usually occurs when a damage zone exists because of applied load. When the load is increased, the density of microcracks ahead of the initial crack tip a_0 are increased and when the damage zone reaches fully development, brittle fracture occurs. The size of this zone can be approximated as the same value as the critical distance from the crack tip, R_c, which is used in MTS and GMTS. The critical distance from the crack tip is the point where the stress field is calculated to also include higer order terms other than the singularity term, see section 3.6.

Mode mixity, M_e, is a parameter describing the relationship between the different stress intensity factors of different modes of loading. For plane strain problems the mode mixity is given by

$$M_e = \frac{2}{\pi} \arctan \frac{K_\mathrm{I}}{K_\mathrm{II}} \tag{3.30}$$

and is a useful parameter when describing fracture limit curves.

For pure Mode I loading, the crack growth becomes unstable if $K_\mathrm{I} \geq K_\mathrm{Ic}$. For a mixed mode problem with Mode I and Mode II loading, only considering K_I would lead to an underestimate of the fracture risk since the Mode II loading also contributes to stresses at the crack tip.

For this reason it is useful to utilise a fracture limit curve. The fracture limit curve is represented differently depending on the criterion used. For example, MTS and GMTS criterions fracture limits are usually represented using the stress intensity factors, see section 3.5 and figure 3.7a.

3.5 Maximum tangential stress criterion

The maximum tangential stress criterion was first proposed by Erdogan and Sih [41]. It reiterated two hypotheses for the extension of cracks which is repeated here in the words of Ayatollahi [42], namely

1. Fracture initiates radially from the crack tip in the direction along which the tangential stress posssesses its maximum value.

2. The onset of fracture occurs when the tangential stress at a critical radial distance from the crack tip, R_c, and along the above direction, reaches a critical value of $\sigma_{\theta\theta,c}$. Both R_c and $\sigma_{\theta\theta,c}$ are considered to be constant material properties.
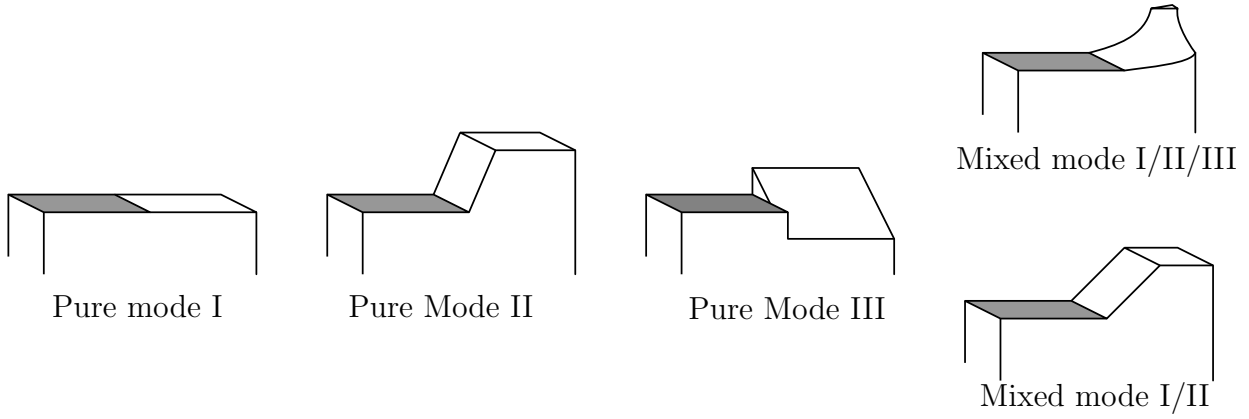
Figure 3.6: Crack propagation for mixed mode loading, derived from [43].

This means there exists an angle $\theta = \theta_0$ in which the crack propegates, when $\sigma_{\theta\theta} = \sigma_{\theta\theta,c}$. Another way to phrase the criterion is that if a comparative stress intensity factor K_{eq} resulting from $\sigma_{\theta\theta}$ exceeds the fracture toughness K_{Ic}. Mathematically, this can be written as

$$\left.\frac{\partial \sigma_{\theta\theta}}{\partial \theta}\right|_{\theta=\theta_0} = 0 \qquad\qquad \text{and} \qquad\qquad \left.\frac{\partial^2 \sigma_{\theta\theta}}{\partial \theta^2}\right|_{\theta=\theta_0} < 0, \qquad (3.31)$$

meaning a point of maxium tangential stress, where $\sigma_{\theta\theta}$ is as defined in equation 3.26. Rewritten to solve for θ_0

$$K_{\text{I}} \sin \theta_0 + K_{\text{II}}(3 \cos \theta_0 - 1) = 0 \qquad (3.32)$$

or

$$\theta_0 = -\arccos\left(\frac{3K_{\text{II}}^2 + K_{\text{I}}\sqrt{K_{\text{I}}^2 + 8K_{\text{II}}^2}}{K_{\text{I}}^2 + 9K_{\text{II}}^2}\right). \qquad (3.33)$$

For pure mode I, when the stress reach a level such that $K_{\text{I}} = K_{\text{I,c}}$, failure occurs. Defining the comparative stress intensity factor in similar fashion, as when $\sigma_{\theta\theta,c}$, the critical tangential stress at critical distance R_c, reaches a level so that $K_{\text{eq}} = K_{\text{I,c}}$, failure occurs. The expression can be written as

$$K_{\text{eq}}^{MTS} = \cos\frac{\theta_0}{2}\left[K_{\text{I}}\cos\frac{\theta_0}{2}^2 - \frac{3}{2}K_{\text{II}}\sin\theta_0\right] = K_{\text{Ic}} \qquad (3.34)$$

Ayatollahi [44] makes a point of showing how MTS (and other criterion based *only* on stress intensity factors) fail to accurately predict failure for a large number of ceramics. The discrepancy between prediction and the test data becomes increasingly large when comparing pure Mode I (for $M_e = 1$) to mixed mode loading ($1 > M_e > 0$) and to pure mode II ($M_e = 0$).

3.6   Generalized maximun tangential stress criterion

By including the higher order terms in equation 3.22, the stress distributions can be described further from the crack tip. Defining T-stress as $T = 4s_2$, one extra term can
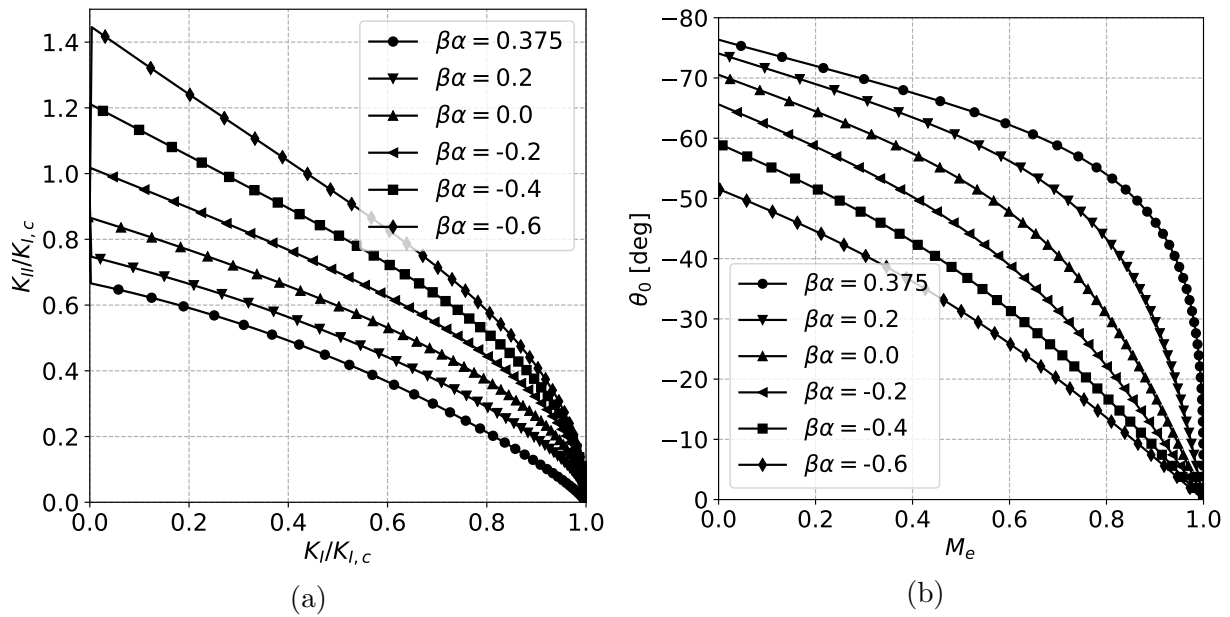
Figure 3.7: (a) shows the influence of T-stress on the fracture curve. (b) shows how the crack propegation angle differ with the influence of T-stress. For $\beta\alpha = 0$, $T = 0$ thus equaling the MTS criterion.

be included, and the equations for stress are extended to be valid further from the crack tip.

$$\sigma_{rr} = \frac{K_{\mathrm{I}}}{4\sqrt{2\pi r}}\left[5\cos\frac{\theta}{2} - \cos\frac{3\theta}{2}\right] + \frac{K_{\mathrm{II}}}{4\sqrt{2\pi r}}\left[-5\cos\frac{\theta}{2} + 3\cos\frac{3\theta}{2}\right] + T\cos^2\theta \qquad (3.35a)$$

$$\sigma_{\theta\theta} = \frac{K_{\mathrm{I}}}{4\sqrt{2\pi r}}\left[3\cos\frac{\theta}{2} + \cos\frac{3\theta}{2}\right] + \frac{K_{\mathrm{II}}}{4\sqrt{2\pi r}}\left[-3\sin\frac{\theta}{2} - 3\sin\frac{3\theta}{2}\right] + T\sin^2\theta \qquad (3.35b)$$

$$\tau_{r\theta} = \frac{K_{\mathrm{I}}}{4\sqrt{2\pi r}}\left[\sin\frac{\theta}{2} + \sin\frac{3\theta}{2}\right] + \frac{K_{\mathrm{II}}}{4\sqrt{2\pi r}}\left[\cos\frac{\theta}{2} + 3\cos\frac{3\theta}{2}\right] - T\sin\theta\cos\theta \qquad (3.35c)$$

This inclusion is an important inclusion to more precisely predict the fracture of materials [42] [45]. Figure 3.5 show how the tangential stress near the crack tip is influenced by the T-stress.

As before, K_{I}, K_{II} and T depend on the geometry and loading configurations. The values can vary by a considerable amount for different specimens. As with MTS, GMTS assume that crack initation happens when $\theta = \theta_0$ and $\sigma_{\theta\theta} = \sigma_{\theta\theta,c}$, while the fracture initiation should be investigated at critical distance R_c from the crack tip.

As mentioned in section 3.4.5, the crack propagation angle is non-zero ($\theta_0 \neq 0$) for mixed mode loading and thus T-stress has influence on the tangential stress $\sigma_{\theta\theta}$. This is along the direction of crack initiaion and will therefore influence the mixed mode fracture toughness. It is usual to normalize the T-stress with regards to the effective stress intensity factor, K_{eff} which is defined

$$K_{\mathrm{eff}} = \sqrt{K_{\mathrm{I}} + K_{\mathrm{II}}} \qquad (3.36)$$

and use the dimensionless biaxility ratio β to express the term containing T-stress, where

$$\beta = (T\sqrt{\pi a})/K_{\mathrm{eff}} \qquad (3.37)$$

and a is crack length. Expanding equation 3.32 to include the T-stress contribution, we write

$$K_\mathrm{I}\sin\theta_0 + K_\mathrm{II}(3\cos\theta_0 - 1) - \gamma_T \sin\frac{\theta_0}{2}\cos\theta_0 = 0 \tag{3.38}$$

where

$$\gamma_T = \frac{16}{3}(T\sqrt{2\pi R_c}) \tag{3.39}$$

The parameter R_c can be represented with the dimensionless parameter $\alpha = \sqrt{2R_c/a}$ [38], thus γ_T is written as

$$\gamma_T = \frac{16}{3}(\beta\alpha K_\mathrm{eff}) \tag{3.40}$$

where a, K_eff and B is defined as before. A comparative stress intensity factor is defined for GMTS as well, similary as for MTS. The onset of crack propegation can be found from

$$K_\mathrm{eq}^{GMTS} = \cos\frac{\theta_0}{2}\left[K_\mathrm{I}\cos\frac{\theta_0}{2}^2 - \frac{3}{2}K_\mathrm{II}\sin\theta_0\right] + \sqrt{2\pi R_c}T\sin\theta_0^2 = K_\mathrm{I,c} \tag{3.41}$$

or using the normalised terms for B, from

$$K_\mathrm{eq}^{GMTS} = \cos\frac{\theta_0}{2}\left[K_\mathrm{I}\cos\frac{\theta_0}{2}^2 - \frac{3}{2}K_\mathrm{II}\sin\theta_0\right] + B\alpha K_\mathrm{eff}\sin\theta_0 = K_\mathrm{I,c} \tag{3.42}$$

Smith et al. [38] shows in their appendix how both direction of initiation angle and mixed mode fracture curves can be plotted and figure 3.7 shows the variation by the method presented.

As seen in equation 3.35b, for pure mode I, T-stress is zero in front of the crack tip. It would seem the T-stress has no effect if the crack propagates along the crack line ($\theta_0 = 0$). However, elastic-plastic materials' fracture toughness is affected by T-stress. T-stress' non effect on mode I loading is only true for linear elastic materials with $-0.6 < \beta\alpha < 0.375$ [38]. For $\beta\alpha$ values greater than 0.375, the fracture angle is not zero.

In this thesis only second order considered; third order and higher is neglected.

3.7 Averaged strain energy density criterion

3.7.1 Basic of the SED approach

Strain energy density is a function describing the stored energy internal energy per unit volume in a body which is under deformation, i.e. work has been done. In a global 1-2-3 coordinate system, the stress is obtainable by taking the derivative of the strain energy density function W with respect to the strain.

$$W = \frac{1}{2E}\left[\sigma_{11}^2 + \sigma_{22}^2 + \sigma_{33}^2 - 2\nu(\sigma_{11}\sigma_{22} + \sigma_{11}\sigma_{33} + \sigma_{22}\sigma_{33}) + 2(1+\nu)\sigma_{12}\right] \tag{3.43}$$

where W is the strain energy, and the subscripts refer to stress components in a given reference system, such as a polar coordinate system. *Average strain energy density* $\overline{W}$ is simply total strain energy in the control volume divided by the control volume.

$$\overline{W} = E_s/V \tag{3.44}$$

which is a useful equation when the data is available. An analytic approach for cracks follows in section 3.7.2. The averaged strain energy density method utilise a material dependent structural volume combined while still being a energy based criterion. The base idea of SED is that when under relatively large tensile stresses, failure occurs when the strain energy density averaged over a control volume reaches a critical value. In other words, when $W = W_c$ failure occurs. The variable W_c is dependant on the material.

Berto and Lazzarin [4] gives a thorough overview of the volume-based ASED approach as a fracture criterion. Four criterions are presented as a basis for the development of the ASED method, namely

- Generalized maximum tangential stress criterion,

- Sih's criterion,

- Notch stress intensity factor criterion,

- Neuber's fictitious notch rounding approach.

The GMTS criterion is already presented in section 3.6.

Sih's criterion uses elastic energy density and near-field equations [43]. The criterion states that a crack extends, beginning from the crack tip, in the direction of the smallest *energy density factor*, S_{min}. The crack growth becomes unstable if S_{min} reaches critical value $S_{min,c}$ which is a material property.

Notch stress intensity factors is a method for evaluating both rounded and sharp notches based on Willams' solution for cracks, see section **??**. When the notch radius is non-zero, the solution is not valid from a theoreical point of view, but other solutions are proposed to also include effects of the rounded notch. The method is important for SED as SED can be used for other applications than sharp cracks. It is worth mentioning that for this thesis cracks with opening angle less than 60 °is used and therefore N-SIFs are considered equal to conventional SIFs of linear elastic fracture mechanics.

Neuber's fictitious notch rounding approach use a fictitious enlarged notch, enlarged by a certain amount determined by stress state. The approach propose that it is the averaged notch stress over a short distance normal to the notch edge which determine static or fatigue strength. The principles was further elaborated and refined until sound principles where established.

3.7.2 Theoretical background of SED

By defining $\psi \neq 2\pi$, the stress fields derived from Williams' approach can be applied for for sharp V-notches. Williams' solution can be solved to include stress distribution that are divided into symmetric type with regard to the bisector and skew-symmetric, analogous to mode I and mode II loading respectively. For mode I the stress distributions are
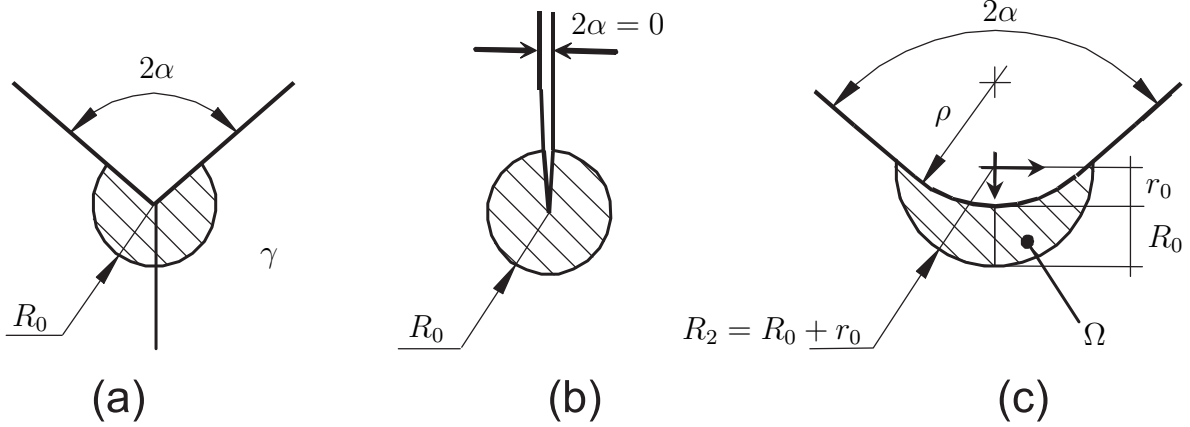
Figure 3.8: Critical control volume (or area) showing parameters crack notch variations for (a) sharp V-notch, (b) crack and (c) blunt V-notch for mode I loading. Retrieved from Berto and Lazzarin [4].

$$
\begin{Bmatrix} \sigma_{\theta\theta} \\ \sigma_{rr} \\ \sigma_{r\theta} \end{Bmatrix} = \frac{1}{\sqrt{2\pi}} \frac{r^{\lambda_1-1} K_1}{(1+\lambda_1) + \chi_1(1-\lambda_1)}
$$

$$
\cdot \left[\begin{Bmatrix} (1+\lambda_1)\cos(1-\lambda_1)\theta \\ (3-\lambda_1)\cos(1-\lambda_1)\theta \\ (1-\lambda_1)\sin(1-\lambda_1)\theta \end{Bmatrix} + \chi_1(1-\lambda_1) \begin{Bmatrix} \cos(1+\lambda_1)\theta \\ -\cos(1+\lambda_1)\theta \\ \sin(1+\lambda_1)\theta \end{Bmatrix} \right] \quad (3.45)
$$

while the stress distributions for mode II is

$$
\begin{Bmatrix} \sigma_{\theta\theta} \\ \sigma_{rr} \\ \sigma_{r\theta} \end{Bmatrix} = \frac{1}{\sqrt{2\pi}} \frac{r^{\lambda_2-1} K_2}{(1-\lambda_2) + \chi_2(1+\lambda_2)}
$$

$$
\cdot \left[\begin{Bmatrix} -(1+\lambda_2)\sin(1-\lambda_2)\theta \\ -(3-\lambda_2)\sin(1-\lambda_2)\theta \\ (1-\lambda_2)\cos(1-\lambda_2)\theta \end{Bmatrix} + \chi_2(1+\lambda_2) \begin{Bmatrix} -\sin(1+\lambda_2)\theta \\ \sin(1+\lambda_2)\theta \\ \cos(1+\lambda_2)\theta \end{Bmatrix} \right] \quad (3.46)
$$

Parameters K_1 and K_2 are the notch stress intensity factors related to mode I and mode II stress distributions respectively, λ_1 and λ_2 are the eigenvalues that solve Williams' stress function and χ_1 and χ_2 are parameters that depend on the opening angle, 2α. The opening angle is found by $2\alpha = 2\pi - \psi$. In other words, the stress fields have exact solutions for sharp V-notches.

As before, stress states are additive in so that

$$
\sigma_{ij}(r,\theta) = r^{\lambda_1-1} K_1 \tilde{\boldsymbol{\sigma}}^{(1)} + r^{\lambda_2-1} K_2^N \tilde{\boldsymbol{\sigma}}^{(2)} \quad (3.47)
$$

where $\tilde{\boldsymbol{\sigma}}^{(1)}$ and $\tilde{\boldsymbol{\sigma}}^{(2)}$ are matrices which components are derived from equations 3.45 and 3.46.

Substituting the explicit expressions for the stress distribution into equation 3.43, gives

$$
W = W_1(r,\theta) + W_2(r,\theta) + W_{12}(r,\theta) \quad (3.48)
$$

where $W_1(r,\theta)$, $W_2(r,\theta)$ and $W_{12}(r,\theta)$ are strain energy densities that depend on parameters relating to mode I, mode II or a combination of the two, respectively. The expressions for W_1, W_2 and W_{12} are lengthy and can be found in the review by Berto and Lazzarin [4].

The energy associated with deformation energy in a region around the notch or crack tip with radius R is

$$
\begin{aligned}
E_s(R) &= \int_A W\,dA \\
&= \int_0^R \int_{-\gamma}^{+\gamma} [W_1(r,\theta) + W_2(r,\theta) + W_{12}(r,\theta)]r \cdot dr d\theta
\end{aligned}
\tag{3.49}
$$

where γ is the angle between the symmetry line (bisector) and crack face, see figure 3.8. The integration field is symmetric with respect to the symmetry line ($\theta^* = 0$) and the contribution of W_{12} vanish. Note that θ^* and γ is the same parameter, but $\theta*$ is used by Williams. Thus equation 3.49 becomes

$$
\begin{aligned}
E_s(R) &= E_{s,1}(R) + E_{s,2}(R) \\
&= \frac{1}{E}\frac{I_1(\gamma)}{4\lambda_1}K_1^2 R^{2\lambda_1} + \frac{1}{E}\frac{I_2(\gamma)}{4\lambda_2}K_2^2 R^{2\lambda_2}.
\end{aligned}
\tag{3.50}
$$

The integrals $I_1(\gamma)$ and $I_2(\gamma)$ are

$$
I_1(\gamma) = \int_{-\gamma}^{+\gamma} (\tilde{\sigma}_{\theta\theta}^{(1)^2} + \tilde{\sigma}_{rr}^{(1)^2} + \tilde{\sigma}_{rr}^{(1)^2} - 2\nu(\tilde{\sigma}_{\theta\theta}^{(1)}\tilde{\sigma}_{rr}^{(1)} + \tilde{\sigma}_{\theta\theta}^{(1)}\tilde{\sigma}_{zz}^{(1)} + \tilde{\sigma}_{rr}^{(1)}\tilde{\sigma}_{zz}^{(1)}) + 2(1+\nu)\tilde{\sigma}_{r\theta}^{(1)^2})d\theta
\tag{3.51a}
$$

$$
I_2(\gamma) = \int_{-\gamma}^{+\gamma} (\tilde{\sigma}_{\theta\theta}^{(2)^2} + \tilde{\sigma}_{rr}^{(2)^2} + \tilde{\sigma}_{rr}^{(2)^2} - 2\nu(\tilde{\sigma}_{\theta\theta}^{(2)}\tilde{\sigma}_{rr}^{(2)} + \tilde{\sigma}_{\theta\theta}^{(2)}\tilde{\sigma}_{zz}^{(2)} + \tilde{\sigma}_{rr}^{(2)}\tilde{\sigma}_{zz}^{(2)}) + 2(1+\nu)\tilde{\sigma}_{r\theta}^{(2)^2})d\theta
\tag{3.51b}
$$

where the $\tilde{\sigma}_{ij}$ are components of the matrices mentioned in equation 3.47. The control volume (or area for plane problems) can be found by

$$
A(R) = \int_0^{R_0} \int_{-\gamma}^{+\gamma} r \cdot dr d\theta = R_0^2\gamma.
\tag{3.52}
$$

The elastic deformation energy E_s is averaged on the area A is

$$
\overline{W} = \frac{E_s(R)}{A(R)} = \frac{1}{E}e_1 K_1^2 R_0^{2\lambda_1-1} + \frac{1}{E}e_2 K_2^2 R_0^{2\lambda_2-1}
\tag{3.53}
$$

where e_1 and e_2 are functions that depend on geometry, more specifically the opening angle 2α, and the linear elastic material property ν:

$$
e_1(2\alpha) = \frac{I_1(\gamma)}{4\lambda_1\gamma} \qquad \text{and} \qquad e_2(2\alpha) = \frac{I_2(\gamma)}{4\lambda_2\gamma}
\tag{3.54}
$$

Rewriting $R_0^{2\lambda_i-1}$ as $(1/R_0^{1-\lambda_i})^2$, an expression for plane problem average strain energy density can be written:

$$
\overline{W} = \frac{e_1}{E}\left[\frac{K_1}{R_0^{1-\lambda_1}}\right]^2 + \frac{e_2}{E}\left[\frac{K_2}{R_0^{1-\lambda_2}}\right]^2
\tag{3.55}
$$

3.7.3 Application of ASED criterion for plane sharp crack problems

For the plane problems with cracks, the control volume is a sector or circle with a radius R_0. Yosibashi and Bussiba proposed [46]

$$R_0 = \frac{(1+\nu)(5-8\nu)}{4\pi} \left(\frac{K_{\text{I,c}}}{\sigma_{UTS}} \right)^2 \tag{3.56}$$

for plane strain, and

$$R_0 = \frac{(5-3\nu)}{4\pi} \left(\frac{K_{\text{c}}}{\sigma_{UTS}} \right)^2 \tag{3.57}$$

for plane stress where ν is the Poissons' ratio, σ_{UTS} is the ulitmate tensile strength and $K_{I,c}$ is the fracture toughness. K_c is apparent fracture toughness, see section **??**. These equations for R_0 is only valid for values $2\alpha = 0$.

A sharp V-notch with $2\alpha = 0$ is equivalent to a crack. Using the values from table 3.1 which are valid for $2\alpha = 0$ and as $K_1 = K_{\text{II}}$ and $K_2 = K_{\text{II}}$, equations 3.45 and 3.46 result in the stress distributions from Williams' approach, equations 3.23 and 3.24. Applying the values for λ_1, λ_2, e_1 and e_2 to equation 3.55 gives

$$\overline{W} = 0.13449 \frac{K_{\text{I}}^2}{ER_c} + 0.34139 \frac{K_{\text{II}}^2}{ER_c} \tag{3.58}$$

If values for K_{I}, K_{II}, E and R_0 are known, $\overline{W}$ can be calulcated. To avoid approximations, the strain energy and volume elements of the finite element model in Abaqus is used to calculate the average strain energy density.

The ASED criterion states that onset of fracture occurs when $W = W_c$. W_c can be determined by material parameters σ_{UTS} and elastic modulus E [4]:

$$W_c = \frac{\sigma_{UTS}^2}{2E} \tag{3.59}$$

Fracture load curves for specimen can be calculated without knowing the fracture initiation angle, unlike MTS and GMTS. This done by the relationship

$$P_{th}/P = \sqrt{W_c/W} \tag{3.60}$$

Table 3.1: Variable values for calculating average strain energy density with eq. 3.55 for $\nu = 0.3$ [4].

2α [rad]	γ [rad]	λ_1	λ_2	χ_1	χ_2	e_1	e_2
0	π	0.5	0.5	1	1	0.13449	0.34139

Chapter 4

Method

4.1 Asymmetric mixed mode testing by roller distance variation

The tested materials would be two 3mol% YSZ materials with different composition. The were 80 specimen with of 3x4x45 mm with 40 of each composition. Because of delay, fracture load curves of 3YSZ, 5YSZ and 8YSZ has been calculated instead for material data retrieved from Ming et al [25] if not otherwise stated (see table 4.1).

The test configuration can be seen in figure 4.3. Technical drawings for the ordered specimens can be seen in Appendix A. A four point bending test was performed to measure the fracture load of the cracked specimen. Choosing appropriate values of $L_i (i = 1, 2, 3, 4)$, where L_i is distance from the crack, gives different fracture loading modes. Choosing $L_1 = L_2$, $L_3 = L_4$ and $L_2 > L_4$, gives symmetric loading conditions and *pure mode I loading conditions*. In other words, pure bending and crack opening mechanism of the cracked specimen.

Choosing $L_1 = L_4$, $L_2 = L_3$ and $L_4 > L_2$, in other words anti-symmetric loading conditions, gives *pure mode II loading conditions*, which results in pure shear deformation in the crack plane, see figure 4.3(a).

For mixed mode I/II loading conditions, a set value was chosen for L_1, L_2 and L_3, while L_4 was varied between certain values. See section **??** for the different fracture modes. Mixed mode loading of this specimen can be characterized as asymmetric loading which leads to both crack opening and shear deformation in the crack plane, see figure 4.3(b).

The geometries and stress intensity factors are valid for pure mode I by standards ASTM C1421 [48] and ISO 23146 [49]. It is worth noting that a reviewed version of ISO 23146 (2018) specifically does not recommend using the standard for testing of tetragonal

Table 4.1: Material properties and calculated fracture criteria values for the simulated YSZ-materials taken from Li et al. [25]. Values marked with (*) is assumed.

	E (GPa)	σ_{fs} (GPa)	ν	ρ (nm)	$K_{I,c}$ (MPa$\sqrt{m}$)	R_c (mm)	R_0 (mm)	W_c (mJ/mm^3)
3YSZ	210	664	0.3*	437	4.4	0.0437	1.02E-02	1.050
5YSZ	243 [47]	272	0.3*	858	2.8	0.0858	2.85E-02	0.1522
8YSZ	213 [16]	166	0.3*	5133	1.6	0.513	2.49E-02	0.06469

YSZ.

The crack tip stress intensity factors for mixed mode I/II loading conditions can be written as a function of load, loading conditions, geometry and crack length [5]:

$$K_{\mathrm{I}} = \frac{P\sqrt{\pi a}Y_1}{BW}\left(1 - \frac{L_2}{L_4}\right) \tag{4.1a}$$

$$K_{\mathrm{II}} = \frac{P\sqrt{\pi a}Y_2}{BW}\left(1 - \frac{L_2}{L_4}\right). \tag{4.1b}$$

where P is applied load, a is crack length, B and W is thickness and width respectively and Y_i is the dimensionles constant dependent on geometry and mode of loading. For T-stress, the following equation is proposed:

$$T = \frac{PT^*}{B(W-a)}\left(1 - \frac{L_2}{L_4}\right) \tag{4.2}$$

Stress intensity factors are obtained by finite element analysis using Abaqus (see section 4.3) and used to calculate the geometric values $Y_i(i = 1, 2)$ and T^* seen in figure 4.2. For pure mode I, ASTM C1421 allows a ratio $0.6 > a/W > 0.35$ and so these upper and lower crack-width ratios are simulated and presented alongside the order ratio in figure 4.2.

In the attempt to cover mode mixity in the interval of $1 \geq M_e \geq 0$, appropriate roller distance values were chosen. Different distances from the crack to the rollers was simulated to study the effect of roller distance. As seen in figure 4.1a(a), $L_3 = L_2 = 10$ mm resulted in roller distances where small inaccuracies in the testing fixture roller distances would result in large variations in mode mixity M_e. A roller distance $L_3 = L_2 = 5$ mm was chosen as it allows larger intervals between L_4 for the chosen mode mixities. The tested mode mixities range from one to zero with intervals of 0.25 and the chosen values can be found in table 4.2.

The fracture toughness values $K_{\mathrm{I,c}}$ should first be obtained by symmetric four point bending so the control volume and fracture curves for the criterion can be calculated. A loading rate of 0.05 mm/min would be performed as it gives crack propagation before failure for 3-point-bending specimen of similar scale with 3YSZ [25]. Thereafter a loading rate of 0.03 mm/min is performed to confirm similar behaviour for the loading curve and that the loading rate is sufficiently slow.

The values of L_4 are varied to test different mode mixites. A total of three specimen are tested for each value M_e. The specimen would loaded until failure.

Table 4.2: Roller values corresponding to chosen mode mixities M_e.

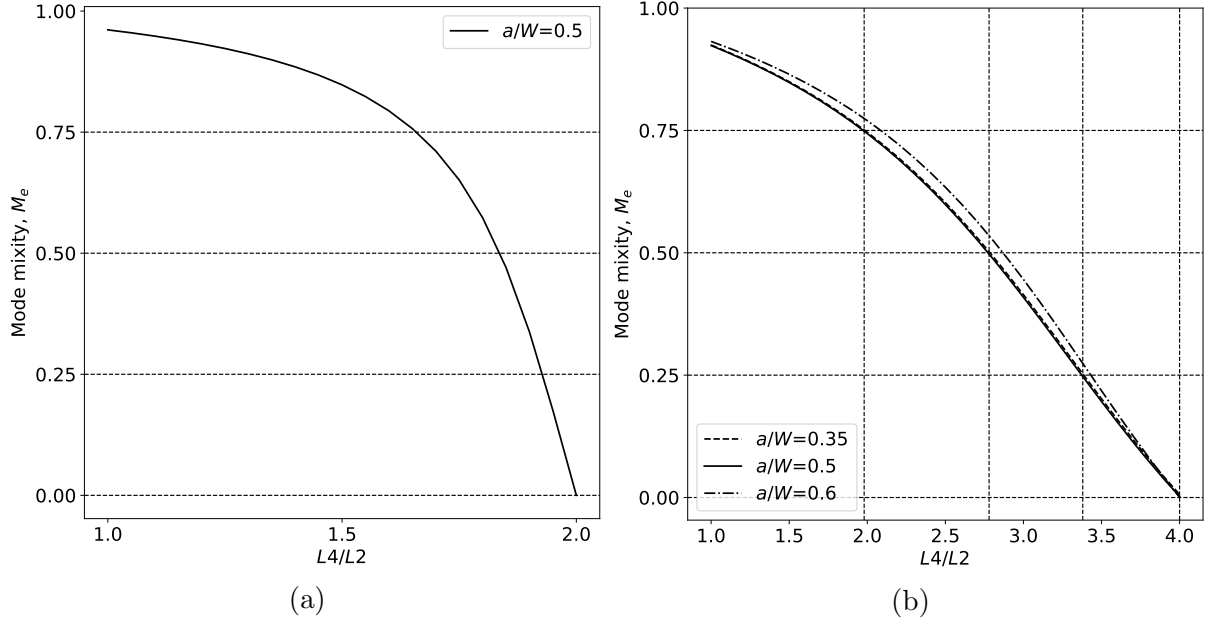| M_e	L_1 (mm)	L_2 (mm)	L_3 (mm)	L_4 (mm)
1.0	20	20	10	10.0
0.75	20	5	5	9.9
0.5	20	5	5	13.9
0.25	20	5	5	16.9
0.0	20	5	5	20

(a)

(b)

Figure 4.1: Mode mixity vs roller distance for (a) $L_3 = L_2$=10 mm and (b) $L_3 = L_2$=5 mm. The vertical lines in (b) shows which L_4 values that give the wanted mode mixities.

X-ray diffraction would be performed to obtain crystalline composition of the specimen. The relative density should also be acquired by archimedes method as the density will affect mechanical properties [17].

The fracture curves are calculated by the dimensionless geometry factors introduced in sections 4.1 and 4.2 since the geometry factors are independent of applied loads. The GMTS criterion is written

$$K_{\text{eq}}^{GMTS} = \cos \frac{\theta_0}{2} \left[K_{\text{I}} \cos^2 \frac{\theta_0}{2} - \frac{3}{2} K_{\text{II}} \sin \theta_0 \right] + \sqrt{2\pi r_c} T \sin \theta_0{}^2 = K_{\text{I,c}}. \qquad (4.3)$$

By dividing both sides by K_{eff} and inverting the equation, it can be written

$$\frac{K_{\text{eff}}}{K_{\text{I,c}}} = \frac{\sqrt{Y_{\text{I}}^2 + Y_{\text{II}}^2}}{Y_{\text{I}} \cos^3 \frac{\theta_0}{2} - \frac{3}{2} Y_{\text{II}} \sin 2\theta_0 \cos \frac{\theta_0}{2} + \sqrt{2r_c/a} \frac{T^*W}{W-a} \sin^2 \theta_0} \qquad (4.4)$$

The MTS criterion is similar, but with $T = 0$. Thus equation 4.4 without the term containing T^*.

The ASED criterion can be written as [45]:

$$\frac{K_{\text{I,c}}}{K_{\text{eff}}} = \sqrt{\frac{K_{\text{If}}}{K_{\text{eff}}} + \frac{2\kappa + 3}{2\kappa - 1} \frac{K_{\text{IIf}}}{K_{\text{eff}}}} \qquad (4.5a)$$

$$\frac{K_{\text{I,c}}}{K_{\text{eff}}} = \sqrt{\frac{1}{Y_{\text{I}}^2 + Y_{\text{II}}^2} \left(Y_{\text{I}}^2 + \frac{2\kappa + 3}{2\kappa - 1} Y_{\text{II}}^2 \right)} \qquad (4.5b)$$

where $\kappa = 3 - 4\nu$.

(a)

(b)

(c)

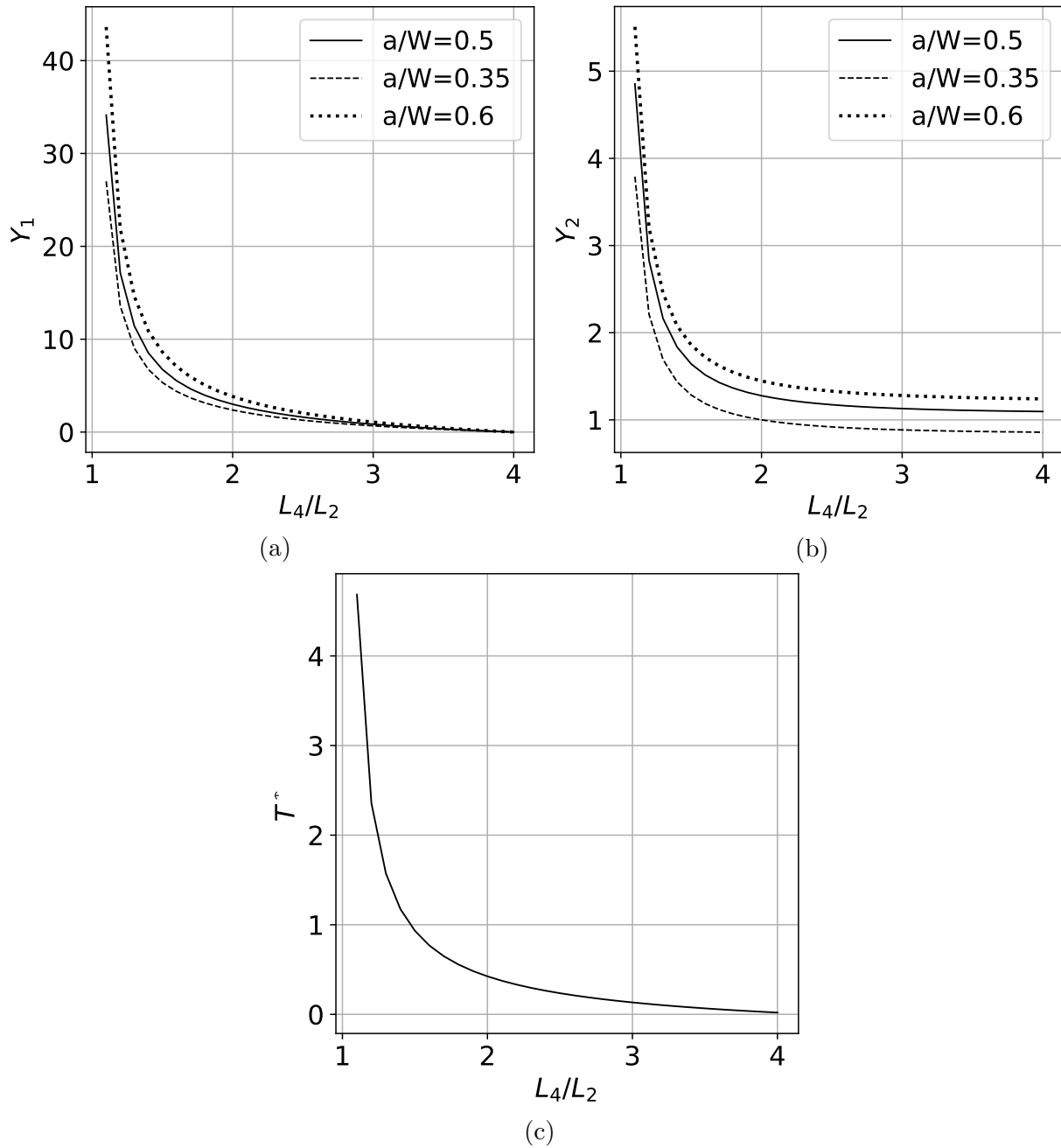Figure 4.2: Variations of Y with roller distances and different crack lengths. L_1=20 mm, L_2=5 mm, L_3=5 mm while L_4 varies. Fig (a) for Y_1 and (b) for Y_2. Fig (c) shows the T-stress for $a/W = 0.5$.
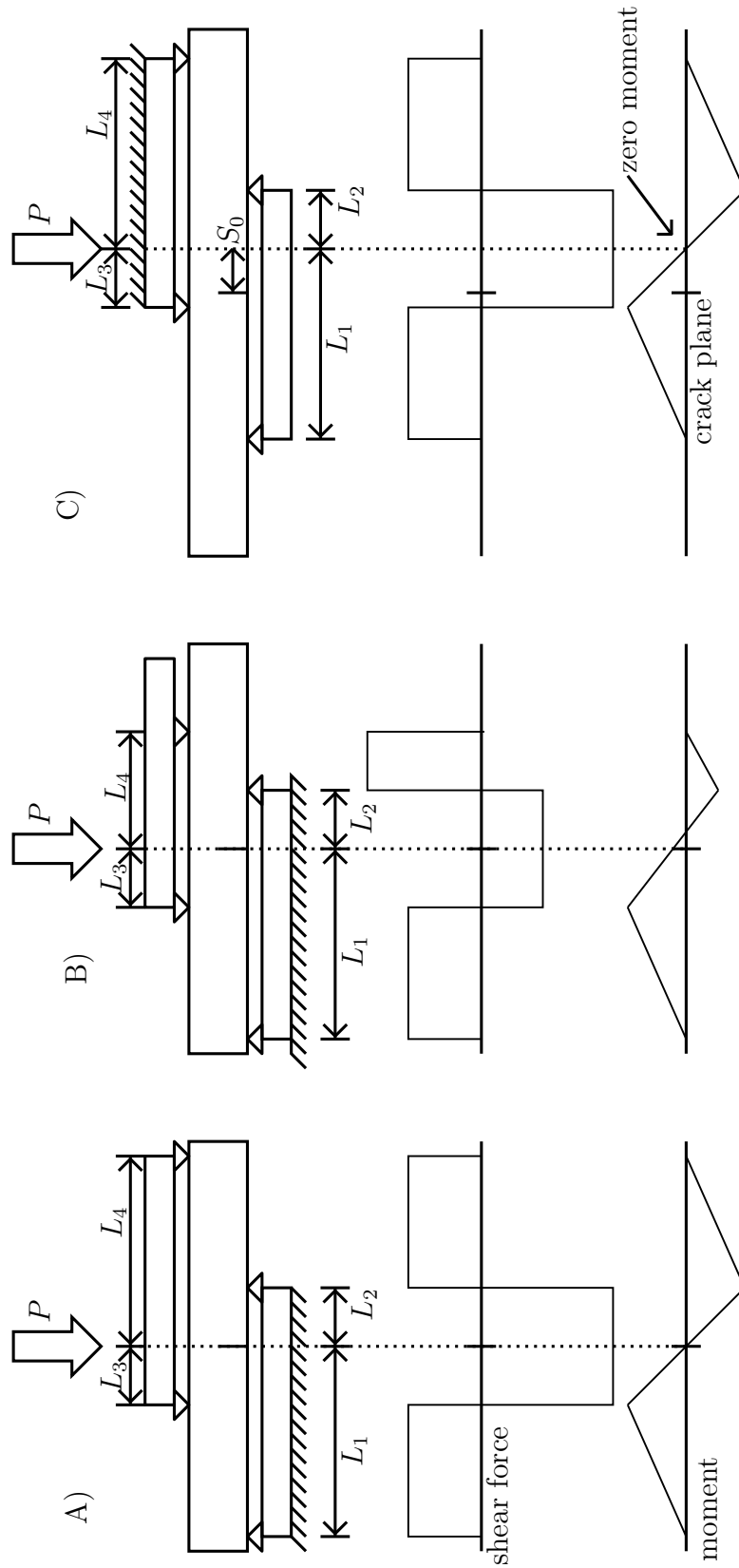
Figure 4.3: Test configuration for A) antisymmetric four point bending, B) asymmetric bending by roller distance variation, and C) asymmetric bending by loading point displacement.

4.2   Asymmtric mixed mode loading by loading point variation.

In this thesis, material data from two papers are valuated by the ASED criterion. Four specimen with different dimensions are simulated in a asymmetric four point bending test. The asymmetric test configuration used in the studied papers have constant roller width, but the distance from the crack to point of loading is varied, see figure 4.3(c). This configuration gives constant K_{II} for constant applied load since the shear forces are constant.

Though not explicitly stated in the papers, it is assumed that values with only slight variation in mode mixity M_e are tested with the same values of S_0, see figure 4.3. The values of S_0 is found by running FE-analyses of all four specimen types with varying values of S_0 and then compare the resulting mode mixity to the results from the papers. The plots used to make sets of similar mode mixity is seen in Appendix C. Strain energy density of the control volume is then used to make the load prediction curves seen in section 5.

The material properties are taken from the respective papers if not explicitly stated otherwise. The test configuration and material data can be seen in table 4.3 and table **??**, respectively. The Poisson's ratio for the short and long alumina samples are assumed 0.23 for similarity between the papers, but would be dependent on production method.

The fracture curves for the specimens used by Suresh et al. can be written

$$\frac{K_{\text{I,c}}}{K_{\text{eff}}} = \sqrt{\frac{1}{(\frac{6S}{W}F_I)^2 + F_{II}^2}\left[\left(\frac{6S}{W}F_I\right)^2 + \left(\frac{2\kappa + 3}{2\kappa - 1}\right)F_{II}^2\right]} \tag{4.6}$$

for ASED, and

$$\frac{K_{\text{eff}}}{K_{\text{I,c}}} = \frac{\sqrt{(\frac{6S}{W}F_I)^2 + F_{II}^2}}{\frac{6S}{W}F_I \cos^3\frac{\theta_0}{2} - \frac{3}{2}F_{II}\sin 2\theta_0 \cos\frac{\theta_0}{2} + \sqrt{2r_c/a}\frac{T^*}{B}} \tag{4.7}$$

for GMTS. F_I and F_{II} is the shape factors which are dependent on a/W. By not including the terms containing the normalized T-stress, the GMTS criterion is the MTS criterion.

Table 4.3: The values of S_0 and M_e to specimen from Li et al and Suresh et al.

Glass		Alumina		Alumina long		Alumina short	
S_0	M_e	S_0	M_e	S_0	M_e	S_0	M_e
0.0	0.0	0.0	0.0	0.0	0.0	0.0	0.0
0.15	0.15	0.15	0.19	0.78	0.31	0.25	0.10
0.28	0.27	0.30	0.34	1.6	0.51	0.65	0.25
0.57	0.47	0.50	0.50	2.6	0.66	1.3	0.44
1.2	0.69	0.85	0.66			2.0	0.57
2.2	0.82	2.0	0.84			2.4	0.63
						2.6	0.65
						3.0	0.69

The equations for Li et al. is similar, but slightly different:

$$\frac{K_{\text{I,c}}}{K_{\text{eff}}} = \sqrt{\frac{1}{(\frac{S}{W}F_I)^2 + F_{II}^2}\left[\left(\frac{S}{W}F_I\right)^2 + \left(\frac{2\kappa+3}{2\kappa-1}\right)F_{II}^2\right]} \tag{4.8}$$

for ASED, and

$$\frac{K_{\text{eff}}}{K_{\text{I,c}}} = \frac{\sqrt{(\frac{S}{W}F_I)^2 + F_{II}^2}}{\frac{S}{W}F_I\cos^3\frac{\theta_0}{2} - \frac{3}{2}F_{II}\sin 2\theta_0\cos\frac{\theta_0}{2} + \sqrt{2\pi r_c W}T^*} \tag{4.9}$$

for GMTS. The shape functions included by Suresh et al. and Li et al. are slightly different and therefore the fracture criterions are represented here slightly different as well. The values for F_I and F_{II} can be found in the papers by Suresh et al. [7] and Li et al. [6].

4.3 Finite element analysis method

4.3.1 Model

The models are created in Abaqus 6.14-1. It is a 2D-planar deformable model with dimensions of width and length of the specimen, W and L_{tot} respectively. Plane strain thickness is set to the thickness B. The model is sectioned in such a way that cracks can be made with the special feature "Crack".

A seam is assigned on the geometry of the model and a crack front is applied to the tip of the crack. This feature makes coincident nodes that are not connected transverse the seam. The crack type contour integral is chosen, meaning that the stress intensity factors are calculated by use of J-integral. The crack front is the geometry point at the end of the crack tip. The crack extension direction is chosen with the q-vector=(x,y,z)=(0,1,0). For second-order Mesh Options is chosen $t = 0.25$ and Degenerate element control is option "Collapsed element side, single node". These options are chosen to create a $1/\sqrt{r}$ singularity for linear elastic fracture mechanics. Other options can be chosen for power-hardening law material or for plasticity.

The results are requested through history output and field output. Values for the stress intensity factors K_I and K_{II} is requested in the domain of the crack. A number of 10 contours is requested to make sure the integral contains the stress fields necessary for computation. Similarly, a history output request for T-stress is made. The mixed mode stress intensity factors are calculated through an interaction integral which allows the calculation of separate stress intensity values when in mixed mode loading. T-stress is also calculated through the same interaction integral. Figure 4.6a shows the basic model while figure 4.6b shows the resulting deformation after applied load.

4.3.2 Mesh

The model is sectioned so different types of mesh control can be applied to different regions. Figure 4.5a shows how the model is sectioned. Sweep elements with bias is used on the sections near the crack tip since it ensures a higher number of elements near the crack tip which is necessary for accurate contour integral calculations since they are dependent on strain values [?].
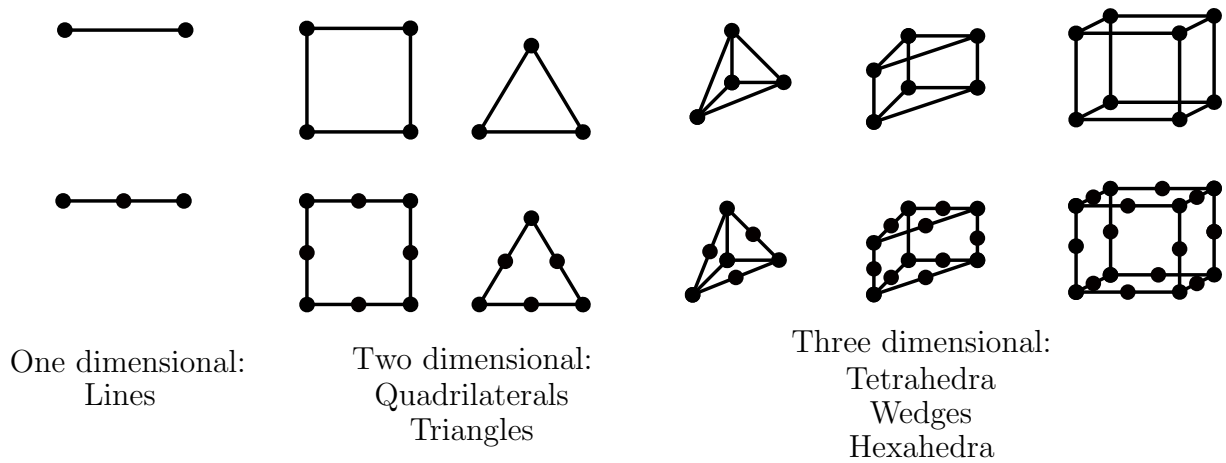
One dimensional: Two dimensional: Three dimensional:
Lines   Quadrilaterals   Tetrahedra
                          Triangles   Wedges
                                                              Hexahedra

Figure 4.4: The different 1D, 2D and 3D element types and the higher geometric order equivalent.

Quadrilaterial elements, see figure 4.4, is chosen since triangular elements are not suited for bending. Additionally, quadratic approximation is chosen for all elements higher accuracy. Plane strain elements and reduced integration is also chosen, meaning CPE8R-elements in Abaqus. Edges, especially cracks as in this model, leads to singularities with possible large errors. Combining both element refinement and higher order approximation (quadratic geometric order) allows optimal small error. Doing so does lead to increased computing times.

In figure 4.5b the control volume where the strain energy density is extracted is seen in addition to bias of the element seeding to refine the mesh around the crack tip. The refinement is necessary for the calculation of accurate stress intensity factor.

A quick K_I convergence test was performed and shown to give stable results from 3 elements or more on the inner circle, see table 4.4. Between 10-15 elements were chosen for the inner circle to ensure convergence even when the control volume is changed during simulation.

Table 4.4: The number of elements and corresponding stress intensity factor values.

Nr. of elements on inner circle	1	2	3	5	10	15	30
K_I (MPa$\sqrt{\text{mm}}$)	2.334	2.345	2.346	2.346	2.346	2.46	2.346

Quad shape structured element

Quad-dominated sweep element
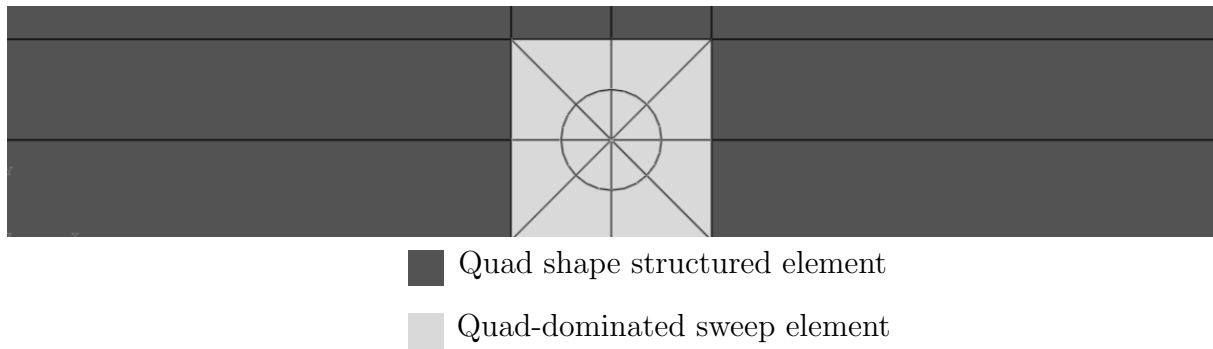
(a)
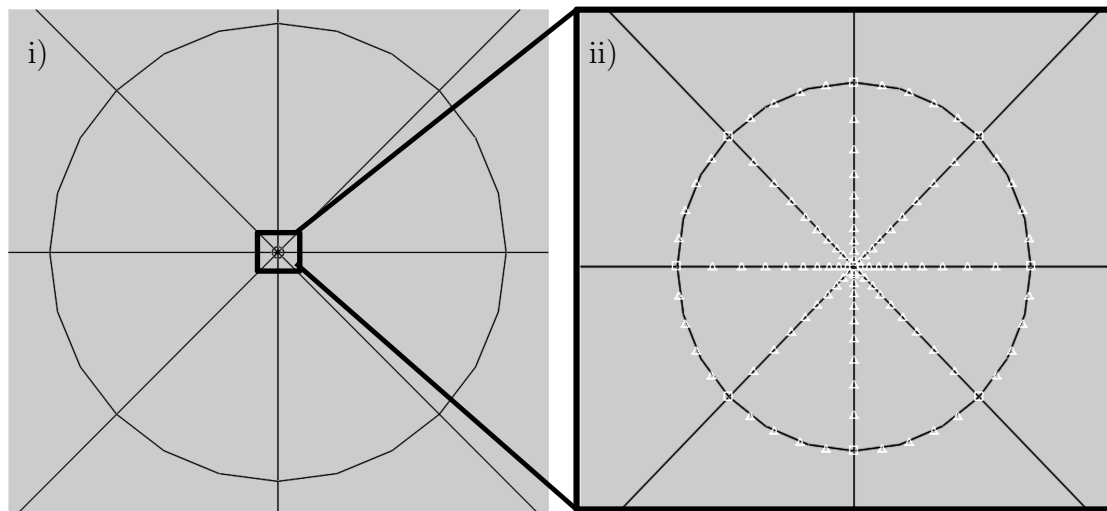
(b)

Figure 4.5: a) Figure shows how the part is sectioned and what element control is used. b) Figure i) shows the two circles that enwrap the crack tip. ii) shows an enlarged section of the red square in i) and shows how bias change the element structure near the crack tip. A bias ratio of 5 and 10 elements is shown on the highlighted lines.

4.3.3 Script description

A script is used to change variables, apply loads, set boundary conditions and change the radius of R_0 and run simulations. When changing the roller distance from the crack tip a single parameter, L_i, is changed and the force applied to the model at each point is recalculated for each simulation distance. When changing the load point distance from the crack S_0, all L_i are changed, but applied load is constant. The strain energy in the elements (ELSE) and element volume (EVOL) of the control area is extracted and used for calculating fracture loads P_{th} seen in section 5. The applied loads can be written

$$P_1 = P \left(1 - \frac{L_3}{L_3 + L_4} \right) \tag{4.10a}$$

$$P_2 = P \frac{L_3}{L_3 + L_4} \tag{4.10b}$$

Force points

(a)

(b)
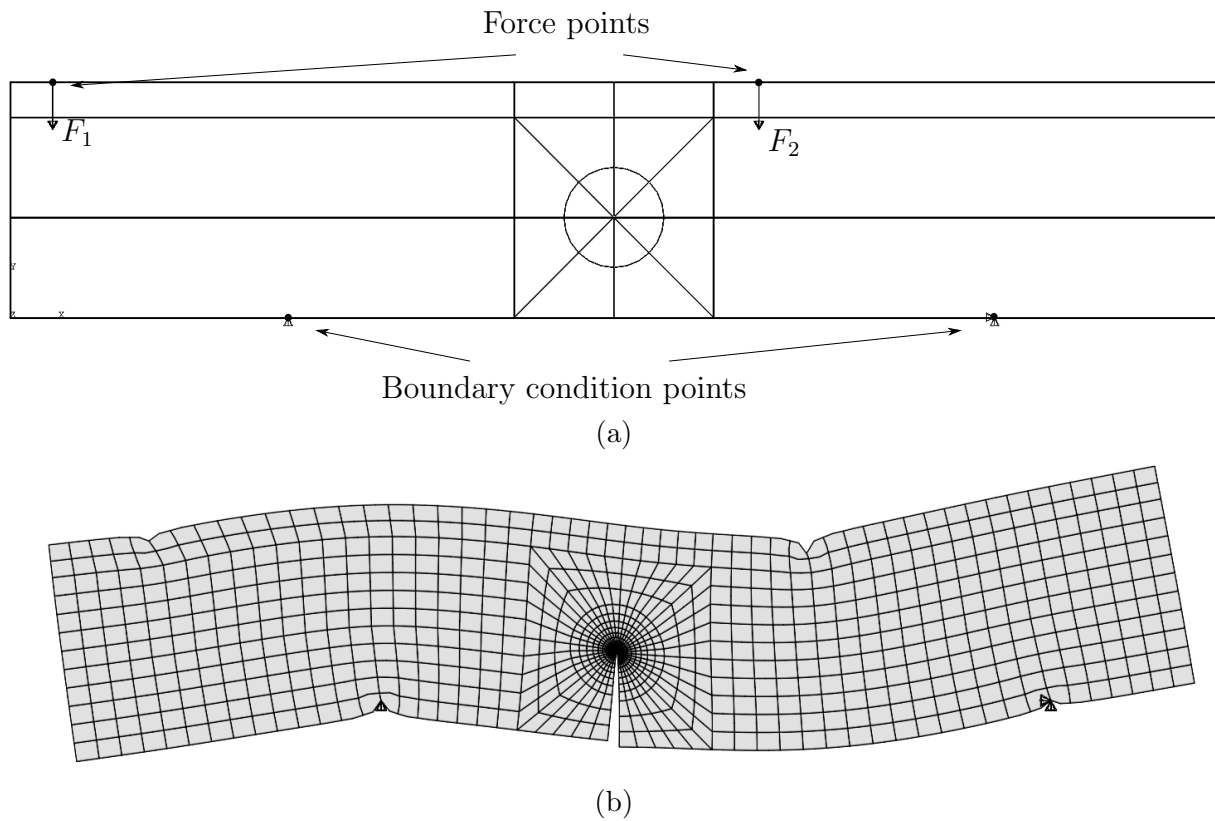
Figure 4.6: (a) The construction of the FE-model showing points that represent the rollers in the test configuration. Points for boundary conditions and applied loads are highlighted. (b) A unit load $P = 1N$ is applied. Deformations shown in the figure is scaled to demostrate the deformation of an asymmetric four point bending test.

where P_1 and P_2 is defined in figure 4.6a, P is the applied load by the testing machine and L_i is the roller distances.

The two scripts used for roller distance variation and loading point distance variation can be found in full in appendix B and C.

Chapter 5

Results and discussion

5.1 Simulation of yttria stablized zirconia specimen

The geometric parameters Y_1 and Y_2 had noticeable change between the limits of the a/W-ratio and there is an asymptote as $L_4 \to L_2$. The range $1.5 < L4/L2 < 4$ is proposed as a limit as to what mode mixity range the ASFPB configuration allows for the specimen of this size, see figure 5.1. The Y_1-value for $a/W = 0.6$ is about 60% larger than the Y_1-value for $a/W = 0.35$ at $L_4/L_2 = 1.5$, and the difference of 0.5 mm from $L_4 = 7.5$ to $L_4 = 8.0$ mm for $a/W = 0.5$ gives a Y_1 reduction of 18%. The difference is larger still for ratios $L_4/L_2 < 1.5$. Since the dimensions of the test specimen already are relatively small, the geometry of the crack needs to accurately measured and the testing needs to be performed by a skilled testing operator. For larger specimen a larger range can be valid since the same mismeasurement (e.g. 0.5 mm), will not give as large an error.

Figure 5.2 shows the predicted fracture load curves for the yttria stabilized zirconia specimens. By testing, one would see if the predicted loads would correspond with the experimental results. The $K_{\mathrm{I,c}}$ fracture toughness for 8YSZ is lower than both 3YSZ and 5YSZ and the fracture load curves produced by the ASED criterion describe this behaviour. The fracture loads are within the limitations of the testing machine (< 5000 N).

Neither Y_i or T^* were changed by varying elastic material properties, as was expected.

The different criterion predict failure at somewhat similar trend above $M_e = 0.5$, see figure 5.3 which show the fracture curves for 3YSZ. The fracture curves are practically identical for 5YSZ and 8YSZ, see appendix D. It is at lower mode mixities, where K_{II} dominates, that there is noticeable difference between the ASED criterion and the two stress based criterion. For the would be tested specimen of YSZ, the critical crack initiation angle would be measured and compared to a corresponding figure that is presented in figure 5.4 to see if the contribution of T-stress can be accurately measured. As seen from figure 5.4, the critical angle is most sensitive for higher M_e while the fracture prediction curve (figure 5.3) is most sensitive to T-stress in the region of $0.3 < M_e < 0.6$.

There has been reported higher mixed mode fracture resistance for testing of ceramics with the brazillian disc (BD) test configuration, mostly attributed to having relatively high negative T-stresses and a large critical distance R_c [44]. For the ASFPB specimen, the T-stresses are positive and the magnitude decrease as mode mixity decrease, thus the prediction is that the additional stress will not affect the mode II fracture toughness. It will however reduce the stress intensity factors for mixed mode loading, increasing fracture resistance. This could explain that the fracture load for 3YSZ, 5YSZ and 8YSZ has a
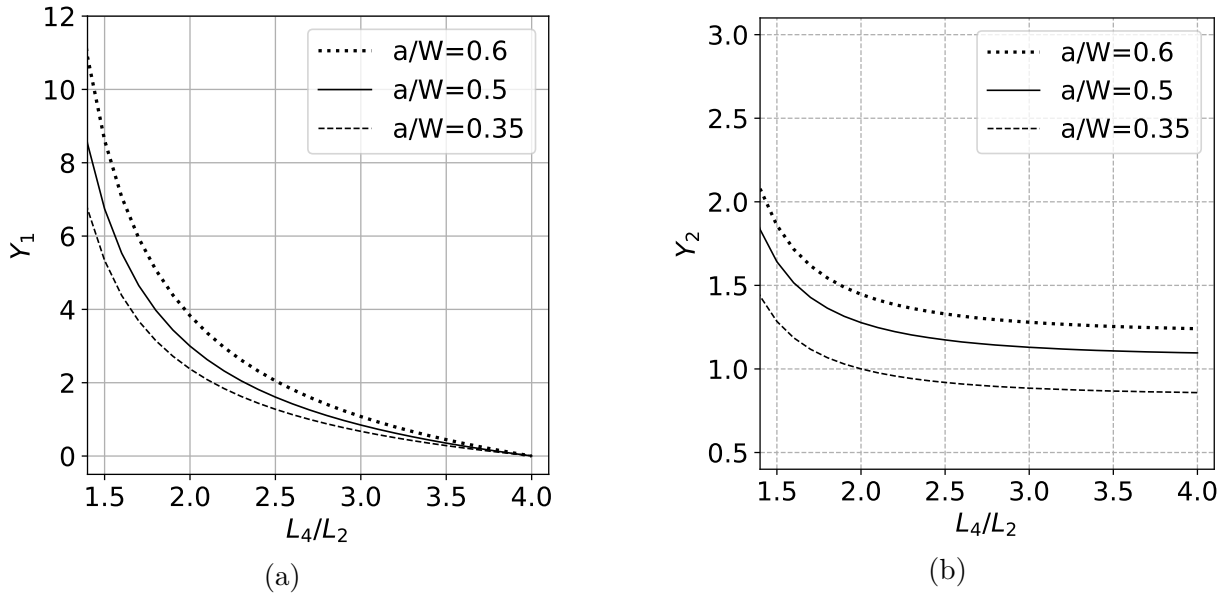
Figure 5.1: The values for Y_1 and Y_2 for suggested range for roller distances L_4/L_2

maximum value at $M_e = 0.2$. It is worth noting that the suggested roller distance values correspons with results that imply that L_4/W should be larger than 1 for pure mode II fracture toughness to be accurately measured without being influenced by T-stress [50].

Both studied papers (Li et al. and Suresh et al.) have a span of 2-3 mm to achieve different loading configuration even when specimen is smaller in size. Margevicius et al. [51] states they have a hard time accurately setting the distance S_0 even with fine threaded adjustment for the same configuration. The long alumina specimen prepared by Suresh et al. are twice as long as the YSZ-specimen and still have only a third of the span. Having a larger span decrease the required skill of the testing operator as inaccuracies will not change mode mixity as much. The volume of specimen (3x4x45 mm) is also 86% of the size of the smallest BD specimen tested by Ayatollahi et al. [44], which is beneficial forexpensive materials.

Figure 5.2: Fracture load curve for the testing of yttria stabilized zirconia specimen.

Figure 5.3: The fracture curves from the MTS, GMTS and ASED criterion.

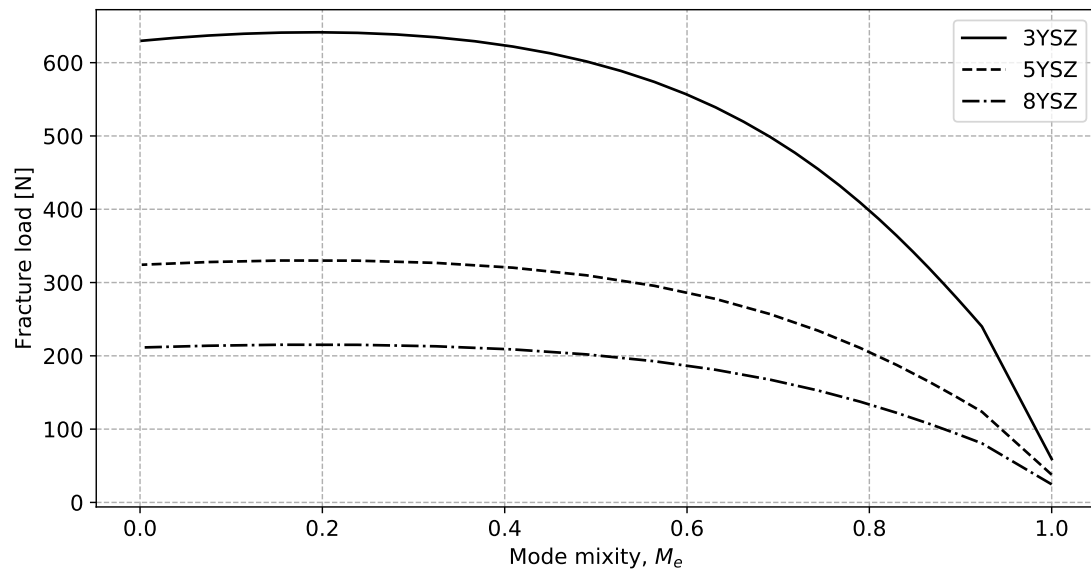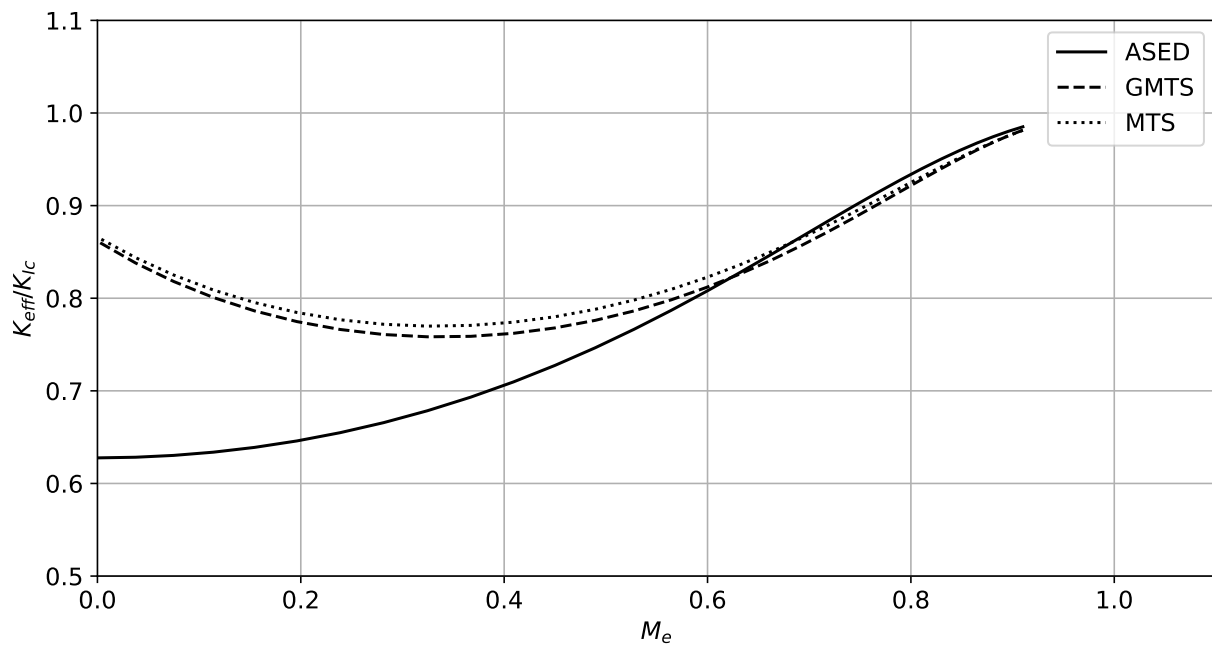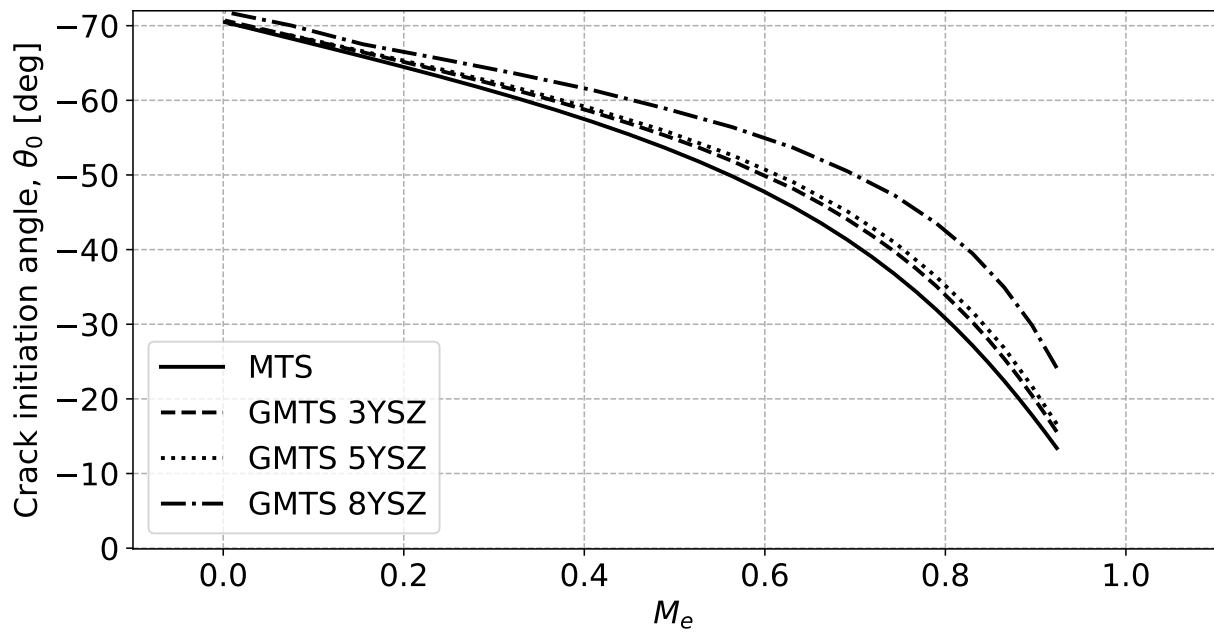Figure 5.4: The expected crack angle initiation for 3YSZ, 5YSZ and 8YSZ composites by MTS and GMTS criterion.

5.2 Analysis of earlier experimental results

The test data acquired have some data points that contradict expected behaviour. The alumina samples tested by Li et al. show fracture loads in same range of 600-800 N, but with mode mixity values of 0.34 and 0.50, see figure 5.5. It is expected that fracture loads increase when M_e decrease, which is opposite of observed behaviour. Li et al. tested course grained alumina samples to test the grain interlocking/bridging by the two crack faces. The glass specimen Li et al. prepared was intended as a control group with little to no grain interlocking. If grain interlocking was present, the fracture resistance would increase and fracture load would be underestimated, not overestimated. The overestimation at $M_e = 0.34$ for the alumina specimen could indicate that grain interlocking was not present. The scatter shown for pure mode II fracture toughness for the alumina samples are larger than the ones for the glass samples, see figure 5.7, which could indicate that grain interlocking were present for some of the samples at $M_e = 0$. For $M_e = 0$, $K_{\text{eff}}/K_{\text{I,c}} = K_{\text{II,c}}/K_{\text{I,c}}$. The ratio $K_{\text{II,c}}/K_{\text{I,c}}$ for the tested specimen varies from 0.57 to 0.98. Pure mode II fracture toughness has not been adapted as the material property the same way pure mode I fracture toughness has. It is likely a material property as well as dependent on geometry and loading configuration. It is worth noting that Razavi et al. [5] show generally accurate estimates of fracture load of a grainte rock, the largest discrepancy was 10.24% and was in the case of pure mode II fracture load for an asymmetric four point bending test.

The fracture load curves for Suresh et al. (figure 5.6) show an underestimation of the fracture load. The samples, both long and short show the same trend, meaning that the fracture resistance is larger than anticipated. A positive T-stress decrease the fracture resistance, as seen in figure 5.8 and thus the results oppose each other. The positive T-stress contribution could however explain the overestimation of fracture load at $M_e = 0.34$ for the alumina specimen prepared by Li et al. The GMTS curve for alumina samples from Li et al. show large reduction in fracture resistance in the region $0.2 < M$ and predicts the results better than the MTS criterion. T-stress practically vanish for pure mode II fracture toughness for all four specimen. The increased fracture toughness of mode II loading is suggested much more dependent on geometry compared to mode I loading since the crack walls can interact. For mixed mode loading, with a considerable amount of pure mode I loading still present, the crack would open and keep the walls from interacting. The effect of T-stress is much more prominent for the samples from Li et al. which is suspected could be because of the smaller specimen size.

The biaxility ratio is shown in figure 5.10. It shows how large a portion the T-stress compared to K_{eff}. Compared to Brazillian disc specimen and semi-circular bending (SCB) specimen the biaxility is low; beneath 0.2 for all four specimen. For comparison, BD have been shown to have about -4 at $M_e = 1$ and -1 at $M_e = 0$. There is considerable larger effect for T-stress for the BD specimen as can noted by their results; the GMTS criterion is much more successfull in predicting failure compared to MTS criterion [44] for BD specimen. The biaxility ratio for the simulated 3YSZ specimen is also included. It shows how T-stress is relatively large for $M_e > 0.8$.

As demonstrated by previous works [25] grain size is an important material property when discussing fracture mechanics, specifically testing fracture toughness. The notch radius should be smaller than the smallest microstructural feature size, which often is the grain size. Doing so reduce the influence of the size effect when testing for fracture parameters.

It is not immediately clear which criterion best describes the mixed mode fracture behaviour. Figure 5.9 shows the absolute average error of the experimental data compared to the predictions of the ASED, GMTS and MTS criterion. MTS is worse for the alumina samples prepared by Li et al. for $M_e < 0.6$ and similar above. If the decreased fracture resistance were because of T-stress and not statistical error, then GMTS and ASED describe this behaviour better.

The ASED criterion comes worse off compared to the stress based ones for the alumina samples prepared by Suresh et al. for pure mode II loading. A reason for this could be that the samples have a notch rip radius of 70 µm and will also strongly affect the measured fracture toughness as shown in section 2.2 and figure 2.6. When such large notch radii is used, perhaps the specimen modelled with a rounded notch and notch-stress intensity factors would be better suited, Lazzarin and Filippi have had success for pure mode I fracture toughness [52]. Additionally, the grain size average is 3µm for alumina from Surehs et al. and 12.5µm from Li et al., so different fracture behaviour is expected.

The alumina samples prepared by Suresh et al. have an opening angle $2\alpha = 60°$. This angle is not considered in the FE-model and could have bearing on the results bearing on the results.

All three criteria predict the glass fracture behaviour very well with all points below 20% absolute average error.
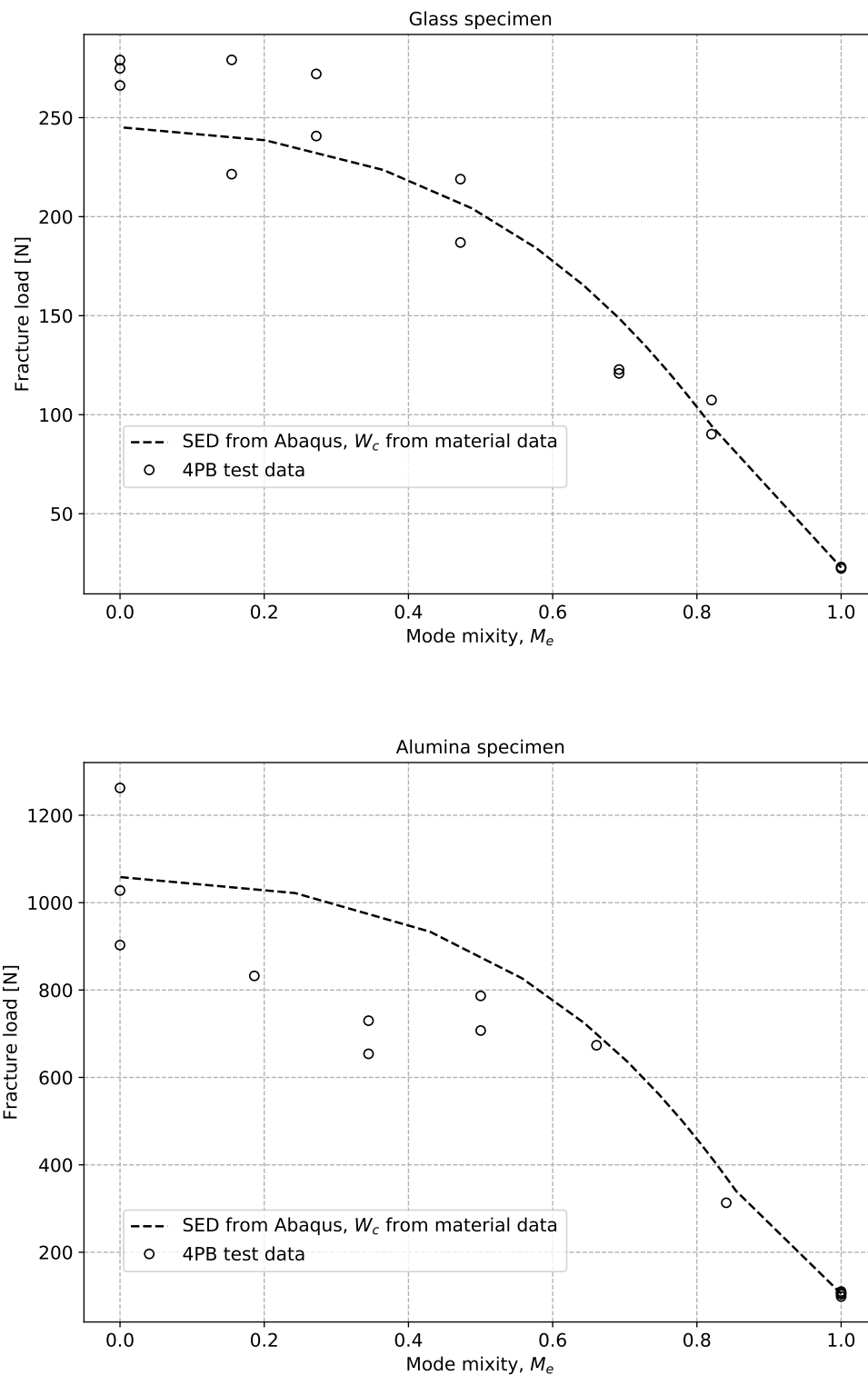
Figure 5.5: Fracture load prediction curves for Li et al. by use of ASED criterion.
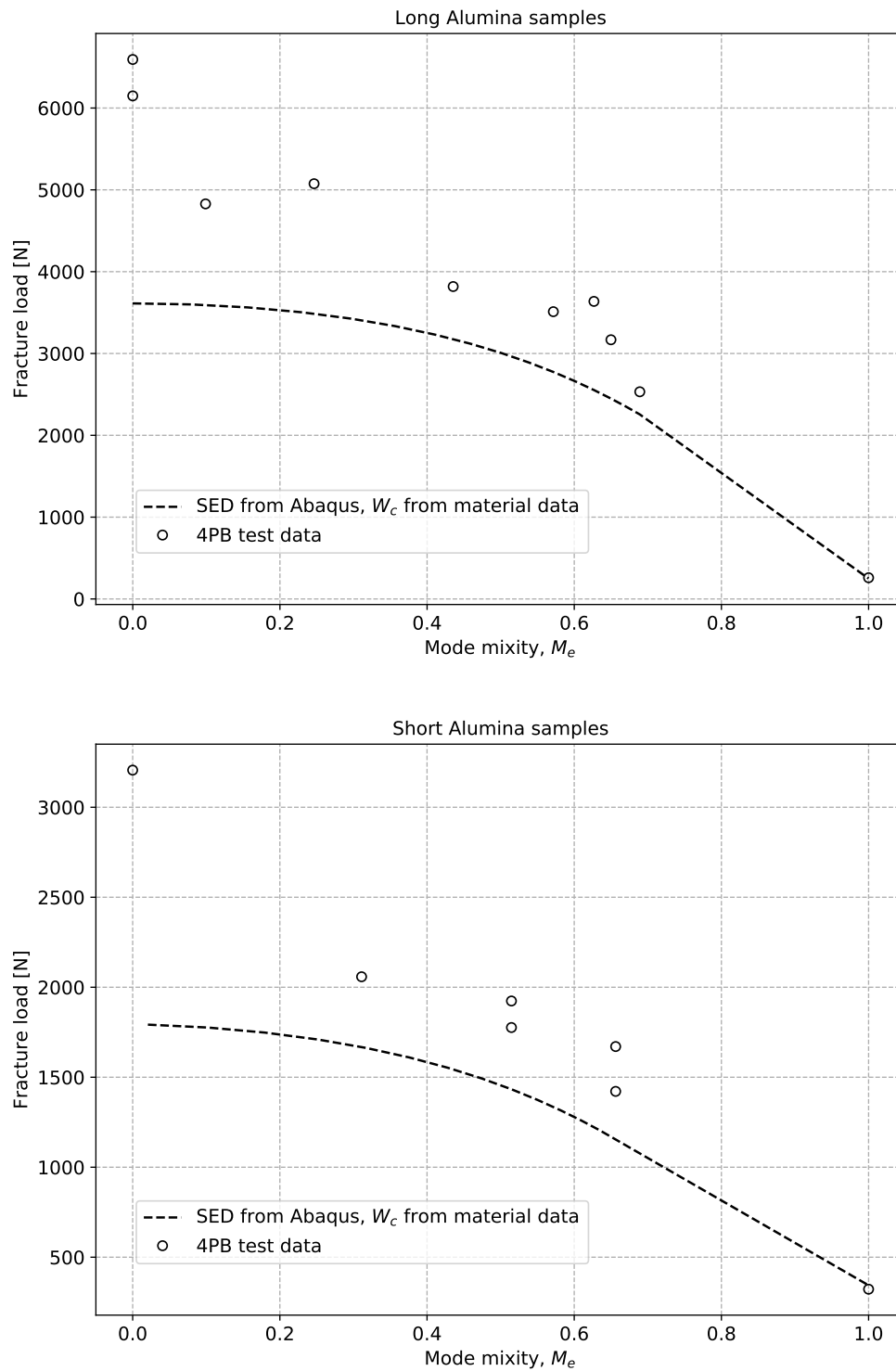
Figure 5.6: Fracture load prediction curves for the data points from Suresh et al. by use of ASED criterion.
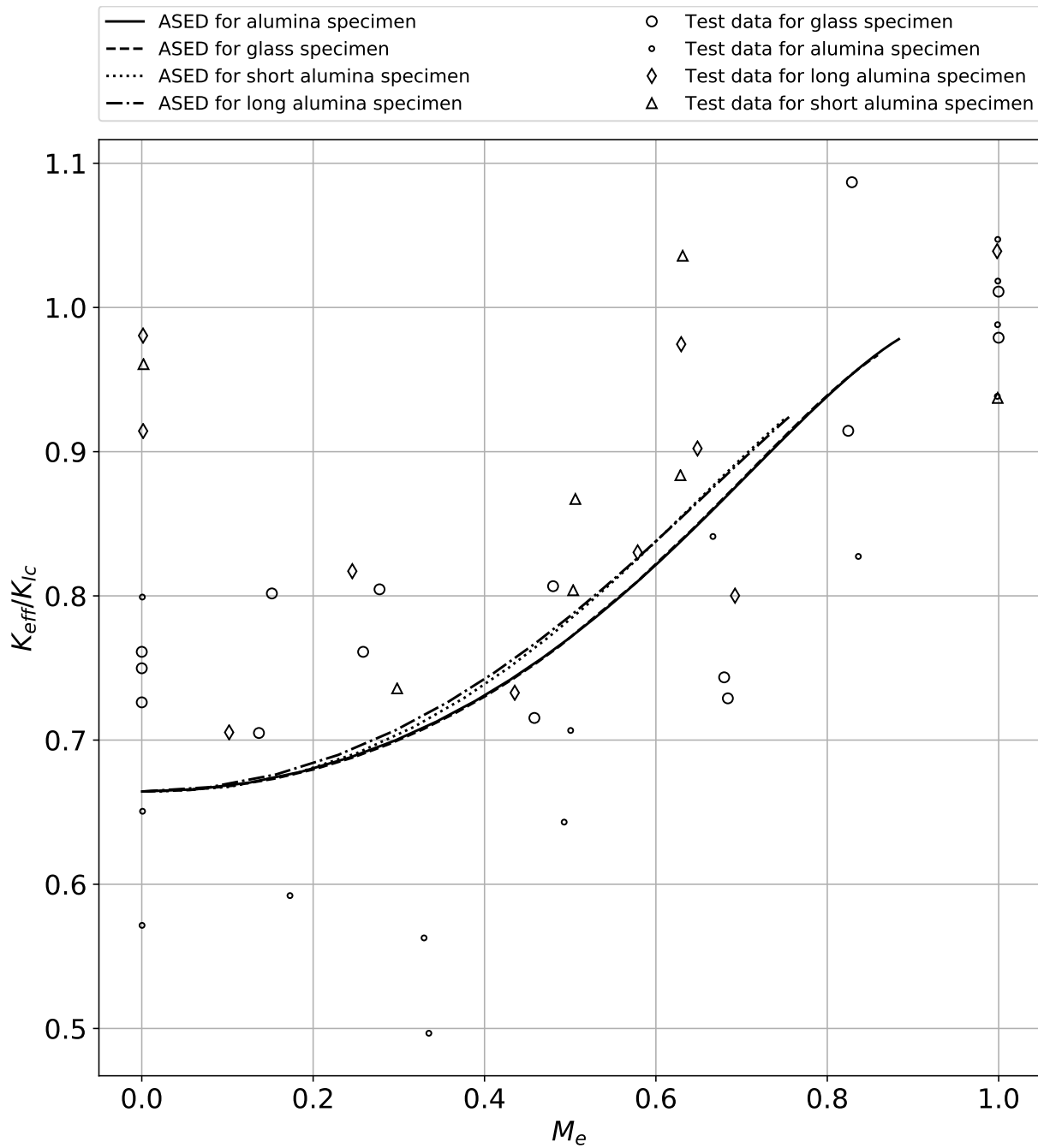
Figure 5.7: ASED prediction curves for the data points from Li et al. and Suresh et al.
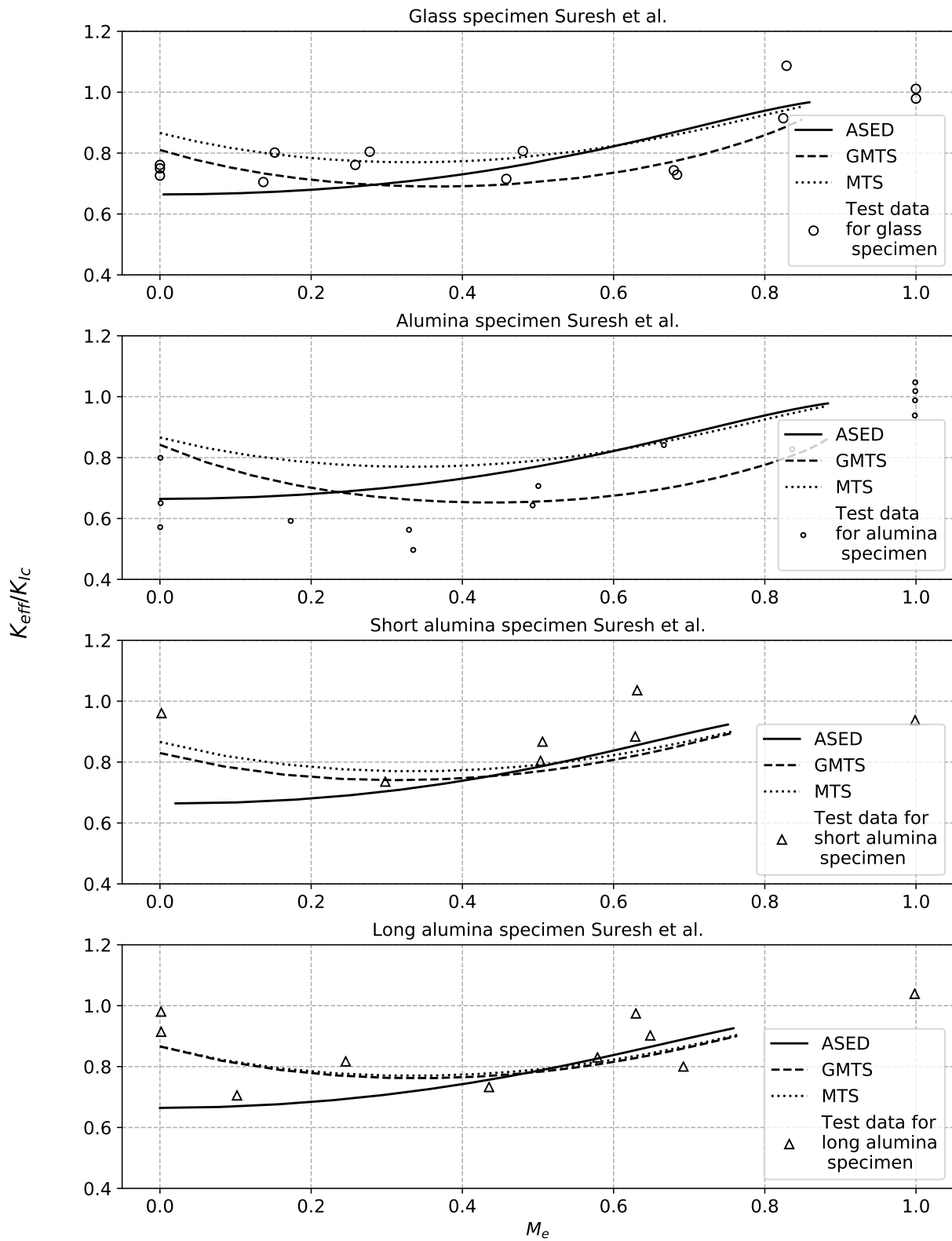
Figure 5.8: ASED, GMTS and MTS prediction curves for each specimen.
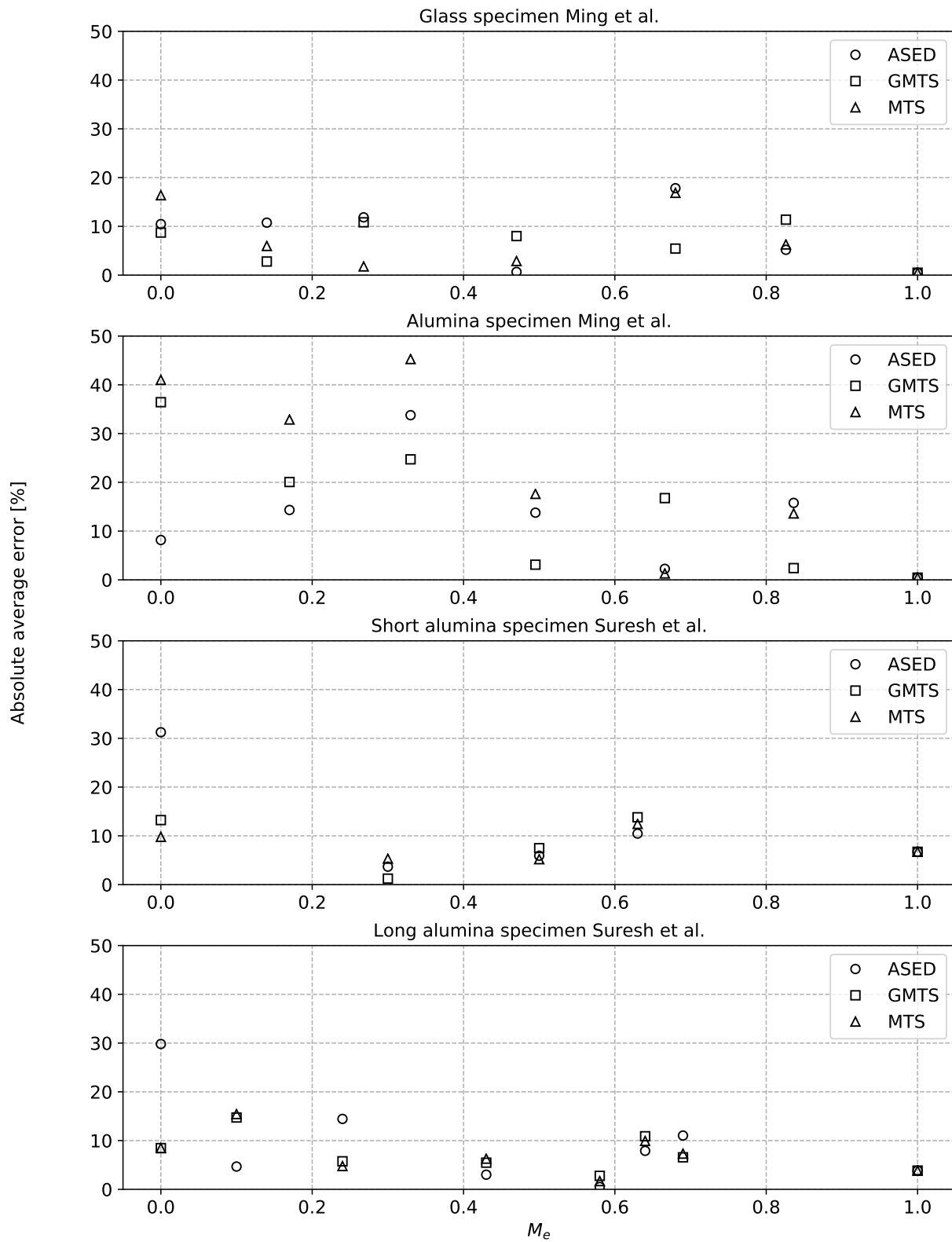
Figure 5.9: The data points show the absolute average error for the three fracture criterion.
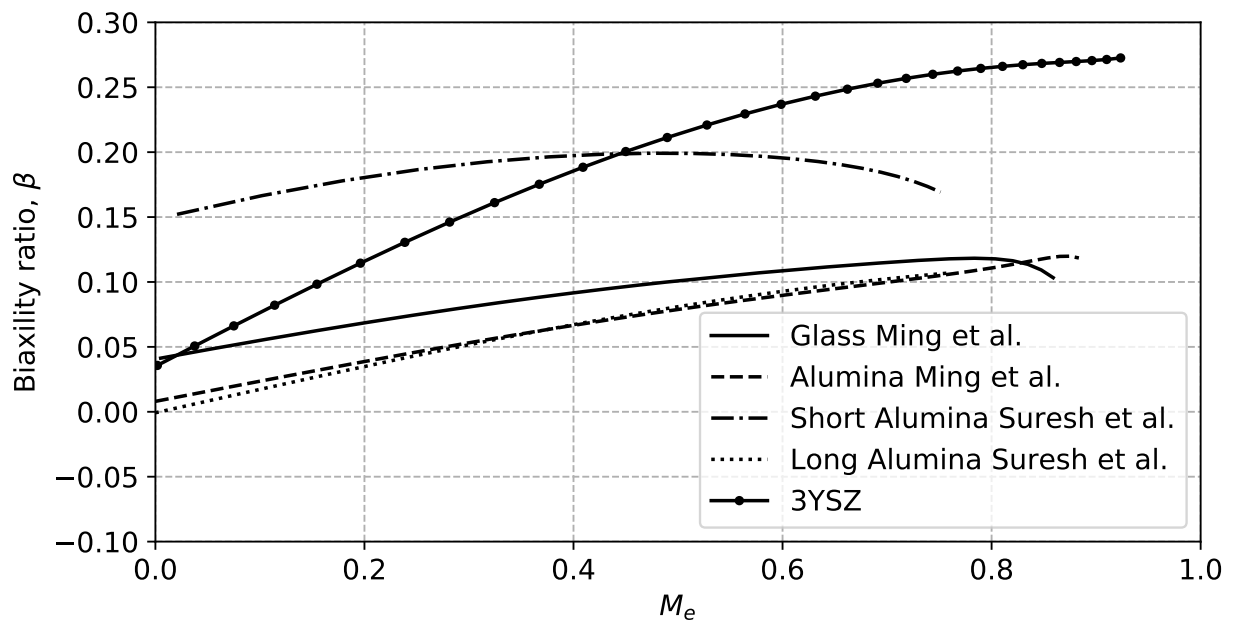
Figure 5.10: Biaxility ratio for the specimen from Li et al. and Suresh et al. The ratio is calculated from simulation results.

5.3   Conclusion

There is benefit in using the roller distance variation testing configuration that was prepared in this thesis compared to the loading point variation since it allows for larger distance between two loading points. Having both small test specimen and relatively large span for testing parameters, the roller distance variation testing is well suited for expensive materials.

All three criteria predict the results fairly well. Except for the alumina specimen from Li et al., all criteria typically have error less than 30%. The ASED criterion has the benefit of easily including variations of the crack tip opening angle especially for use in FE software such as Abaqus and use of notch-stress intensity factors for analytic solutions as well. GMTS and MTS have the benefit of being able to calculate the critical crack initiation angle which is useful when able to physically measure the tested specimen.

5.4   Further work

As a consequence of the delayed delivery of the test specimen, the experimental testing needs to be performed.

Because of the high operating temperature of solid-oxide fuel cells, fracture of electrolyte ceramics should also be tested in heightened temperature as it likely will affect the mechanical properties used for predicting fracture. Specifically elastic modulus and ultimate tensile stress, which decide the critical SED, is known to change with varying temperature [16] [53].

For the experimental data studied here, there correlation between prediction and experiments is not impressive. Moghaddam et al. [45] proposed a generalized ASED criterion which include the T-stress in similar fashion as GMTS. The results for BD and semi-circular bend (SCB) specimen using a generalized ASED criteria better fits the test results compared to ASED which over and underestimate the results. However, BD and SCB specimen have large T-stress and the paper suggest that the large difference between the predicted failure is because of the T-stress as previously discussed. For the four point bending specimen tested here, the effect of T-stresses have been shown small when using GMTS criterion and the low effect could be similar for generalized ASED.

The crack wall interaction for pure mode II is interesting topic for study. As stated earlier, the notch width does not affect the measured $K_{I,c}$ value as long as the not tip radius is small enough. Using a femtosecond laser to machine the notch tip would allow relatively large notch width and small crack tip. It could be interesting to see how dependant the mode II fracture toughness is on notch width and if grain interlocking can be validated.

Bibliography

[1] Marge Ryan. Fuel cells and hydrogen in norway. Report, Fuel Cell Today, 2013.

[2] Statistics Norway (SSB). Nedgang i klimagassutslippene, 2017.

[3] T. L. Anderson. *Fracture mechanics : fundamentals and applications.* Taylor & Francis, Boca Raton, Fla, 3rd ed. edition, 2005.

[4] F. Berto and P. Lazzarin. Recent developments in brittle and quasi-brittle failure assessment of engineering materials by means of local approaches. *Materials Science and Engineering: R: Reports*, 75:1–48, 2014.

[5] S. M. J. Razavi, M. R. M. Aliha, and F. Berto. Application of an average strain energy density criterion to obtain the mixed mode fracture load of granite rock tested with the cracked asymmetric four-point bend specimens. *Theoretical and Applied Fracture Mechanics*, 2017.

[6] Ming Li and Mototsugu Sakai. Mixed-mode fracture of ceramics in asymmetric four-point bending: Effect of crack-face grain interlocking/bridging. *Journal of the American Ceramic Society*, 79(10):2718–2726, 1996.

[7] S. Suresh, C. F. Shih, A. Morrone, and N. P. O'Dowd. Mixed-mode fracture toughness of ceramic materials. *Journal of the American Ceramic Society*, 73(5):1257–1267, 1990.

[8] Omar Z. Sharaf and Mehmet F. Orhan. An overview of fuel cell technology: Fundamentals and applications. *Renewable and Sustainable Energy Reviews*, 32:810–853, 2014.

[9] Univesity of Cambridge. Fuel cells, 2006.

[10] Arata Nakajo, Zacharie Wuillemin, Jan Van herle, and Daniel Favrat. Simulation of thermal stresses in anode-supported solid oxide fuel cell stacks. part i: Probability of failure of the cells. *Journal of Power Sources*, 193(1):203–215, 2009.

[11] Arata Nakajo, Zacharie Wuillemin, Jan Van herle, and Daniel Favrat. Simulation of thermal stresses in anode-supported solid oxide fuel cell stacks. part ii: Loss of gas-tightness, electrical contact and thermal buckling. *Journal of Power Sources*, 193(1):216–226, 2009.

[12] T. Zhang, Q. Zou, J. Zhang, D. Tang, and H. Yang. Development of ceramic sealant for solid oxide fuel cell application: Self-healing property, mechanical stability and thermal stability. *Journal of Power Sources*, 204:122–126, 2012.

[13] Z. G. Liu, J. H. Ouyang, Z. Ren, K. N. Sun, and Y. Zhou. Influence of fe2o3 addition on the densification and oxygen ion conductivity of the gdsmzr2o7 ceramic. *Journal of the European Ceramic Society*, 34(15):3735–3740, 2014.

[14] Ryan O'Hayre, Suk-Won Cha, Whitney G. Colella, and Fritz B. Prinz. Fuel cell fundamentals (3rd edition).

[15] M. Morales, J. J. Roa, X. G. Capdevila, M. Segarra, and S. Piñol. Mechanical properties at the nanometer scale of gdc and ysz used as electrolytes for solid oxide fuel cells. *Acta Materialia*, 58(7):2504–2509, 2010.

[16] P. Gao, A. Bolon, M. Taneja, Z. Xie, N. Orlovskaya, and M. Radovic. Thermal expansion and elastic moduli of electrolyte materials for high and intermediate temperature solid oxide fuel cell. *Solid State Ionics*, 300:1–9, 2017.

[17] J. Cao, X. Dong, Y. Dong, and X. Feng. Strengthening of gadolinia-doped ceria (ce¡inf¿0.80¡/inf¿gd¡inf¿0.20¡/inf¿o¡inf¿2-¡/inf¿) thick ceramic membranes with co-doping of 1 mol% cuo. *International Journal of Applied Ceramic Technology*, 12(5):1027–1033, 2015.

[18] P. C. C. Daza, R. A. M. Meneses, J. L. de Almeida Ferreira, J. A. Araujo, A. C. M. Rodrigues, and C. R. M. da Silva. Influence of microstructural characteristics on ionic conductivity of ceria based ceramic solid electrolytes. *Ceramics International*, 44(2):2138–2145, 2018.

[19] S. Ramesh, C. K. Ng, C. Y. Tan, W. H. Wong, C. Y. Ching, A. Muchtar, M. R. Somalu, S. Ramesh, H. Chandran, and P. Devaraj. Effects of sintering on the mechanical and ionic properties of ceria-doped scandia stabilized zirconia ceramic. *Ceramics International*, 2016.

[20] C. K. Ng, S. Ramesh, C. Y. Tan, A. Muchtar, and M. R. Somalu. Microwave sintering of ceria-doped scandia stabilized zirconia as electrolyte for solid oxide fuel cell. *International Journal of Hydrogen Energy*, 41(32):14184–14190, 2016.

[21] Miguel Morales, Joan Josep Roa, José Manuel Pérez-Falcón, Alberto Moure, Jesús Tartaj, and Mercè Segarra. Electrical and mechanical characterization by instrumented indentation technique of la0.85sr0.15ga0.8mg0.2o3 electrolyte for sofcs. *Journal of the European Ceramic Society*, 32(16):4287–4293, 2012.

[22] M. Morales, J. J. Roa, J. M. Perez-Falcón, A. Moure, J. Tartaj, F. Espiell, and M. Segarra. Correlation between electrical and mechanical properties in la 1-xsrxga1-ymgyo3- ceramics used as electrolytes for solid oxide fuel cells. *Journal of Power Sources*, 246:918–925, 2014.

[23] J. Xia, H. Nian, W. Liu, H. Xu, and D. Jiang. Synthesis, sintering behavior, structure, and electrical properties of 5ysz electrolyte. *Journal of Materials Engineering and Performance*, 24(9):3291–3299, 2015.

[24] M. Asadikiya, P. Foroughi, and Y. Zhong. Re-evaluation of the thermodynamic equilibria on the zirconia-rich side of the zro2-yo1.5 system. *Calphad: Computer Coupling of Phase Diagrams and Thermochemistry*, 61:264–274, 2018.

[25] H. Liu, W. Zhao, Y. Ji, J. Cui, Y. Chu, and P. Rao. Determination of fracture toughness of zirconia ceramics with different yttria concentrations by sevnb method. *Ceramics International*, 43(13):10572–10575, 2017.

[26] A. N. Kumar and B. F. Sørensen. Fracture resistance and stable crack-growth behavior of 8-mol%-yttria-stabilized zirconia. *Journal of the American Ceramic Society*, 83(5):1199–1206, 2000.

[27] A. Nakajo, J. Kuebler, A. Faes, U. F. Vogt, H. J. Schindler, L. K. Chiang, S. Modena, J. Van Herle, and T. Hocker. Compilation of mechanical properties for the structural analysis of solid oxide fuel cell stacks. constitutive materials of anode-supported cells. *Ceramics International*, 38(5):3907–3927, 2012.

[28] A. Masini, F. Šiška, O. Ševeček, Z. Chlup, and I. Dlouhý. Elastic properties of multi-layered ceramic systems for socs. *International Journal of Applied Ceramic Technology*, 2017.

[29] W. Zhao, P. Rao, and Z. Ling. A new method for the preparation of ultra-sharp v-notches to measure fracture toughness in ceramics. *Journal of the European Ceramic Society*, 34(15):4059–4062, 2014.

[30] S. Heiroth, R. Ghisleni, T. Lippert, J. Michler, and A. Wokaun. Optical and mechanical properties of amorphous and crystalline yttria-stabilized zirconia thin films prepared by pulsed laser deposition. *Acta Materialia*, 59(6):2330–2340, 2011.

[31] G. D. Quinn and R. C. Bradt. On the vickers indentation fracture toughness test. *Journal of the American Ceramic Society*, 90(3):673–680, 2007.

[32] Anzhe Wang, Ping Hu, Xinghong Zhang, Wenbo Han, Guiqing Chen, and Jiecai Han. Accurate measurement of fracture toughness in structural ceramics. *Journal of the European Ceramic Society*, 37(13):4207–4212, 2017.

[33] J. Chevalier, C. Olagnon, and G. Fantozzi. Subcritical crack propagation in 3y-tzp ceramics: Static and cyclic fatigue. *Journal of the American Ceramic Society*, 82(11):3129–3138, 1999.

[34] Carl T. Herakovich. *Mechanics of fibrous composites*. Wiley, New York, 1998.

[35] William D. Callister. *Materials science and engineering : an introduction*. Wiley, New York, 7th ed. edition, 2007.

[36] ML Williams. Stress singularities resulting from various boundary conditions in angular corners of plates in extension. *Journal of applied mechanics*, 19(4):526–528, 1952.

[37] M. L. Williams. On the stress distribution at the base of a stationary crack. *Journal of Applied Mechanics*, 24:109–114, 1957.

[38] D. J. Smith, M. R. Ayatollahi, and M. J. Pavier. The role of t-stress in brittle fracture for linear elastic materials under mixed-mode loading. *Fatigue and Fracture of Engineering Materials and Structures*, 24(2):137–150, 2001.

[39] Y. Chao and X. Zhang. *Constraint Effect in Brittle Fracture*. 1997.

[40] F. Berto and P. Lazzarin. On higher order terms in the crack tip stress field. *International Journal of Fracture*, 161(2):221–226, 2010.

[41] F. Erdogan and G. C. Sih. On the crack extension in plates under plane loading and transverse shear. *Journal of Basic Engineering*, 85(4):519–525, 1963.

[42] M. R. Ayatollahi and B. Saboori. T-stress effects in mixed mode i/ii/iii brittle fracture. *Engineering Fracture Mechanics*, 144:32–45, 2015.

[43] A. Richard H, M. Fulland, and M. Sander. Theoretical crack path prediction. *Fatigue & Fracture of Engineering Materials & Structures*, 28(1-2):3–12, 2004.

[44] M. R. Ayatollahi and M. R. M. Aliha. Fracture analysis of some ceramics under mixed mode loading. *Journal of the American Ceramic Society*, 94(2):561–569, 2011.

[45] M. Rashidi Moghaddam, M. R. Ayatollahi, and F. Berto. Mixed mode fracture analysis using generalized averaged strain energy density criterion for linear elastic materials. *International Journal of Solids and Structures*, 120:137–145, 2017.

[46] Zohar Yosibash, Arie Bussiba, and Ilan Gilad. Failure criteria for brittle elastic materials. *International Journal of Fracture*, 125(3):307–333, 2004.

[47] Ghatee Mojtaba and Salari Farid. Electrical and mechanical properties of 5ysz tubular thin film prepared by screen printing method. *International Journal of Applied Ceramic Technology*, 13(2):373–381, 2016.

[48] ASTM ASTM Committee C28. Standard test methods for determination of fracture toughness of advanced ceramics at ambient temperature, 2010.

[49] International Organization for Standardization. Fine ceramics (advanced ceramics, advanced technical ceramics) — test methods for fracture toughness of monolithic ceramics — single-edge v-notch beam (sevnb) method, 2008.

[50] M. R. Ayatollahi and M. R. M. Aliha. On the use of an anti-symmetric four-point bend specimen for mode ii fracture experiments. *Fatigue & Fracture of Engineering Materials & Structures*, 34(11):898–907, 2011.

[51] R. W. Margevicius, J. Riedle, and P. Gumbsch. Fracture toughness of polycrystalline tungsten under mode i and mixed mode i/ii loading. *Materials Science and Engineering: A*, 270(2):197–209, 1999.

[52] P. Lazzarin and S. Filippi. A generalized stress intensity factor to be applied to rounded v-shaped notches. *International Journal of Solids and Structures*, 43(9):2461–2478, 2006.

[53] F. Fleischhauer, R. Bermejo, R. Danzer, A. Mai, T. Graule, and J. Kuebler. High temperature mechanical properties of zirconia tapes used for electrolyte supported solid oxide fuel cells. *Journal of Power Sources*, 273:237–243, 2015.

Appendix A

The geometry of the ordered specimen

45

22,4

B

3

4

0,2

0,8
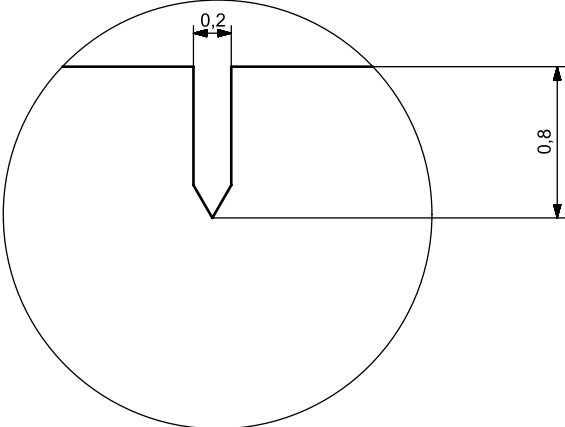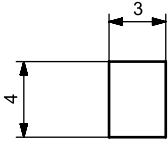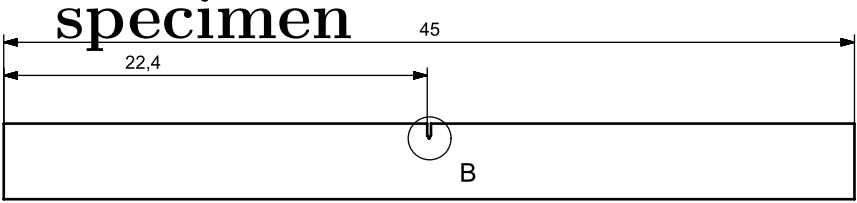
DETAIL B
SCALE 50:1

Dato	Konstr./Tegnet	Godkjent	Maalestokk	NTNU - IPM	
	SWB	Projeksjonsmetode	5:1		
				Erstatning for:	Erstattet av:
Henvisning:		Beregning:			

45

22,4

B

6

5

0,2

1,8
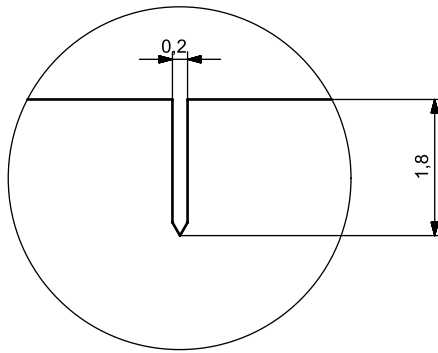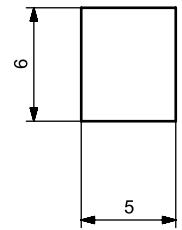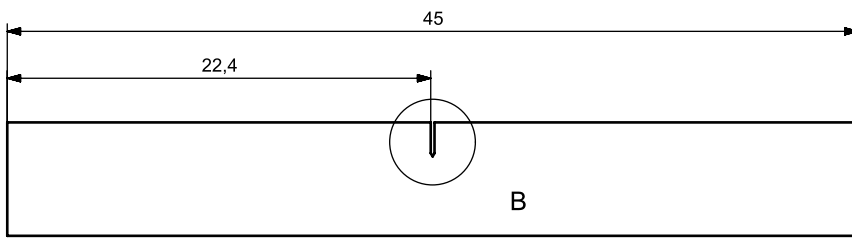
DETAIL B
SCALE 20:1

Dato	Konstr./Tegnet	Godkjent	Maalestokk	NTNU - IPM	
	SWB	Projeksjonsmetode	5:1		
				Erstatning for:	Erstattet av:
Henvisning:		Beregning:			

Appendix B

For the simulated models of Li et al. and Suresh et al.

```python
# -*- coding: mbcs -*-
# Do not delete the following import lines
# The from and import is needed to function in Abaqus
from abaqus import *
from abaqusConstants import *
import __main__
import section
import regionToolset
import displayGroupMdbToolset as dgm
import part
import material
import assembly
import step
import interaction
import load
import mesh
import optimization
import job
import sketch
import visualization
import xyPlot
import displayGroupOdbToolset as dgo
import connectorBehavior
import numpy as np

def loadPart(partdir, Model_Name): # Loads the part named in main
                                   # function. Make sure the part
                                   # directory and the name of the mode
                                   # add up.
    openMdb(pathName=partdir)
    p = mdb.models[Model_Name].parts['Part-1']

def calc_dimensionCHANGES(Ltot, S1, S2, S0, Width): # Calculates the
                                                    # dimensions that are set in the
                                                    # abaqus model. Mixed mode and mode II
    W = Width
    L1d = (Ltot/2.0) + S0 - S2
    L2d = (Ltot/2.0) - S0 - S1
    L3d = (Ltot/2.0) + S0 - S1
    L4d = (Ltot/2.0) - S0 - S2
```

```python
    L1x = L1d
    L2x = Ltot - L2d
    L3x = L3d
    L4x = Ltot - L4d
    L1y = 0
    L2y = 0
    L3y = W
    L4y = W
    return L1d, L2d, L3d, L4d, L1x, L2x, L3x, L4x, L1y, L2y, L3y, L4y

def calc_dimensionCHANGES_Pure_Mode_I(Ltot, Sout, Sin, Width): #
                                      Calculates the dimensions for pure
                                      mode I loading
    W = Width
    L1d = (Ltot/2.0) - Sout/2.0
    L2d = (Ltot/2.0) - Sout/2.0
    L3d = (Ltot/2.0) - Sin/2.0
    L4d = (Ltot/2.0) - Sin/2.0
    L1x = L1d
    L2x = Ltot - L2d
    L3x = L3d
    L4x = Ltot - L4d
    L1y = 0
    L2y = 0
    L3y = W
    L4y = W
    return L1d, L2d, L3d, L4d, L1x, L2x, L3x, L4x, L1y, L2y, L3y, L4y

def dimChange_MINGLI(Model_Name, L1d, L2d, L3d, L4d): # Changes the
                                      dimensions that make
    a = mdb.models[Model_Name].rootAssembly
    s = a.features['Partition face-1'].sketch
    mdb.models[Model_Name].ConstrainedSketch(name='__edit__',
                                      objectToCopy=s)
    s1 = mdb.models[Model_Name].sketches['__edit__']
    g, v1, d, c = s1.geometry, s1.vertices, s1.dimensions, s1.
                                      constraints
    s1.setPrimaryObject(option=SUPERIMPOSE)
    a.projectReferencesOntoSketch(sketch=s1,
        upToFeature=a.features['Partition face-1'], filter=
                                      COPLANAR_EDGES)
    d[0].setValues(value=L1d, )
    d[1].setValues(value=L2d, )
    d[2].setValues(value=L3d, )
    d[3].setValues(value=L4d, )
    s1.unsetPrimaryObject()
    a = mdb.models[Model_Name].rootAssembly
    a.features['Partition face-1'].setValues(sketch=s1)
    del mdb.models[Model_Name].sketches['__edit__']
    a = mdb.models[Model_Name].rootAssembly
    a.regenerate()

def meshModel(Model_Name): #Mesh the model
    a = mdb.models[Model_Name].rootAssembly
    partInstances =(a.instances['Part-1-1'], )
    a.generateMesh(regions=partInstances)

#xy is the coordinate of the point. The bounding box is used to
```

```python
#select the points. Applies load the chosen point.
def applyLoadToPoint(x,y,P_calculated, name_of_load, Model_Name):
    a = mdb.models[Model_Name].rootAssembly
    v1 = a.instances['Part-1-1'].vertices
    verts1 = v1.getByBoundingBox(x-0.1,y-0.1,-0.1,x+0.1,y+0.1,0.1)
    region = regionToolset.Region(vertices=verts1)
    mdb.models[Model_Name].ConcentratedForce(name=name_of_load,
        createStepName='Step-1', region=region, cf2=P_calculated,
        distributionType=UNIFORM, field='', localCsys=None)

#xy is the coordinate of the point. The bounding box is used to
#select the points. Applies boundary condition no y-movement to the
                                chosen point.
def createBC_U2(x,y, BC_Name, Model_Name):
    a = mdb.models[Model_Name].rootAssembly
    v1 = a.instances['Part-1-1'].vertices
    verts1 = v1.getByBoundingBox(x-0.1,y-0.1,-0.1,x+0.1,y+0.1,0.1)
    region = regionToolset.Region(vertices=verts1)
    mdb.models[Model_Name].DisplacementBC(name=BC_Name, createStepName='
                                Initial',
        region=region, u1=UNSET, u2=SET, ur3=UNSET, amplitude=UNSET,
        distributionType=UNIFORM, fieldName='', localCsys=None)

#xy is the coordinate of the point. The bounding box is used to
#select the points. Applies boundary condition no xy-movement to the
                                chosen point.
def createBC_U1U2(x,y, BC_Name, Model_Name):
    a = mdb.models[Model_Name].rootAssembly
    v1 = a.instances['Part-1-1'].vertices
    verts1 = v1.getByBoundingBox(x-0.1,y-0.1,-0.1,x+0.1,y+0.1,0.1)
    region = regionToolset.Region(vertices=verts1)
    mdb.models[Model_Name].DisplacementBC(name=BC_Name, createStepName='
                                Initial',
        region=region, u1=SET, u2=SET, ur3=UNSET, amplitude=UNSET,
        distributionType=UNIFORM, fieldName='', localCsys=None)

#creates and submits job, waits for completion and
# opens the database to the vizualisation for later view
def createJob(job_name, Model_Name):
    mdb.Job(name=job_name, model=Model_Name, description='', type=
                                ANALYSIS,
        atTime=None, waitMinutes=0, waitHours=0, queue=None, memory=90,
        memoryUnits=PERCENTAGE, getMemoryFromAnalysis=True,
        explicitPrecision=SINGLE, nodalOutputPrecision=SINGLE, echoPrint
                                =OFF,
        modelPrint=OFF, contactPrint=OFF, historyPrint=OFF,
                                userSubroutine='',
        scratch='', resultsFormat=ODB, multiprocessingMode=DEFAULT,
                                numCpus=1,
        numGPUs=0)
    mdb.jobs[job_name].submit(consistencyChecking=OFF)
    mdb.jobs[job_name].waitForCompletion()
    o3 = session.openOdb(name='C:/Temp/'+job_name+'.odb')

#Calculats how the roller divide the applied loads from the testing
                                machine
def calculateP(S1, S2, P):
    P = float(P)
```

```python
    A = (S1)/(S1+S2)
    P2 = A*P
    P1 = (1.0-A)*P
    return P1, P2

#Sums the strain energy for all elements in requested field output
def get_ELSE(job_name):
    odb = session.openOdb(job_name+'.odb')
    a= odb.rootAssembly
    inst = a.instances['PART-1-1']
    myelse=odb.steps['Step-1'].frames[-1].fieldOutputs['ELSE']
    tote=0
    for i in myelse.values:
        tote=tote+i.data
    return tote

#Sums the volume for all elements in requested field output
def get_EVOL(job_name):
    odb = session.openOdb(job_name+'.odb')
    a= odb.rootAssembly
    inst = a.instances['PART-1-1']
    myevol=odb.steps['Step-1'].frames[-1].fieldOutputs['EVOL']
    totv=0
    for i in myevol.values:
        totv=totv+i.data
    return totv

#Makes a string for use in printing data
def make_string(Evol,Else,delim,job_name):
    job_name = str(job_name).replace(",",".")
    s = job_name+delim+str(Evol)+delim+str(Else)+'\n'
    return s

#Main function running all other functions
#S1,S2 = roller dimension from crack front
#S0 = load point variation
#Model_name = the name of the model in Abaqus
#job_name = the name of the job that is submitted
#Ltot = the totalt length of the test specimen that you have modeled.
#Width = the width of the specimen that you have modeled.
def runModel_MINGLI(S1, S2, S0, Ptot, Model_Name, job_name, Ltot, Width)
                                    :
    partdir = 'D:/Documents/abaqustesting/Crack/data_simulation/ming_li'
    loadPart(partdir, Model_Name)
    L1d, L2d, L3d, L4d, L1x, L2x, L3x, L4x, L1y, L2y, L3y, L4y =
                                    calc_dimensionCHANGES(Ltot, S1,
                                    S2, S0, Width)
    dimChange_MINGLI(Model_Name, L1d, L2d, L3d, L4d)
    P1, P2 = calculateP(S1, S2, Ptot)
    createBC_U1U2(L2x,0, 'L2', Model_Name) #L2
    createBC_U2(L1x,0,'L1', Model_Name) #L1
    applyLoadToPoint(L3x, Width, P1, 'L3', Model_Name) #L3
    applyLoadToPoint(L4x, Width, P2, 'L4', Model_Name) #L4
    meshModel(Model_Name)
    createJob(job_name, Model_Name)
    EVOL = get_EVOL(job_name)
    ELSE = get_ELSE(job_name)
    s = make_string(EVOL, ELSE,',',job_name)
```

```python
    f=open(work_dir+report_filename,'a')
    f.write(s)
    f.close

#Sin = distance between inner roller bearings in test setup
#Sout = distance between outer roller distance in test setup
#Model_name = the name of the model in Abaqus
#job_name = the name of the job that is submitted
#Ltot = the totalt length of the test specimen that you have modeled.
#Width = the width of the specimen that you have modeled.
def runModel_MINGLI_Pure_Mode_I(Sin, Sout, Ptot, Model_Name, job_name,
                                Ltot, Width):
    partdir = 'D:/Documents/abaqustesting/Crack/data_simulation/ming_li'
    loadPart(partdir, Model_Name)
    L1d, L2d, L3d, L4d, L1x, L2x, L3x, L4x, L1y, L2y, L3y, L4y =
                                calc_dimensionCHANGES_Pure_Mode_I
                                (Ltot, Sout, Sin, Width)
    dimChange_MINGLI(Model_Name, L1d, L2d, L3d, L4d)
    P1, P2 = calculateP(Sin/2.0, Sin/2.0, Ptot)
    createBC_U1U2(L2x,0, 'L2', Model_Name) #L2
    createBC_U2(L1x,0,'L1', Model_Name) #L1
    applyLoadToPoint(L3x, Width, P1, 'L3', Model_Name) #L3
    applyLoadToPoint(L4x, Width, P2, 'L4', Model_Name) #L4
    meshModel(Model_Name)
    createJob(job_name, Model_Name)
    EVOL = get_EVOL(job_name)
    ELSE = get_ELSE(job_name)
    s = make_string(EVOL, ELSE,',',job_name)
    f=open(work_dir+report_filename,'a')
    f.write(s)
    f.close

### GLOBAL PARAMETERS ###
# work directory of abaqus and the filename of the report that the
                                script prints.
work_dir='C:/Temp/'
report_filename='MyExcellentResults.txt'

#function for making range increments with decimal.
def frange(start, stop, step):
    ''' "range()" like function which accept float type'''
    i = start
    while i < stop:
        yield i
        i += step

#Making space between script runs in the report
f=open(work_dir+report_filename,'a')
f.write('\n\n')
f.close

#S0 distances that were assumed from the papers studied
#Gl = glass
#Al = Alumina
#Short = short samples of alumina
#Long = long samples of alumina
```

```python
Gl_M = np.array([2.2, 2.2, 1.2, 1.2, 0.57, 0.57, 0.28, 0.28, 1.5, 1.5, 0
                                .0, 0.0, 0.0])
Al_M = np.array([0.0, 0.15, 0.30, 0.5, 0.85, 2])
Short_S = np.array([0.0, 0.78, 1.6, 2.6])
Long_S = np.array([0.0, 0.25, 0.65, 1.3, 2.0, 2.4, 2.6, 3.0])


# Comment out the lines below that is not wanted for the run of the
                                simulation.
for i in Gl_M:
    runModel_MINGLI(5.0,15.0,float(i),-1.0,'Model-2',str(i).replace(".",
                                ","),37.0, 4.0) # Glass

for i in Al_M:
    runModel_MINGLI(10.0,5.0,-float(i),-1.0,'Model-1',str(i).replace("."
                                ,","),32, 3.2) # Alumina Ming Li

for i in Short_S:
    runModel_MINGLI(19.8,9.9,-(float(i)),-1.0,'Model-4',str(i).replace("
                                .",","),50.8, 9.9) # Alumina
                                Short

for i in Long_S:
    runModel_MINGLI(34.3,24.1,-(float(i)),-1.0,'Model-3',str(i).replace(
                                ".",","),78.7, 10.2) # Alumina
                                Long

for i in frange(0.0,5.0,0.2):
    runModel_MINGLI(34.3,24.1,-(float(i)),-1.0,'Model-3',str(i).replace(
                                ".",","),78.7, 10.2) # Alumina
                                Long

for i in frange(0.0,4.0,0.5):
    runModel_MINGLI(19.8,9.9,-(float(i)),-1.0,'Model-4',str(i).replace("
                                .",","),50.8, 9.9) # Alumina
                                Short

for i in frange(0.0,2.2,0.2):
    runModel_MINGLI(5.0,10.0,float(i),-1.0,'Model-1',str(i).replace(".",
                                ","),32, 3.2) # Alumina Ming Li

for i in frange(0.0,2.5,0.4):
    runModel_MINGLI(5.0,15.0,float(i),-1.0,'Model-2',str(i).replace(".",
                                ","),37.0, 4.0) # Glass

for i in frange(0.0,3.0,0.2):
    runModel_MINGLI(20.0,15.0,-float(i),-1.0,'Model-5',str(i).replace(".
                                ",","),50.0, 6.0) # Tungsten


runModel_MINGLI_Pure_Mode_I(10.0, 20.0, -105.1, 'Model-1', 'Alumina', 32
                                .0, 3.2)
runModel_MINGLI_Pure_Mode_I(10.0, 30.0, -22.84, 'Model-2', 'Glass', 37.0
                                , 4.0)
runModel_MINGLI_Pure_Mode_I(30.0, 60.0, -249.6, 'Model-3', 'LongAl', 78.
                                7, 10.2)
```

```
runModel_MINGLI_Pure_Mode_I(20.0, 40.0, -343.9, 'Model-4', 'ShortAl', 50
                                       .8, 9.9)
runModel_MINGLI_Pure_Mode_I(20.0, 40.0, -248.1, 'Model-5', 'Tungsten_Pc'
                                       , 50.0, 6.0)


runModel_MINGLI_Pure_Mode_I(20.0, 50.0, -1.0, 'Model-3', 'LongAl_test',
                                       78.7, 10.2)
runModel_MINGLI_Pure_Mode_I(15.0, 30.0, -1.0, 'Model-4', 'ShortAl_test',
                                       50.8, 9.9)

for i in frange(0.0,1.0,0.05):
    runModel_MINGLI(5.0,10.0,float(i),-1.0,'Model-1',str(i).replace(".",
                                       ","),32, 3.2) # Alumina Ming Li

for i in frange(0.0,1.0,0.05):
runModel_MINGLI(5.0,10.0,float(i),-1.0,'Model-1',str(i).replace(".",",")
                                       ,32, 3.2) # Alumina suresh

for i in frange(0.8,3.0,0.2):
    runModel_MINGLI(5.0,15.0,float(i),-1.0,'Model-2',str(i).replace(".",
                                       ","),37, 4.0) # Glass
```

Appendix C

Script for 3x4x45 model specimen

```python
    # -*- coding: mbcs -*-
# Do not delete the following import lines
from abaqus import *
from abaqusConstants import *
import __main__
import section
import regionToolset
import displayGroupMdbToolset as dgm
import part
import material
import assembly
import step
import interaction
import load
import mesh
import optimization
import job
import sketch
import visualization
import xyPlot
import displayGroupOdbToolset as dgo
import connectorBehavior

#changes
def loadPart(partdir):
    openMdb(pathName=partdir)
    p = mdb.models['Model-1'].parts['Part-1']

#changes the dimension that section the edges
def dimensionChange(L1d,L2d,L3d,L4d):
    a = mdb.models['Model-1'].rootAssembly
    s = a.features['Partition face-1'].sketch
    mdb.models['Model-1'].ConstrainedSketch(name='__edit__',
                                            objectToCopy=s)
    s1 = mdb.models['Model-1'].sketches['__edit__']
    g, v, d, c = s1.geometry, s1.vertices, s1.dimensions, s1.constraints
    s1.setPrimaryObject(option=SUPERIMPOSE)
    a.projectReferencesOntoSketch(sketch=s1,
        upToFeature=a.features['Partition face-1'], filter=
                                        COPLANAR_EDGES)
    d[0].setValues(value=L3d, )
    d[1].setValues(value=L4d, )
```

```python
    d[3].setValues(value=L1d, )
    d[2].setValues(value=L2d, )
    s1.unsetPrimaryObject()
    a = mdb.models['Model-1'].rootAssembly
    a.features['Partition face-1'].setValues(sketch=s1)
    del mdb.models['Model-1'].sketches['__edit__']
    a = mdb.models['Model-1'].rootAssembly
    a.regenerate()

#mesh the model preexisting model
def meshModel():
    a = mdb.models['Model-1'].rootAssembly
    partInstances =(a.instances['Part-1-1'], )
    a.generateMesh(regions=partInstances)

#marks the point and applies the load
def applyLoadToPoint(x,y,P,name_of_load):
    a = mdb.models['Model-1'].rootAssembly
    v1 = a.instances['Part-1-1'].vertices
    verts1 = v1.getByBoundingBox(x-0.1,y-0.1,-0.1,x+0.1,y+0.1,0.1)
    region = regionToolset.Region(vertices=verts1)
    mdb.models['Model-1'].ConcentratedForce(name=name_of_load,
        createStepName='Step-1', region=region, cf2=P,
        distributionType=UNIFORM, field='', localCsys=None)

#marks the point xy and constrains the point in y-direction
def createBC_U2(x,y):
    a = mdb.models['Model-1'].rootAssembly
    v1 = a.instances['Part-1-1'].vertices
    verts1 = v1.getByBoundingBox(x-0.1,y-0.1,-0.1,x+0.1,y+0.1,0.1)
    region = regionToolset.Region(vertices=verts1)
    mdb.models['Model-1'].DisplacementBC(name='L3', createStepName='
                                        Initial',
        region=region, u1=UNSET, u2=SET, ur3=UNSET, amplitude=UNSET,
        distributionType=UNIFORM, fieldName='', localCsys=None)

#Marks the point of xy and constraints it in xy-direction
def createBC_U1U2(x,y):
    a = mdb.models['Model-1'].rootAssembly
    v1 = a.instances['Part-1-1'].vertices
    verts1 = v1.getByBoundingBox(x-0.1,y-0.1,-0.1,x+0.1,y+0.1,0.1)
    region = regionToolset.Region(vertices=verts1)
    mdb.models['Model-1'].DisplacementBC(name='L4', createStepName='
                                        Initial',
        region=region, u1=SET, u2=SET, ur3=UNSET, amplitude=UNSET,
        distributionType=UNIFORM, fieldName='', localCsys=None)

#Creates job, submits job and waits for completion and open Odb.
def createJob(job_name):
    mdb.Job(name=job_name, model='Model-1', description='', type=
                                        ANALYSIS,
        atTime=None, waitMinutes=0, waitHours=0, queue=None, memory=90,
        memoryUnits=PERCENTAGE, getMemoryFromAnalysis=True,
        explicitPrecision=SINGLE, nodalOutputPrecision=SINGLE, echoPrint
                                        =OFF,
        modelPrint=OFF, contactPrint=OFF, historyPrint=OFF,
                                        userSubroutine='',
```

```
                    scratch='', resultsFormat=ODB, multiprocessingMode=DEFAULT,
                                                      numCpus=1,
            numGPUs=0)
     mdb.jobs[job_name].submit(consistencyChecking=OFF)
     mdb.jobs[job_name].waitForCompletion()
     o3 = session.openOdb(name='C:/Temp/'+job_name+'.odb')


#Sums the strain energy of all elements requested in fieldoutput
def get_ELSE(job_name):
     odb = session.openOdb(job_name+'.odb')
     a= odb.rootAssembly
     inst = a.instances['PART-1-1']
     myelse=odb.steps['Step-1'].frames[-1].fieldOutputs['ELSE']
     tote=0
     for i in myelse.values:
         tote=tote+i.data
     return tote


#Sums the volume of all elements requested in fieldoutput
def get_EVOL(job_name):
     odb = session.openOdb(job_name+'.odb')
     a= odb.rootAssembly
     inst = a.instances['PART-1-1']
     myevol=odb.steps['Step-1'].frames[-1].fieldOutputs['EVOL']
     totv=0
     for i in myevol.values:
         totv=totv+i.data
     return totv


#Makes a string
def make_string(Evol,Else,delim,job_name):
     job_name = str(job_name).replace(",",".")
     s = job_name+delim+str(Evol)+delim+str(Else)+'\n'
     return s


#Calulcates load in point 1 and 2
def calculateP(L1,L2,P):
     A = L1/(L1+L2)
     PL2 = A*P
     PL1 = (1.0-A)*P
     return PL1, PL2


#calculates R0 control volume radius
def calc_R0(v,Kic,Suts):
     A = (1+v)
     B = (5-8*v)
     C = (Kic/Suts)**2
     D = 4*3.141592
     R0 = (A*B*C*1000)/D
     return R0


#Changes the dimension that is the inner circle, the ASED control volume
                               radius
def change_SED_circle(R0):
     a = mdb.models['Model-1'].rootAssembly
     s = a.features['Partition face-2'].sketch
     mdb.models['Model-1'].ConstrainedSketch(name='__edit__',
                                   objectToCopy=s)
```

```python
    s1 = mdb.models['Model-1'].sketches['__edit__']
    g, v, d, c = s1.geometry, s1.vertices, s1.dimensions, s1.constraints
    s1.setPrimaryObject(option=SUPERIMPOSE)
    a.projectReferencesOntoSketch(sketch=s1,
        upToFeature=a.features['Partition face-2'], filter=
                                        COPLANAR_EDGES)
    d[6].setValues(value=R0, )
    s1.unsetPrimaryObject()
    a = mdb.models['Model-1'].rootAssembly
    a.features['Partition face-2'].setValues(sketch=s1)
    del mdb.models['Model-1'].sketches['__edit__']
    a = mdb.models['Model-1'].rootAssembly
    a.regenerate()

#Changes the Poisson's ratio in the material module
def change_Pratio(Pratio):
    mdb.models['Model-1'].materials['Y3SZ'].elastic.setValues(table=((
                                        213000.0,
        Pratio), ))


#Runs a model with crack = 1.4 mm
def runModel_new_14mm(L1,L2,L3,L4,job_name,P):
    partdir = 'D:/Documents/abaqustesting/Crack/new again/crack_14mm'
    loadPart(partdir)
    L1x, L2x, L3x, L4x, L1d, L2d, L3d, L4d = Lcoord45(L1,L2,L3,L4)
    dimensionChange(L1d,L2d,L3d,L4d)
    meshModel()
    PL1, PL2 = calculateP(L1,L2,P)
    applyLoadToPoint(L1x,0,PL1,'L1') #L1
    applyLoadToPoint(L2x,0,PL2,'L2') #L2
    createBC_U1U2(L4x,4) #L4
    createBC_U2(L3x,4) #L3
    meshModel()
    createJob(job_name)

#Runs a model with crack = 2mm
def runModel_new_2mm(L1,L2,L3,L4,job_name,P):
    partdir = 'D:/Documents/abaqustesting/Crack/new again/crack_2mm'
    loadPart(partdir)
    L1x, L2x, L3x, L4x, L1d, L2d, L3d, L4d = Lcoord45(L1,L2,L3,L4)
    dimensionChange(L1d,L2d,L3d,L4d)
    meshModel()
    PL1, PL2 = calculateP(L1,L2,P)
    applyLoadToPoint(L1x,0,PL1,'L1') #L1
    applyLoadToPoint(L2x,0,PL2,'L2') #L2
    createBC_U1U2(L4x,4) #L4
    createBC_U2(L3x,4) #L3
    meshModel()
    createJob(job_name)
    EVOL = get_EVOL(job_name)
    ELSE = get_ELSE(job_name)
    s = make_string(EVOL, ELSE,',',job_name)
    f=open(work_dir+report_filename,'a')
    f.write(s)
    f.close

#Runs a model with crack = 2.4mm
```

```python
def runModel_new_24mm(L1,L2,L3,L4,job_name,P):
    partdir = 'D:/Documents/abaqustesting/Crack/new again/crack_24mm'
    loadPart(partdir)
    L1x, L2x, L3x, L4x, L1d, L2d, L3d, L4d = Lcoord45(L1,L2,L3,L4)
    dimensionChange(L1d,L2d,L3d,L4d)
    meshModel()
    PL1, PL2 = calculateP(L1,L2,P)
    applyLoadToPoint(L1x,0,PL1,'L1') #L1
    applyLoadToPoint(L2x,0,PL2,'L2') #L2
    createBC_U1U2(L4x,4) #L4
    createBC_U2(L3x,4) #L3
    meshModel()
    createJob(job_name)

#Runs the model in which the control volume of ASED can be changed.
def runModel_new_2mm_changeR0(L1,L2,L3,L4,job_name,P,v,Kic,Suts):
    partdir = 'D:/Documents/abaqustesting/Crack/new again/
                                    crack_2mm_SED_Circle_change'
    loadPart(partdir)
    L1x, L2x, L3x, L4x, L1d, L2d, L3d, L4d = Lcoord45(L1,L2,L3,L4)
    dimensionChange(L1d,L2d,L3d,L4d)
    change_Pratio(v)
    R0 = calc_R0(v,Kic,Suts)
    change_SED_circle(R0)
    meshModel()
    PL1, PL2 = calculateP(L1,L2,P)
    applyLoadToPoint(L1x,0,PL1,'L1') #L1
    applyLoadToPoint(L2x,0,PL2,'L2') #L2
    createBC_U1U2(L4x,4) #L4
    createBC_U2(L3x,4) #L3
    meshModel()
    createJob(job_name)
    EVOL = get_EVOL(job_name)
    ELSE = get_ELSE(job_name)
    s = make_string(EVOL, ELSE,',',job_name)
    f=open(work_dir+report_filename,'a')
    f.write(s)
    f.close

### GLOBAL PARAMETERS ###

work_dir='C:/Temp/'
report_filename='MyExcellentResults.txt'

#Marks new simulation in the report
f=open(work_dir+report_filename,'a')
f.write('\n\n')
f.close

#Similar to in range, but for decimal numbers
def frange(start, stop, step):
    ''' "range()" like function which accept float type'''
    i = start
    while i < stop:
        yield i
        i += step

#For changing poisson ratio
```

```python
for j in frange(0.28,0.35,0.02):
#For changing wanted roller distance
for i in frange(5.0,20.5, 1.0):

runModel_new_2mm(20,20,10,10,'pureModeI_a_2mmx2',59.26*2) #pure Mode I
runModel_new_2mm_changeR0(20.0,5.0,5.0,float(i),'v='+str(j).replace(".",
                                    ",")+'-'+str(i).replace(".",","),1.0
                                    ,j,4.1,664.0) # Mixed mode to pure
                                    mode II
runModel_new_2mm_changeR0(20.0,20.0,10.0,10.0,'pureModeI_a_2mm_5YSZ',1.0
                                    ,0.3,2.8,272.0)
runModel_new_14mm(20,5,5,float(i),str(i).replace(".",","),1) # Mixed
                                    mode to pure mode II
runModel_new_24mm(20,5,5,float(i),str(i).replace(".",","),1) # Mixed
                                    mode to pure mode II
runModel_new_2mm_changeR0(20.0,5.0,5.0,float(i),'v='+str(j).replace(".",
                                    ",")+'-'+str(i).replace(".",","),1.0
                                    ,j,4.1,664.0)
```
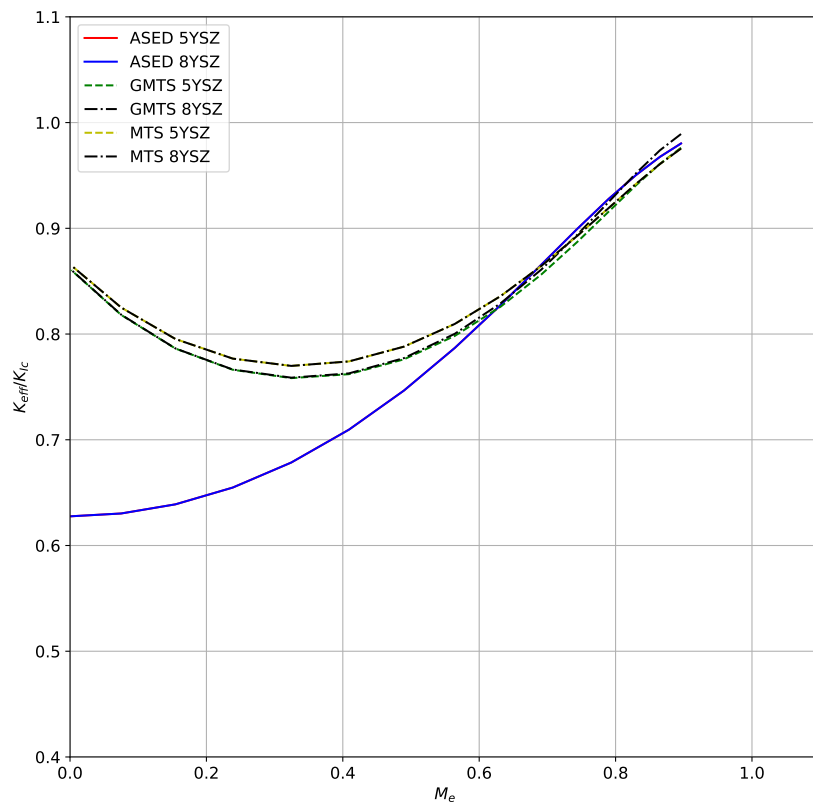
Appendix D

Plot of 3YSZ, 5YSZ and 8YSZ

Figure D.1